2017

Energy transport at the micro-/nanoscale and structure discovery based on phonon scattering

Jing Liu
Iowa State University

Energy transport at the micro-/nanoscale and structure discovery based on phonon scattering

by

Jing Liu

A dissertation submitted to the graduate faculty

in partial fulfillment of the requirements for the degree of

DOCTOR OF PHILOSOPHY

Major: Mechanical Engineering

Program of Study Committee:
Xinwei Wang, Major Professor
Xianglan Bai
Wei Hong
Reza Montazami
Chenxu Yu

The student author and the program of study committee are solely responsible for the content of this dissertation. The Graduate College will ensure this dissertation is globally accessible and will not permit alterations after a degree is conferred.

Iowa State University

Ames, Iowa

2017

DEDICATION

I would like to dedicate this dissertation to my family who have supported me throughout my life and education. My lovely parents, Xianrong Liu and Renzhu Jin, whose endless love has supported me the whole life. My older sister, Yan Liu, who is very special to me and gives me brave to pursue what I want. My loving boyfriend, Zedong Wang, gives me the brave and flying wings to pursue my future.

TABLE OF CONTENTS

Page

LIST OF FIGURES

Page

LIST OF TABLES

Page

ACKNOWLEDGEMENTS

My deepest gratitude goes first and foremost to Dr. Xinwei Wang, my major professor. I show my deep gratitude to him for the chance of joining Micro/Nanoscale Thermal Science Laboratory. My experience in the lab is very important in my life. I am deeply inspired by him, not only due to the intelligence but also the work attitude. Without his advice, great efforts, patience as well as support, I could not prepare myself well for the future challenges. I would also like to thank Dr. Xianglan Bai, for the advice and chance of cooperation during my PhD period. I want to thank Dr. Wei Hong, Dr. Reza Montazami and Dr. Chenxu Yu for their advice during the research and that makes my research more completed.

Second, I should give my heart thanks to my lab mates in Micro/Nanoscale Thermal Science Laboratory, Shen Xu, Zaoli Xu, Chong Li, Yangsu Xie, Zhe Cheng, Bowen Zhu, Tianyu Wang, Meng Han, Pengyu Yuan and Ridong Wang. Without their help, my research would be much harder.

Third, I would like to thank my friends Christine Hendershot and Katy Springer in Ames. Their encouragement gives me the confidence to face the challenges in work and life.

Finally, my thanks and love go to my parents, my elder sister and my boyfriend from my deep heart. I am truly indebted to them for all the sacrifices they have made for me throughout my life.

Support of the work by the Army Research Office (W911NF-12-1-0272), Office of Naval Research (N000141210603), National Science Foundation (CBET1235852, CMMI1264399), Department of Energy (DENE0000671, DE-EE0007686) and Iowa Energy Center (MG-16-025, OG-17-005) is gratefully acknowledged. I thank Prof. Xiulin Ruan of Purdue University very much for the discussion on electron-phonon energy coupling in graphene.

ABSTRACT

The various microscale structures of materials play an important role in determining and predicting the thermal transport performance of the materials. To have a better understanding of the structure effect, this work focuses on studying the effect of microscale structure on thermal transport behaviors of materials. To this end, the thermal conductivity of several materials with different microscale structure has been characterized using different methods in this work. The thermal transport behaviors have been further studied in detail by analyzing the phonon propagation mechanisms in the materials. Specifically, a Johnson noise electro-thermal technique has been firstly developed to directly measure the thermal conductivity (k) of microscale glass fiber. This new technique provides a good improvement for the thermal properties measurement by avoiding the requirement of the resistance temperature coefficient calibration.

Furthermore, three typical materials: ultra-high molecular weight polyethylene (UHMWPE) fiber, giant size graphene on PMMA, and lignin-based carbon fiber (CF), are chosen to study the effect of structure on thermal conductivity. By using the transient electro-thermal technique, the thermal diffusivity and thermal conductivity variations against temperature of PE fibers from room temperature down to 22 K are measured. By using the newly developed "thermal reffusivity" model, the residual phonon thermal reffusivity (Θ_0) of PE is obtained, which gives significant information about the phonon scattering in the materials. The defect-induced low-momentum phonon mean free paths are determined by using Θ_0, which are much smaller than the crystallite size determined by XRD. The results strongly demonstrate the dominating diffuse phonon scattering at the grain boundaries. The carbon chains in the crystallites are quiet along the

fiber axial direction, which contributes to the high thermal conductivity of our samples [~25 W/(m·K)]. The grains interface thermal conductance in PE fibers is subsequently evaluated.

Thermal properties measurement of mm-scale graphene is critical for device/system-level thermal design since it reflects the effect of abundant grains in graphene. The thermal conductivity of giant size graphene supported by PMMA is determined for the first time by using a differential technique. This giant graphene measurement eliminates the thermal contact resistance problems and edge phonon scattering encountered in μm-scale graphene thermal conductivity measurement. The thermal conductivity of 1.33-layered, 1.53-layered, 2.74-layered and 5.2-layered supported graphene is measured as 365, 359, 273 and 33.5 W/(m·K), respectively. The existence of graphene oxide, disorder in sp^2 domain and stratification leads to the thermal conductivity reduction in 5.2-layered graphene.

The microstructure of lignin-based CF is important to study the thermal transport. The structure domain size of the CF is investigated by x-ray scattering, Raman scattering, and phonon scattering at the 0 K limit. The 0 K-limit phonon scattering mean free path (~12 Å) uncovers a characteristic structure size, and it agrees well with the crystallite size by x-ray scattering (9 and 13 Å) and the cluster size by Raman spectroscopy (23 Å). The thermal diffusivity and reffusivity of CFs show little change from room temperature down to 10 K, uncovering the existence of extensive defects and grain boundaries which dominate the phonon scattering. The thermal conductivity of CFs is significantly increased by more than ten-fold after being annealed at 2770 K, to a level of 24 W/(m·K). This is due to the improvement of graphitic structure in the annealed CFs. Our microscale Raman scanning from slightly annealed to strongly annealed regions shows

one-fold increase of the cluster size: from 1.83 nm to 4 nm, directly uncovering structure improvement by annealing. The inverse of the thermal conductivity is found linearly proportional to the annealing temperature in the range of 1000-2770 K.

CHAPTER 1 INTRODUCTION

1.1 Thermal Transport in Micro-/Nanoscale Materials

Recently, due to the progress in synthesis and analysis of micro/-nanoscale materials, many micro-/nanoscale materials have been demonstrated to have promising engineering applications. Examples include nanocomposites, microelectronics and optoelectronic devices, multiplayer coating and so on.[1] The thermal conductivity of macroscale materials is measured according to Fourier's law. However, when the characteristic length of the micro-/nanoscale materials becomes comparable to the mean free path of the heat carriers (phonons and/or electrons), the thermal transport mechanism becomes different from the macroscale counterpart. The grain boundaries and surface will play a major role in limiting the scattering process, which finally leads to the thermal conductivity reduction in micro-/nanoscale materials.[2, 3] For example, the thermal conductivity of silver nanowire could be reduced by 55% when compared with that of bulk silver.[3] On the other hand, thermal conductivity could be enhanced when the size of materials is at the nanoscale. The thermal conductivity of an ultra-drawn polyethylene (PE) nanofiber (diameter: 50 - 500 nm) could reach ~104 W/(m·K), while its macroscale counterpart's thermal conductivity is on the order of 1 W/(m·K).[4] It is explained that the stretching leads the carbon-chain in PE nanofiber to be arranged in the fiber axial direction. Thus, the ultra-drawn PE nanofiber could be seen an 'ideal' single crystalline fiber.[4] Also, thermal behaviors of micro-/nanoscale materials are important to the application. For example, the micro-/nanoscale materials used in microelectronics and optoelectronic devices are under development. In some micro-devices, like modern processors, the power required for high performance can reach 200 W, which needs heat dissipation as efficient as possible.[5] On the other side, like the thermoelectric materials used in solid-state refrigeration devices, they need the thermal conductivity (k) as small as possible.[1, 6] With various needs for

micro-/nanoscale materials with certain thermal conductivity, understandings of the thermal transport in micro-/nanoscale materials are required. In addition to thermal conductivity, the interface thermal resistance also plays an important role in thermal transport of micro-/nanoscale materials. For dissimilar materials, due to the phonon velocity and densities differences, phonon transmission impedance mismatch happens, which finally leads to the interface thermal resistance.[1]

So far, a lot of techniques have been developed to determine the thermal conductivity and interface thermal resistance by experiments, like the 3ω method,[7-9] micro-fabricated devices method,[10] transient thermo-reflectance (TTR) method[11, 12] and so on. Simulation methods like first-principle calculations, molecular dynamic (MD) simulation and Green's function method are also used to predict the thermal conductivity and interface thermal resistance.[13] Understanding the thermal transport is a challenge until now when the characteristic length of the materials reduces to micro-/nanoscale. Since the scattering of heat carriers is more affected by the defects and grain boundaries rather than the intrinsic scattering, the thermal transport mechanism at the macroscale is not applicable. Research about the thermal transport in micro-/nanoscale will need not only the knowledge of thermal transport but also the study of material' microstructure.[2, 14] Yet, there are many challenges in measurement accuracy when characterizing the thermal properties and interface thermal resistance. The reduction in feature size (as small as ~nm) leads to the manufacturing process complexity and the difficulty in controlling the parameters like grain texture, surface chemical residue and porosity.[1]

1.2 Techniques Developed to Characterize the Thermal Transport in Micro-/Nanoscale Materials

To date, the developed thermal measurement techniques include 3ω method,[7, 9] the micro-fabricated device method,[10, 15, 16] time-domain thermo-reflectance (TDTR) method,[1, 17] transient electro-thermal technique (TET)[18, 19] and so on. For the 3ω method, an *AC* current in the form $I_0 \sin\omega t$ is fed to the sample to induce a temperature fluctuation at 2ω. This will cause a small voltage fluctuation at 3ω across the sample. The voltage harmonics ($V_{3\omega}$) is used to determine the thermal diffusivity and thermal conductivity.[7-9] Usually, this technique has high accuracy when measuring the thermal conductivity of bulk materials and the dielectric films with low thermal conductivity. However, the accuracy of this technique is reduced when applied on semiconducting thin film.[1] The micro-fabricated device method makes the sample as the thermal path between suspended islands that are thermally isolated to each other. By employing the temperature differences of different islands and the Joule heat fed to one island, the thermal conductance of the sample is obtained.[15] It takes a long time to fabricate the micro-devices and the contact resistances between the micro-wire and the islands are difficult to analyze. For the TDTR method, by adjusting the relative optical path lengths between the 'pump' pulse and 'probe' pulse, the 'pump' pulse and 'probe' pulse reach the sample one after another. The temperature evolution of the sample surface is detected by the 'probe' pulse. The thermal properties and interface thermal resistance could be achieved by fitting experimental temperature cooling curve with the theoretical model.[20, 21] The TDTR method has been successfully applied on thermal properties of various materials with high accuracy.[13] However, this method could only detect the thermal transport in the film, but not applicable to the thermal transport through extreme thin film.[1] Besides, the laser power absorbed by the sample is still difficult to analyze exactly. The TET method utilizes the self-heating in the

sample and the monitored voltage evolution to determine the thermal diffusivity of micro-/nanoscale one-dimensional materials. This method is proven to be quick and reliable. However, it needs resistance (R) - temperature (T) coefficient (dR/dT) calibration. Since dR/dT is the differentiated value of R against T, its accuracy is easily hindered by the measurement errors of resistance and temperature. For some extremely thin fibers (~nm), it is fragile and easily broken during the calibration, which results in the failure of obtaining R-T coefficient.[18, 19]

1.3 Relationship between Thermal Properties and Microstructures

A lot of factors affect the thermal properties. For example, the thermal conductivity of polymers is dependent on many factors: temperature, crystallinity, crystallite orientation, crystallite size and chain length.[22-27] In this work, we aim at discovering the effect of microstructures in the samples on thermal properties. The micro-structures include the crystallinity, crystallite size, crystallite orientation and chain length. The k of crystalline part is several times larger than the k of amorphous part.[23, 25] The semi-crystalline fiber could be considered as a two-phase system composed of crystallite and amorphous regions. The amorphous phase can be regarded as being distributed uniformly among the crystalline regions. According to Maxwell effective medium theory, the effective thermal conductivity of a mixture (k_e) and the thermal conductivity of crystallite (k_c) could be depicted by the following equation: $k_e / k_c = 1 + 3(\gamma - 1)(1 - \chi) / [(\gamma + 2)(\gamma - 1)(1 - \chi)]$. Here χ is the crystallinity and γ is the ratio of thermal conductivity of amorphous to thermal conductivity of crystallite.[28] It is easily concluded that k increases as crystallinity increases. The orientation effect for polymers could be depicted by an orientation function f_c: $f_c = [3 < \cos^2 \theta > -1] / 2$, ($0 \le f_c \le 1$), among which θ is the angle between the chain direction and the fiber axial direction. < > means the average value over all

crystallites. The polymers show larger *k* in the direction of molecular orientation, while showing smaller value in the normal direction of molecular orientation.[23, 26, 29] To date, little work has been published about the crystallite size dependence of thermal conductivity for semi-crystalline polymers. The thermal conductivity of polymers is typically in the order of 1 W/(m·K), while the thermal conductivity of amorphous part in semi-crystalline polymers is extracted to be at the order of 0.1 W/(m·K).[26] The crystallites could be regarded as in a series, with the junction part of adjacent crystallites is filled with amorphous part. Thus, in the semi-crystalline polymers, amorphous part is the main obstacle to thermal transport. Under this situation, very little work focuses on the crystallite size effect on thermal conductivity. Experimental data about the chain length dependence of thermal conductivity for polymers is rare. Through MD simulations, the thermal conductivity of single extended polymer chains is found to be one to two orders of magnitude higher when the chain length is increased from 1 to 10^4 nm.[30, 31]

For graphene-based materials, defects, grain size, substrate and so on affect the thermal conductivity jointly.[32-37] The thermal conductivity of suspended graphene shows discrepancy from the former research. It is reported to be as high as ~5300 W/(m·K) by using micro-Raman spectroscopy, and the sample is ~20 μm in length.[38] Other researchers stated a smaller thermal conductivity [2500 W/(m·K)] for suspended graphene based on micro-Raman spectroscopy.[39] The discrepancies may come from the different methods of determining laser power absorbed by graphene as well as the different consideration for the segment of graphene supported on SiO_2.[39] The defects in graphene include intrinsic defects such as point defects, line defects, vacancies, grain boundaries (GBs) and extrinsic defects like foreign atoms.[40] So far, most of the studies about the defects effect on thermal transport are through simulation methods.[36, 37, 41-43] Experimental data

relating defects with the changes in thermal properties are urgently needed. Liu's *et al.* work shows that thermal conductivity decreases with increased GB fraction or GB energy. It has been demonstrated that the polycrystalline structures with non-uniform grain distribution show higher thermal conductivity than samples with uniform grain distribution when the grain sizes reach a certain level. When the grain sizes become smaller, the grain size distribution shows negligible effect on thermal conductivity.[36] Besides, thermal conductivity of polycrystalline structures decreases with decreasing grain sizes.[42, 44] The thermal conductivity of supported graphene is much lower than that of suspended graphene. Researchers reported that the *k* of supported graphene on SiO_2 is ~600 W/(m·K) and the *k* of supported graphene on Au is ~370 W/(m·K).[39, 45, 46] A generally accepted explanation for the thermal conductivity reduction in supported graphene is that the phonon leakage at the graphene/substrate interface leads to the reduction of the long-wavelength phonons' mean free path. This finally results in smaller thermal conductivity of supported graphene.[46]

It is also found that different coupling strengths caused by different choices of substrates are critical for thermal transport in supported graphene.[33, 34] The thermal conductivity of graphene supported by SiO_2 was reported to be ~600 W/(m·K), which is relatively larger than that of graphene supported by PMMA [~270-360 W/(m·K)]. Enormous carbon atoms in PMMA leads to easier phonon coupling between PMMA and carbon, which results in strong thermal conductivity reduction.[46, 47] A strong graphene-substrate coupling strength significantly increases the ZA mode scattering in graphene, which leads to more reduction of thermal conductivity when coupling strength increases.[32, 35] However, some other researchers found that a higher graphene-substrate coupling strength increases the thermal conductivity by using the spectral energy density (SED)

analysis.[33] Different simulation methods cause the discrepancy. Experiments are needed to further explore the relationship between the thermal conductivity of supported graphene and graphene-substrate coupling strength. The thermal conductivity of suspended and supported graphene is also reported to be strongly dependent with the size of graphene flake.[48] Both theoretical predications and experimentally obtained data show that the k of suspended graphene has a ~ log$L$ dependence, where L is the length of the graphene flake.[48-50] The k of supported graphene could be reduced by ~85% when the sample length is reduced from 5.0 to 1.0 μm.[45] One proposed mechanism is that the increase of the sample size results in the excitation of low-frequency acoustic phonons, which finally makes contribution to the thermal transport.[48, 51] However, the thermal conductivity of graphene will be restricted by the phonon-grain boundary scattering as graphene flake become very large.[51]

Thermal properties of carbon fiber (CF) are directly related with the microstructures.[52-54] Factors affecting the thermal transport in CF include the degree of disorder, crystallite size, crystallinity as well as crystal orientation. These factors are not independent but correlated with each other. The smaller degree of disorder usually accompanies with larger crystallite size, smaller carbon layer lattice spacing and better crystal orientation, which finally leads to a higher thermal conductivity.[52-54] In CFs, the atomic structure consists of carbon atoms in the arrangement of hexagonal pattern, which is similar to the aromatic rings in graphene.[55] According to the adjacent graphene sheets packing style, there are three kinds of graphene sheets packing pattern: graphitic, turbostratic, and a hybrid structure of graphitic and turbostratic.[55] The thermal conductivity of graphitic CF could be 70 times larger than that of turbostratic CF.[56] With the treatment temperature increase, the turbostratic structure in CF undergoes transition to graphitic carbon. The increased

order of the graphene sheets will result in higher thermal conductivity.[57] Larger crystallite size results in larger thermal conductivity in CFs. With the removal of defects like vacancies, impurities, or interstitial atoms in pitch-based CFs, the lattice spacing between two carbon layers decreases and the crystallite size increases. Correspondingly, *k* of CFs increases with increased crystallite size.[52, 54] The thermal conductivity increases with the increased crystallinity in the materials. After being annealed at 2800 °C for 20 h, there is an obvious crystallinity improvement in carbon nanofibers. *k* of the carbon nanofiber could be increased from 4.5 to 160 W/(m·K) after being annealed at 2800 °C.[58]

1.4 Background of Phonon Scattering

Usually, XRD is used to determine the crystallinity and crystallite size for semi-crystal materials. Raman spectroscopy provides the information about molecular vibration modes. However, for micro-/nanoscale materials, it is difficult to obtain sufficient intensity to determine the crystallite size and crystallinity since the materials are too small to do the XRD test. Former research proposed that the thermal conductivity is limited by defects at low temperatures. The thermal conductivity in the lowest temperature range could be fitted and used to give insight of the microstructure of bulk graphite and CFs.[52, 53] In this work, instead of using thermal conductivity at low temperatures, we will introduce another parameter: thermal reffusivity (inverse of thermal diffusivity), to study the phonon scattering and characterize the grain boundaries and defects in samples. The thermal reffusivity eliminates the heat capacity parameter when considering the phonon scattering. This theory is not only applicable to graphite, but also applicable to carbon-based materials, polymers as well as DNA.[59-62] Furthermore, the mean free path due to grain

boundary/defects is determined by 0 K-limit phonon scattering. We will introduce the advantages of utilizing thermal reffusivity in the details later.

In polymers and carbon-based materials, the thermal transport is dominated by phonon scattering. Phonon is defined as the elastic wave packet of lattice vibrations. There are two modes of phonons based on the adjacent atoms vibration mode. For the acoustic mode, the neighboring atoms are in phase. On the contrary, the neighboring atoms which are out of phase are defined as optical mode.[63] It is well known that the lattice thermal conductivity could be defined as $k = 1/3\sum C_i v_i l_i$, where i denotes each phonon mode. C is the volumetric heat capacity, v is the phonon group velocity and l is the phonon mean free path.[64] Since the group velocity of optical phonons is much smaller than that of acoustic phonons, the thermal transport in polymers and carbon-based materials is dominated by the acoustic phonon scattering.[30] There are two kinds of phonon scattering: phonon-phonon scattering and phonon-grain boundary/defect scattering. Phonon-phonon scattering is intrinsic scattering that the phonons are scattered by other phonons and exists in a pure crystal. The phonon-phonon scattering is dependent on the temperature. Another kind of phonon scattering is called extrinsic scattering. The phonons are scattered by grain boundaries and defects like vacancies, impurities, or interstitial atoms. The phonon-grain boundary/defect scattering is independent of temperature and is only related with microstructure of materials.[65] As temperature decreases to 0 K, the phonon-phonon scattering is frozen out, leaving only the phonon-grain boundary/defect scattering.[66] Thus, the thermal reffusivity at 0 K limit (residual thermal reffusivity) is directly related with the grain size and defect level. It is possible for us to utilize residual thermal reffusivity to determine the magnitude of grain size.

1.5 Scope of Present Work

In this work, we develop a Johnson noise electro-thermal (JET) technique to directly characterize the k and α of one-dimensional micro-/nanoscale materials. The k of a glass fiber with a diameter (d) of 8.82 μm is measured using JET technique. The measured value 1.2 W/(m·K) agrees well with the value using a standard technique in our laboratory. The JET technique could characterize the thermo-physical properties of micro-/nanoscale materials without calibrating the sample's resistance-temperature coefficient. Combining transient electro-thermal (TET) technique with a cryogenic system, we characterize the temperature-dependent behavior (down to 22 K) of thermal diffusivity and conductivity of UHMWPE fibers in anticipation of observing the phonon scattering rate against temperature and of freezing out high-momentum phonons to clearly observe the defect effects. By studying the temperature-dependent behavior of thermal reffusivity (Θ, inverse of thermal diffusivity) of UHMWPE fibers, we are able to quantify the defect effect on thermal conductivity. After taking out the amorphous region's effect, the residual thermal reffusivities (Θ_0) for the studied two samples at the 0 K limit are determined as 3.45×10^4 and 2.95×10^4 s/m^2, respectively. The obtained defect-induced low-momentum phonon mean free paths are smaller than the crystallite size in the (002) direction (19.7 nm) determined by XRD. The grain boundary thermal conductance (G) is then evaluated as $G \approx \beta\rho c_p v$ with sound accuracy. At room temperature, G is around 3.73 GW/(m^2·K), comparable to that of interface with tight atomic bonding.

We also develop a differential technique to characterize the thermal conductivity of giant chemical vapor deposition (CVD) graphene supported by PMMA. Our graphene size is ~mm, far above the samples studied in the past. The thermal conductivity of 1.33-layered, 1.53-layered,

2.74-layered and 5.2-layered supported graphene is measured as 365, 359, 273 and 33.5 W/(m·K), respectively. We use the thermal conductivity of graphene to characterize the defects level in CVD graphene. Raman spectroscopy is also used to prove the defects level in each kind of graphene. The structure domain size of lignin-based CFs is first investigated by XRD, Raman scattering and phonon scattering at the 0 K limit. The sizes obtained by the three methods are well consistent with each other. Our thermal reffusivity study shows that the phonon scattering in the CFs are dominated by the grain boundaries and defects. The thermal conductivity of the annealed CFs is significantly increased by more than ten-fold after being annealed at ~2770 K. This is due to the graphitic structure improvement and increase of graphitic contents in the CFs. The annealing effect on microscale structure and thermal transport has been investigated by the microscale Raman scanning from slightly annealed to strongly annealed region. The cluster size shows one-fold increase after being annealed. This directly uncovers the structure improvement by annealing. We also find that the inverse of thermal conductivity is linearly proportional to the annealing temperature in the range of 1000-2000 K.

CHAPTER 2 MICROSCALE THERMAL CHARACTERIZATION USING JOHNSON NOISE

This chapter reports the thermal conductivity and thermal diffusivity measurement of glass fiber by using Johnson noise. In section 2.1, we analyze the accuracy of new developed system response of pre-amplification and temperature measurement. Experimental principle and setup and physics model development are introduced in section 2.2. Section 2.3 introduces the results. The thermal conductivity obtained by JET technique is also verified by TET technique.

2.1 System Response and Thermal Measurement Accuracy

2.1.1 System response of pre-amplification

Johnson noise, caused by the thermal agitation of the charge carriers (usually electrons), generates an open circuit voltage across any resistance, which is random with a zero mean over a long time. It always happens regardless of any applied bias. It was first observed by Johnson and the voltage variance per hertz of bandwidth was given by the Nyquist relation: $\overline{<V_n^2>} = 4k_B RT$.[67, 68] Here R is resistance in ohm, T is the temperature in Kelvin, and k_B is the Boltzmann constant. In a realistic resistor, it is almost a white noise, which means the power spectral density is nearly constant throughout the frequency domain up to GHz.[67] Johnson noise thermometer (JNT) has been developed according to this principle.[69, 70] In this work, we aim at measuring the thermal conductivity of microscale sample directly by using Johnson noise.

Johnson noise is very small. For instance, given the resistance is 1 kΩ and it is measured under room temperature, the order of the Johnson noise is ~10^{-17} V^2/Hz. It is necessary to amplify it before using a dynamic signal analyzer to detect it. Before we conduct thermal property

measurement using Johnson noise, the system response and measurement accuracy are fully evaluated. In this experiment setup, the to-be-measured resistor is placed in a chamber to minimize external noise injection. The Johnson noise across the resistor is first amplified by a low noise amplifier (SR560). The amplifier output is connected to a dynamic signal analyzer (SR785) through a coaxial cable. All the coaxial cables in this experiment are wrapped with aluminum foil to eliminate external noise. In this experiment, carbon film resistors with different resistance values are used under room temperature to measure their Johnson noise. The voltage spectral density from 50 to 102.4 kHz is used for noise evaluation. 1000 root mean square (RMS) data averages are collected to minimize statistical fluctuations. Instrument noise resulted from the amplifier and dynamic signal analyzer has been proven to be constant with a variation less than 1% during the experiment.

The voltage spectral density of Johnson noise is shown in the inset of Fig. 2.1 for several resistors with different resistance. We could see that the spectrum is flat. This is consistent with the fact that Johnson noise is constant over a very wide frequency range. The average voltage spectral density of Johnson noise (averaged over 50 to 102.4 kHz of the spectrum) is shown in Fig. 2.1 for resistance ranging from 99 to 4630 Ω. The voltage spectral density can be expressed as: $S_V = g^2(4k_BTR + S_0)$, where S_0 is the output voltage noise of the preamplifier and g is the gain of the preamplifier, T is the room temperature. In our experiment, the gain is 80 dB. It is constant among the frequency domain. Figure 2.1 shows a very good linear relationship between the measured voltage spectral density and the resistances. When the resistance goes down to zero, the measured noise is supposed to be the output noise of the preamplifier. Linear fitting based on the above equation is conducted. In the manual of SR560, when frequency is between 1 and 100 kHz,

and the source resistance is between 10 Ω and 10 kΩ, the preamplifier's own noise remains constant. In this fitting, S_0 could be assumed to be constant considering the frequency range and resistances of the resistors used in this experiment and it is determined as 1.424×10^{-17} V^2/Hz. This value is very reasonable since the output noise of SR560 is given 4 nV/$\sqrt{\text{Hz}}$ in the data manual, namely 1.6×10^{-17} V^2/Hz. The slope of the fitting is $4k_BT$ according to the Nyquist relation. In this experiment, the slope is determined as 1.62×10^{-20} J. The Boltzmann constant is obtained by dividing the slope with $4T$. The room temperature is 295.1 K when the experiment is conducted. The specific value of the Boltzmann constant is determined to be 1.375×10^{-23} J/K. This result agrees nicely with the standard value of Boltzmann constant (1.381×10^{-23} J/K) with a relative error of 0.36%. We feel very confident of the preamplifier, dynamic signal analyzer and the connections in the experiment.

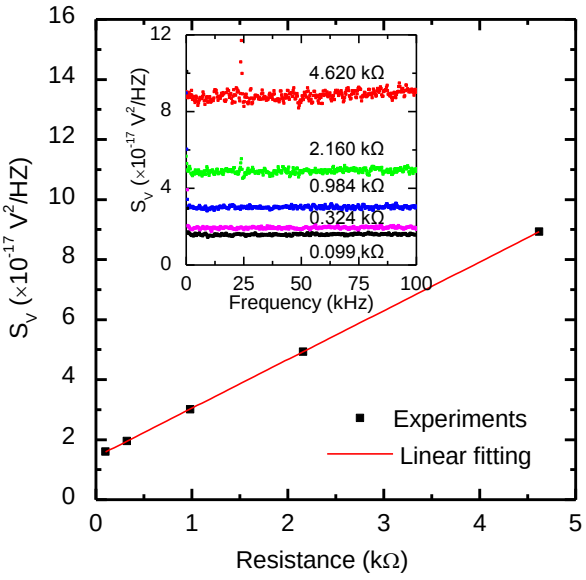

Figure 2.1 Variation of measured Johnson noise voltage spectral density against resistance. Excellent linear relation is observed between them. The inset shows the voltage spectral density of Johnson noise measured across different resistors, clear Johnson noise increase is observed for an increased resistance.

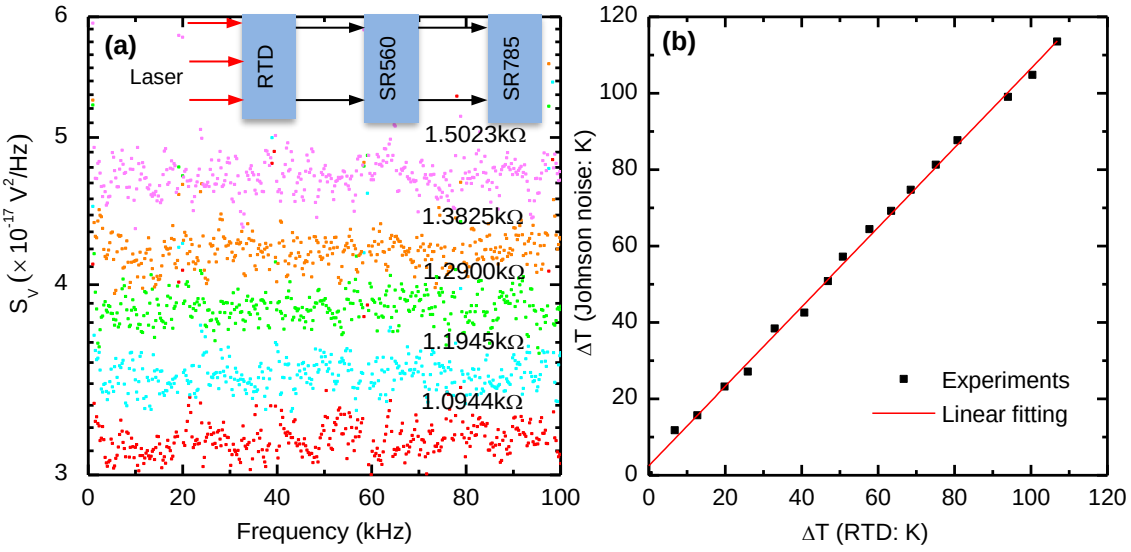

Figure 2.2 (a) Voltage spectral density of Johnson noise measured across the RTD, the inset shows the schematic setup for evaluation of temperature measurement accuracy, RTD: Resistance temperature detector; SR560: Preamplifier; SR785: Dynamic signal analyzer. (b) Temperature rise obtained through Johnson noise and RTD, respectively. The slope of the fitting line is 1.04.

2.1.2 Temperature measurement accuracy evaluation

In the above section, the measurement accuracy which includes amplification and signal transmission of the whole system is carefully studied and verified. Then we design an experiment to test the temperature measurement accuracy before we apply the technique to temperature probing for thermo-physical properties measurement. The inset in Fig. 2.2(a) shows the schematic setup of this accuracy test. Here, a resistance temperature detector (RTD) is used as the sample in this experiment. It is placed in a vacuum chamber to minimize the environment influence such as air flow and fluctuation. A laser beam is used to heat the RTD. Different from using a voltage source to heat the sample, the laser will not cause any voltage noise in the sample. As the laser energy level is increased, the temperature of the RTD will increase as well, thus causes its resistance to rise. The resistance of RTD has an exact relationship with temperature:

$R_t = R_0(1 + At + Bt^2)$, where R_0 is the resistance at 0 °C, and t is temperature in degrees Celsius. A and B are coefficients given by the product data. The temperature of the RTD can be obtained exactly from the resistance which is measured by using a 6½ digital multi-meter (Agilent 34401A). To measure the resistance accurately, a 10 kΩ measurement range is chosen, and the operating current is 100 μA. The temperature of the RTD can also be obtained by measuring the Johnson noise, and compared with the one determined by using resistance. This will provide excellent evaluation of the direct temperature measurement accuracy based on Johnson noise.

The voltage spectral density during frequency domain is shown in Fig. 2.2(a). The five peaks in the spectrum are caused by the external noise. Data lying on or close to the baseline is used to calculate the temperature of RTD. The voltage spectral density and temperature have the following relationship: $S_V=g^2(4k_BTR+S_0)$. The output noise of the preamplifier remains constant during the experiment, so we use 1.424×10^{-17} V^2/Hz for S_0 to calculate the temperature. We mainly focus on the temperature rise since our later experiment aims at probing the thermal conductivity, which is determined by the temperature rise. The exact temperature of the sample is less important in our experiment. By comparing the temperature rise obtained from calculation of Johnson noise and resistance of RTD respectively, the accuracy of temperature measurement of JET is determined. Figure 2.2(b) shows the result of the temperature measurement accuracy evaluation. The temperature rise is obtained by subtracting the temperature with zero laser input power. The slope of the fitting line is 1.04. It means that temperature rise obtained from the Johnson noise method is very reasonable and reliable. Compared with the standard method using RTD, it has a very small deviation (4%).

2.2 Physics and Experimental Details for Johnson Noise Electro-Thermal Characterization

2.2.1 Experimental principle and setup

Schematic of the setup to measure the thermal conductivity of a one-dimensional material based on Johnson noise is shown in Fig. 2.3(a). In this JET technique, if the sample is non-conductive, it will be first coated with iridium to make it conductive. Then the sample is suspended between two copper electrodes. The sample is connected with a resistor which has a greater value of resistance (R_0=55.93 kΩ). A voltage source (SIM928) is used in this electrical circuit to offer a current to induce Joule heating in the sample. Both sample (R_s) and the resistor (R_0) are placed in a vacuum chamber to eliminate external noise. The two terminals of the sample are also connected to the feedthrough of the chamber. And then another terminal of the feedthrough is connected to the preamplifier (SR560) through a coaxial cable. The output of the preamplifier is connected to the dynamic signal analyzer (SR785) through a coaxial cable. All the coaxial cables are wrapped with aluminum foil to minimize the effect of external noise.

Some points need to be explained here. First, the sample is very fine and fragile, so a resistor (R_0) with a large resistance is used to limit the current in the sample and thus protect it. Second, we measure the bias over the sample (V_{R_s}) by using a digital multi-meter (Agilent 34401A), with the assumption that the resistance of R_0 remains constant during the whole experiment. This is reasonable since the heating power for this resistor is very negligible. Therefore, the real resistance of the sample is obtained through calculation as $R_0 V_{R_s} / (V - V_{R_s})$, where V is the overall voltage applied to the circuit. Third, what we obtained is only the Johnson noise without shot noise. When the length of sample is much larger than the electron-photon scattering length ($L \gg l_{e\text{-}ph}$), the shot noise vanishes.[71, 72] The electron's thermal conductivity can

be expressed as: $k=Cv_F l_{e\text{-}ph}/3$. v_F is the particles' velocity, C is the heat capacity per unit volume, and $l_{e\text{-}ph}$ is the mean free path.[65] The electron mean free path $l_{e\text{-}ph}$ of iridium is calculated to be 2.04 nm.[73] The length of the sample used in the experiment is much larger than 2.04 nm. Fourth, the voltage source also has output voltage noise even though it is much smaller than that of a current source. Its effect on R_s and R_0 can be calculated like voltage of two resistors in series. The measured voltage spectral density is expressed as:

$$S_V = \left(\frac{R_0}{R_0 + R_S}\right)^2 \cdot 4k_B T_s R_s + \left(\frac{R_S}{R_0 + R_S}\right)^2 \cdot (4k_B T_0 R_0 + < V_0^2 >) + S_0 \qquad (2.1)$$

Where T_0 is room temperature and the temperature of R_0, and T_s is the sample temperature. $< V_0^2 >$ is the output noise of the voltage source and S_0 is the output noise of the preamplifier. Since R_0 is much larger than R_s (approximate 83 times larger in this experiment), the measured voltage spectral density can be approximately equal to $4k_B T_s R_s + S_0$ with a very high accuracy. The relative error of this approximation is smaller than 2% in this experiment. If the sample is directly connected with the voltage source, the measured voltage spectral density is:

$$S_V = 4k_B T_s R_s + < V_0^2 > + S_0 \qquad (2.2)$$

Thus, the value of output noise of voltage source is larger than that of the sample, the effect of voltage source becomes not negligible. A resistor with a much larger resistance is helping to minimize the effect of output noise of voltage source on the Johnson noise measurement.

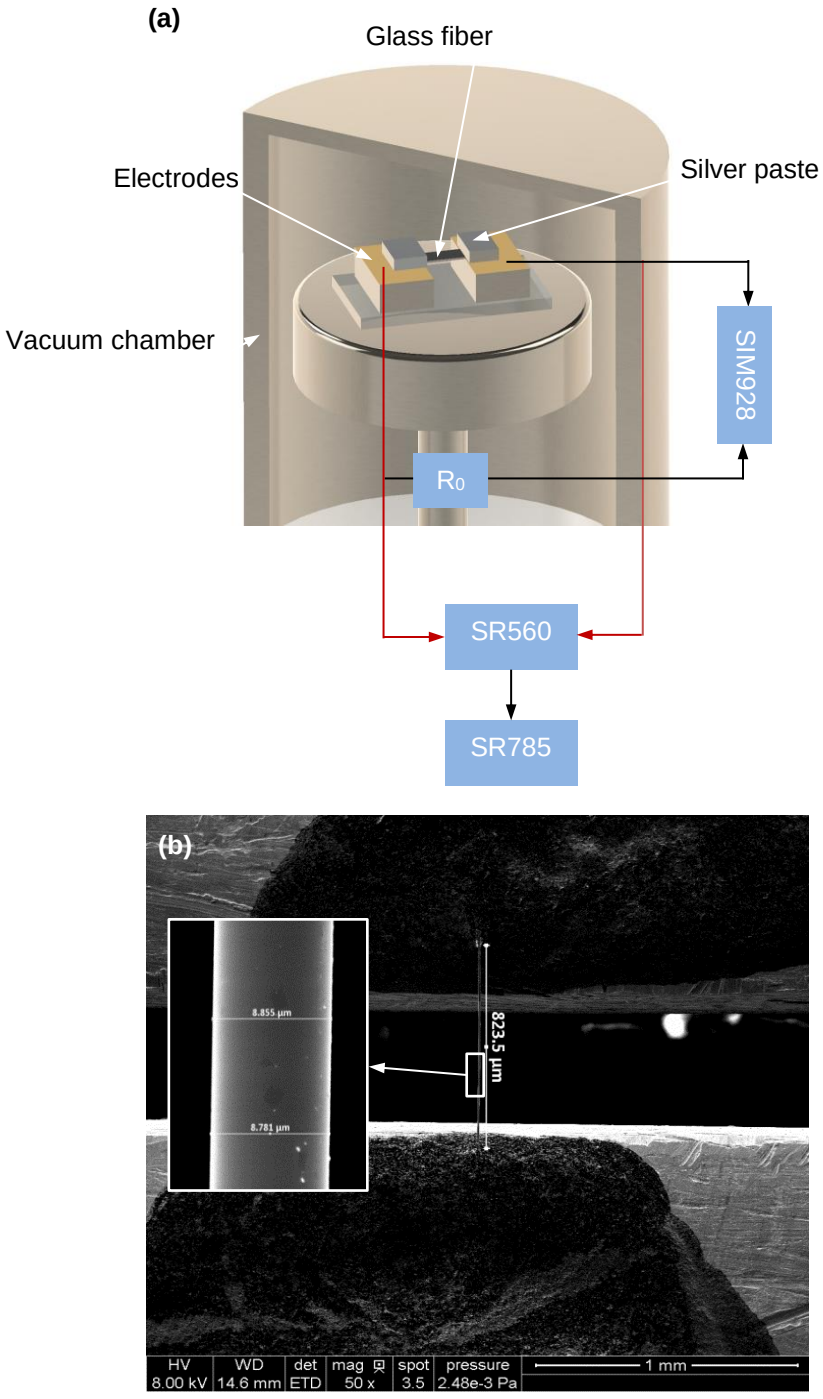

Figure 2.3 (a) Schematic of the setup for the new JET technique, SR560: Preamplifier; SR785: Dynamic signal analyzer; SIM928: Voltage source; R_0: Resistor which has a large resistance. (b) SEM image of the glass fiber measured in this work. The inset shows details of the diameter and surface morphology.

2.2.2 Physics model development

Figure 2.3(a) shows that under DC current heating, the heat transfer in the sample is a one-dimensional heat conduction problem. D. F. Santavicca *et al.* developed a 1-D energy loss model for electron in single-walled carbon nanotubes.[74] In their work, the hot electron diffusion, the energy dissipated internal to the tube and phonon emission were taken into consideration (p_{ph}) when building the governing equation. Different from us, they measured p_{ph} in experiment. But in our analysis, we derive the final average temperature rise with the effect of radiation. In this experiment, the electrical heating power has the form of I^2R_s. It varies with the change of the resistance of the sample. Since the copper electrodes used in this experiment are much larger than the sample dimension, the temperature of the electrodes can be assumed constant even though a small current is flowing through them. The boundary condition can be described as $\Delta T(x=0) = 0$, where $\Delta T = T - T_0$, T_0 is the room temperature. The governing equation is

$$\frac{\partial\left(\rho c_p T\right)}{\partial t} = k\frac{\partial^2 T}{\partial x^2} + \dot{q} - \frac{16\varepsilon k_s\left(T - T_0\right)T_0^3}{d} \quad , \tag{2.3}$$

where ρ, c_p and k are the density, specific heat and thermal conductivity of the sample, respectively, $\dot{q}$ is electrical heating power per unit volume. It has the form of

$$\dot{q} = \frac{I^2 R_s}{AL} \quad , \tag{2.4}$$

where R_s is the resistance of the sample and it can be detected instantly when measuring the Johnson noise. A and L are the cross-sectional area and length of the sample, respectively. $16\varepsilon k_s\left(T - T_0\right)T_0^3 / d$ describes the effect of radiation for small temperature increases [$(T-T_0)/T_0 \ll 1$], ε and k_s are emissivity and Stefan-Boltzmann constant, and d is the sample diameter. When it reaches steady state, $\partial(\rho c_p T)/\partial T = 0$, and the final average temperature rise which is averaged over the sample length is:

$$\Delta T = \frac{I^2 R_s}{LAa}\left(1 - \frac{\tanh(mL/2)}{(mL/2)}\right), \tag{2.5}$$

where a is $16\varepsilon k_s T_0^3 / d$, and m is $\sqrt{a/k}$. Völklein *et al.* got similar temperature derivation for 1-D heat transport in single metallic nanowires. They also neglected the effect of heat convection and took the radiation and conductive thermal transport into consideration.[75] Normally, the thermal conductivity of glass fiber is ~1.2-1.4 W/(m·K) at room temperature, the thermal conductivity due to radiation effect is determined according to the equation: $16\varepsilon k_s T^3 L^2 / (d\pi^2)$.[76] It is around 0.1 W/(m·K) for the glass fiber used in this experiment when the emissivity is 0.5. The exact effect of radiation will be subtracted to get the real thermal conductivity of glass fiber. Details about this consideration are given in later section.

2.2.3 Methods for data analysis to determine thermal conductivity of the sample

From the above description, the sample and resistor are in series, and a voltage source is used to offer a current to induce Joule heating. The overall voltage ranges from 5 to 20 V with a step of 0.5 V. We use the voltage over the sample, the voltage over the sample and resistor, and the resistance of resistor R_0 to obtain the resistance of the sample, and thus obtain the current in the sample. After obtaining the voltage spectral density, the data in the frequency range of 50 to 102.4 kHz are used to calculate the RMS data average. 1000 root mean square (RMS) data averages are collected to minimize the statistical fluctuations. The total voltage spectral density is:

$$S_V = g^2\left[4k_B(T_0 + \Delta T)R_s + S_0\right] \tag{2.6}$$

where S_0 is the output noise of preamplifier, ΔT is $I^2 R_s / LAa \cdot [1 - \tanh(mL/2)/(mL/2)]$. Here, S_0 is 1.424×10^{-17} V^2/Hz which is determined in the above experiment when determining the Boltzmann constant. Then the temperature rise is calculated out according to Eq. (2.6). After

obtaining the temperature rise, we plot the temperature rise (ΔT) against the input power of the sample (I^2R_s), and fit it with Eq. (2.5) to obtain thermal conductivity.

2.3 Results and Discussion

The scanning electron microscope (SEM) images of the glass fiber measured in this work are shown in Fig. 2.3(b). The inset shows details of the diameter and surface morphology. The diameter and length of the sample are 8.82 and 823.5 μm, respectively. The initial sample resistance is 673 Ω. During the JET test, the sample is placed in a vacuum chamber. The pressure of the chamber is remained under 2 mTorr to minimize the heat convection effect. A DC voltage bias ranging from 5 to 20 V is applied to this electrical circuit. Figure 2.4(a) shows the voltage spectral density of Johnson noise measured under two different overall voltages. Figure 2.4(b) shows the sample resistance variation against the input power of the sample. Sound linear fitting is obtained between sample resistance and the input power of the sample. This is physically expectable since the temperature rise is linearly proportional to the heating level within a moderate heating range, and the electrical resistance changes with temperature linearly. We fit the temperature rise against input power of the sample based on Eq. (2.5), and the experiment data and fitting data are shown in Fig. 2.4(c). The glass fiber and iridium have emissivities of 0.92 and almost 0 at room temperature. In this experiment, we use an emissivity of 0.5 in the fitting (Upper part of the glass fiber is coated with iridium and the lower half is not). The instrument input noise is 1.424×10^{-17} V^2/Hz and the sample's thermal conductivity including the effect of iridium is characterized as 1.31 W/(m·K). Equation (2.5) has taken the effect of radiation into consideration but not the effect of iridium. The real thermal conductivity of glass fiber is obtained according to Eq. (2.7) as

$$k = k_{e0} - \pi\delta / 4d \cdot k_{Ir} \tag{2.7}$$

Where k_{e0} is the measured thermal conductivity obtained in original fitting, δ is the thickness of iridium, k_{Ir} is the thermal conductivity of iridium. The thermal conductivity of iridium is determined to be 60 W/(m·K).[73] Thus, the real thermal conductivity of glass fiber is determined as 1.20 W/(m·K).

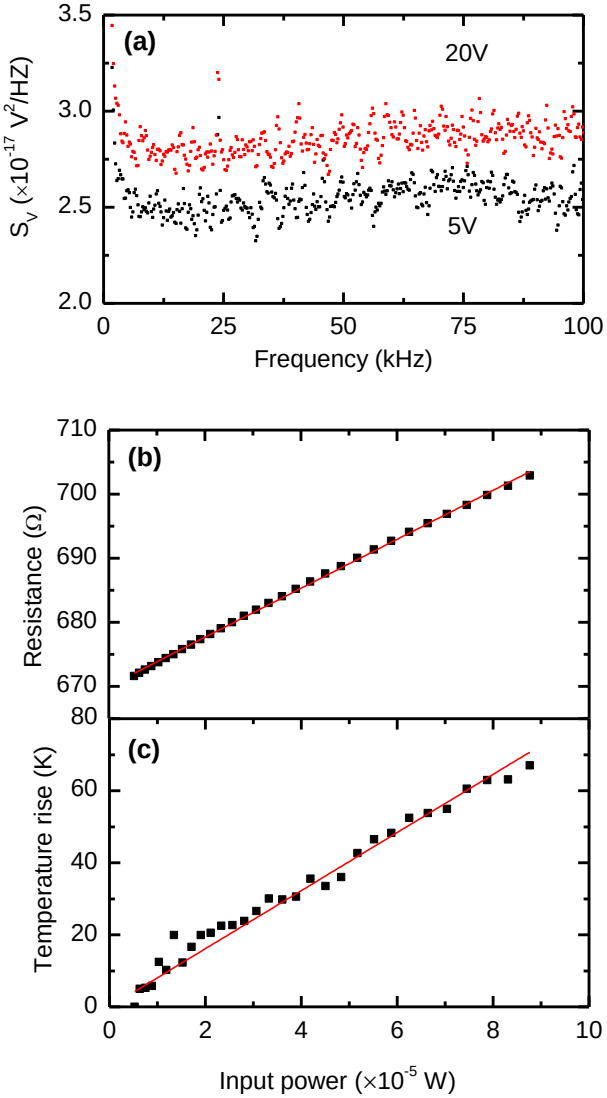

Figure 2.4 (a) Voltage spectral density of Johnson noise measured with two applied bias. (b) The fitting of sample resistances against input power of the sample. (c) Variation of temperature rise against input power of the sample. The thermal conductivity of the fiber is determined by fitting the $\Delta T \sim I^2 R_s$ relation using Eq. (2.5).

We also use the same sample to do TET test to acquire the thermal conductivity. The TET technique has been widely used to measure the thermal diffusivity/conductivity with very high accuracy. During the TET test, the sample is placed in a vacuum chamber, the pressure of the chamber is remained under 2 mTorr. DC current is feed through the sample to induce Joule heating. The temperature rise of the sample causes the resistance of sample to rise, and thus the voltage over the sample increases. We use an oscilloscope to monitor the voltage evolution and then save the data. The heat transfer problem is one dimensional along the fiber axial direction, the normalized temperature rise, which is defined as $T^*(t)=[T(t)-T_0]/[T(t\to\infty)-T_0]$, can be written as:[18]

$$T^* = \frac{96}{\pi^4}\sum_{m=1}^{\infty}\frac{1-\exp[-(2m-1)^2\pi^2\alpha t/L^2]}{(2m-1)^4}. \tag{2.8}$$

Where $T(t)$ is the average temperature of the sample along the fiber, T_0 is the room temperature, α is the thermal diffusivity, L is the length and t is the time. After obtaining the temperature evolution *T-t*, we use least square fitting to obtain the thermal diffusivity of the sample. The normalized temperature rise is calculated according to Eq. (2.8) by using different trial values in a MATLAB program. The trial value giving the best fit of the experimental data is regarded as the measured thermal diffusivity of the sample. The thermal conductivity (k_{e0}) of the glass fiber ruling out the effect of radiation can be calculated as

$$k_{e0} = \alpha_e \rho c_p - \frac{16\varepsilon k_s T^3 L^2}{\pi^2 d} \tag{2.9}$$

Where α_e is the measured thermal diffusivity, and T is the average temperature of the sample during TET test. In this TET test, the current is ranging from 0.16 to 0.24 mA with a step of 0.02 mA. Figure 2.5 shows the typical experiment data and the fitting line. The measured thermal diffusivity

(α_e) is determined as 9.40×10^{-7} m^2/s. The density and heat capacity of the glass fiber are determined to be 2070 kg/m^3 and 745 J/(kg·K) at room temperature.[73, 77] The thermal conductivity of glass fiber after subtracting the effect of radiation is calculated as 1.34 W/(m·K) according to Eq. (2.9). According to Eq. (2.7), the real thermal conductivity of glass fiber is determined to be 1.26 W/(m·K) after ruling out the effect of iridium. This value agrees very well with that obtained by the JET technique: 1.20 W/(m·K). This strongly proves the high measurement accuracy of the JET technique reported in this work. The thermal conductivities obtained through these two methods are consistent with the reference value which is 1.3 W/(m·K).

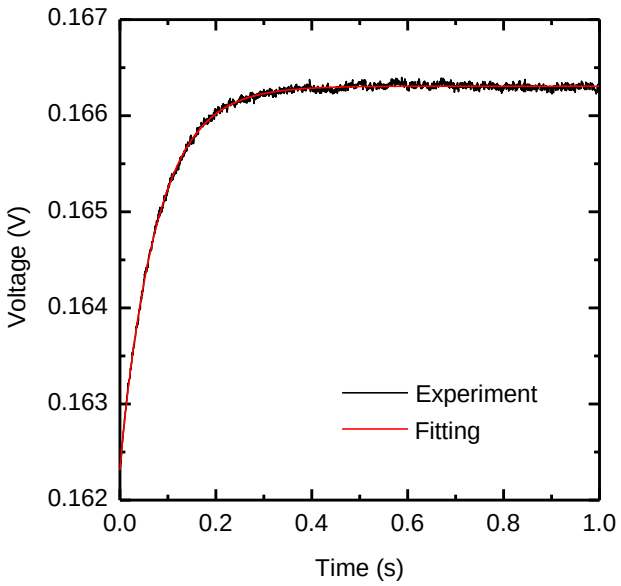

Figure 2.5 TET fitting result curve when a square current of 0.24 mA is applied to the sample.

Here, we discuss the measurement uncertainty of the JET technique. According to the temperature measurement accuracy evaluation test, the temperature measurement uncertainty is 4%. During the temperature rise-input power of the sample fitting, the fitting uncertainty is 1.5%. The diameter and length of the glass fiber are measured by using a scanning electron microscope.

The relative errors of the diameter and length are both less than 1%. The final measurement uncertainty of thermal conductivity is estimated less than 5%.

CHAPTER 3 ENERGY TRANSPORT IN MICROSCALE POLYETHYLENE CRYSTALLINE FIBERS AND PHONON SCATTERING STUDY

This chapter reports on the temperature-dependent behaviors (down to 22 K) of thermal diffusivity and conductivity of UHMWPE fibers in anticipation of freezing out high-momentum phonons to clearly observe the defects effect. Section 3.1 introduces the characterization of sample structure. In section 3.2.1, thermal conductivity and thermal diffusivity against temperature are studied. The defect effect on thermal conductivity and domain size uncovered by 0 K limit phonon scattering is studied in section 3.2.2.

3.1 Sample Structure Characterization

Commercial UHMWPE fibers (Spectra 900) with high strength and extended chains from Minifibers Company are used in this experiment. Their modulus and tensile strength is 125 GPa and 2.7 GPa, respectively. The density is 0.974 g/cm^3.[78] The molecular mass is usually between 2 and 6 million Dalton for UHMWPE fibers. Figure 3.1(a) shows a schematic molecular arrangement in crystalline regions in PE fibers. Figure 3.1(b) shows the experimentally reported crystal structure of PE.[79] PE chain has an extended planar zigzag conformation. The PE chains with different colors shown in Fig. 3.1(a) are on different lamellae. Since the inter-chain Van der Waals force is much weaker than the intra-chain covalent bonds, thermal conductivity of PE along the chain direction [*c* direction in Fig. 3.1(a) and Fig. 3.1(b)] is much larger than those along the other two directions.[23] Further investigation of the molecular structure of our samples shows that the *c*-direction is highly aligned along the fiber axial direction along which the thermal conductivity was measured. More details about the crystallite orientation will be given later.

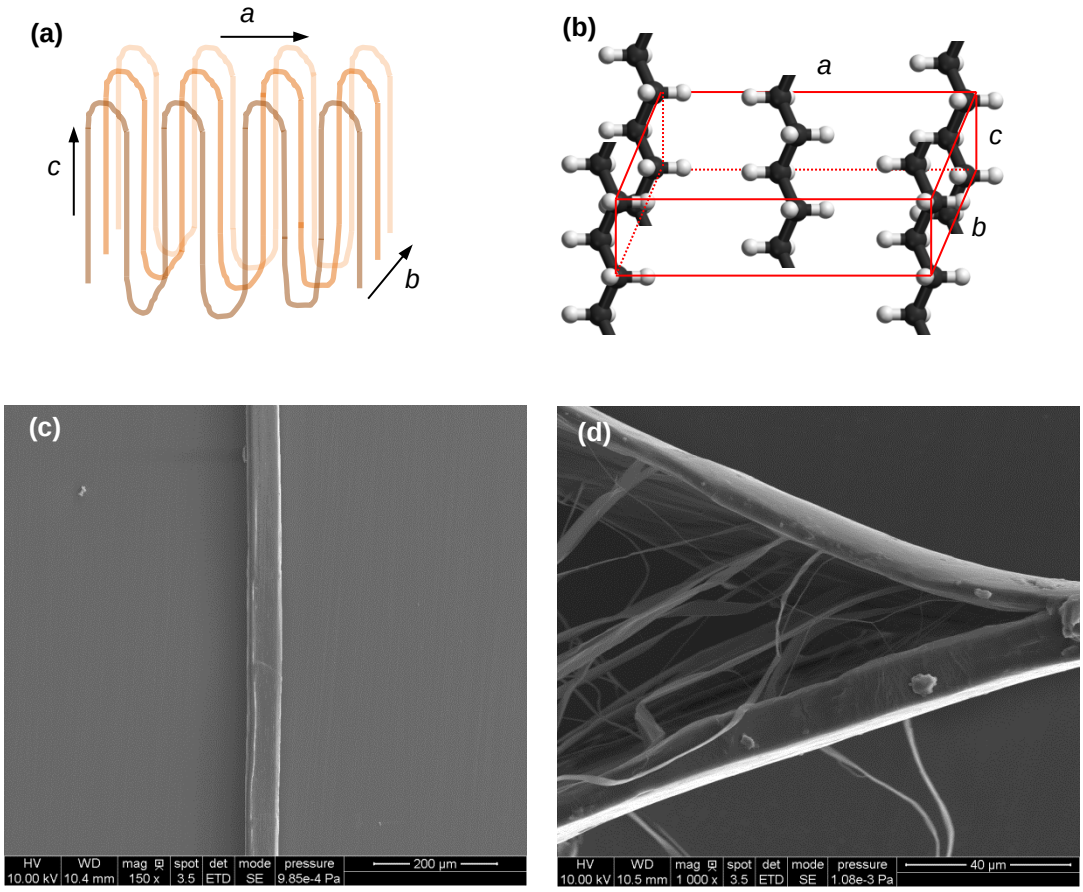

Figure 3.1 (a) Schematic molecular arrangement in crystalline PE fibers. The chains are carbon chains. The carbon chains shown in different colors are located on different lamellae. *c* direction is always along the carbon chain direction. *a*=7.41 Å, *b*=4.94 Å and *c*=2.55 Å. (b) Experimentally reported crystal structure of PE. (c) SEM image of the sample before it is split into several fine fibers. (d) Sample that is mechanically broken into fine fibers to illustrate its internal stranded structure. The diameter of the sample used in this experiment is ~50 µm. The finest split fiber could be ~1 µm thick

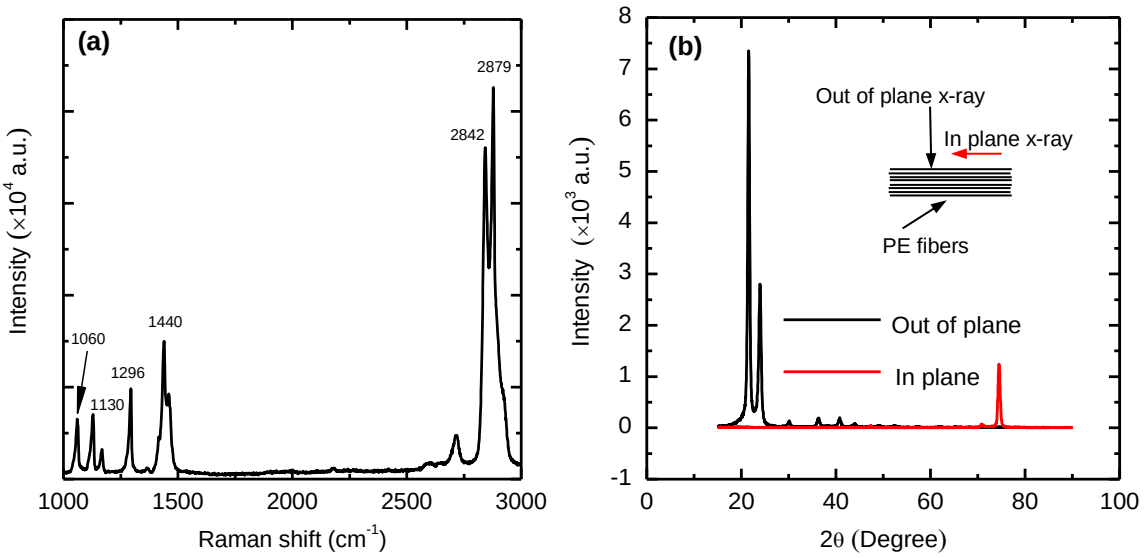

Figure 3.2 (a) Raman spectrum of our studied UHMWPE fibers. (b) x-ray diffraction patterns for the UHMWPE fibers. The inset in Fig. 3.2(b) shows the schematic experimental setup for determining the crystallite size in the (002) direction. The normal lines of the x-ray beam are out of the plane of PE fibers and in the plane of PE fibers, respectively.

The molecular structure of the fibers is characterized using a confocal Raman system (Voyage, B&W Tek, Inc. and Olympus BX51). A 532 nm Raman laser of 16 mW is focused on the fiber with a 50× objective. 20 s integration time is used to obtain a representative spectrum of the fibers as shown in Fig. 3.2(a). Sharp peaks are observed at 1060 and 1130 cm^{-1} for C-C stretching mode and peaks at 1167 and 1296 cm^{-1} for CH_2 twisting mode for *all-trans* -$(CH_2)_n$- in the crystalline structures. The existence of amorphous structures is illustrated by the amorphous peaks at 1440 and 1460 cm^{-1}. The 2842 and 2878 cm^{-1} peaks indicate CH_2 stretching modes in the fiber which are not related to the crystalline structures.[80, 81] When we place a PE fiber on a glass slide, and use another glass slide to press the fiber, we find the PE fiber can be mechanically split into finer ones. Figure 3.1(c) shows the SEM image of the sample before it is split into several finer fibers. It is observed that the cross section of the fiber is not exactly round. Figure 3.1(d) shows that a sample is split into several fine fibers mechanically, which illustrates its internal

stranded structure. The diameter of the sample used in this experiment is ~50 μm. The finest split fiber could be ~1 μm thick. This concludes that the large fiber is composed of fine fibers aligned along the axial direction.

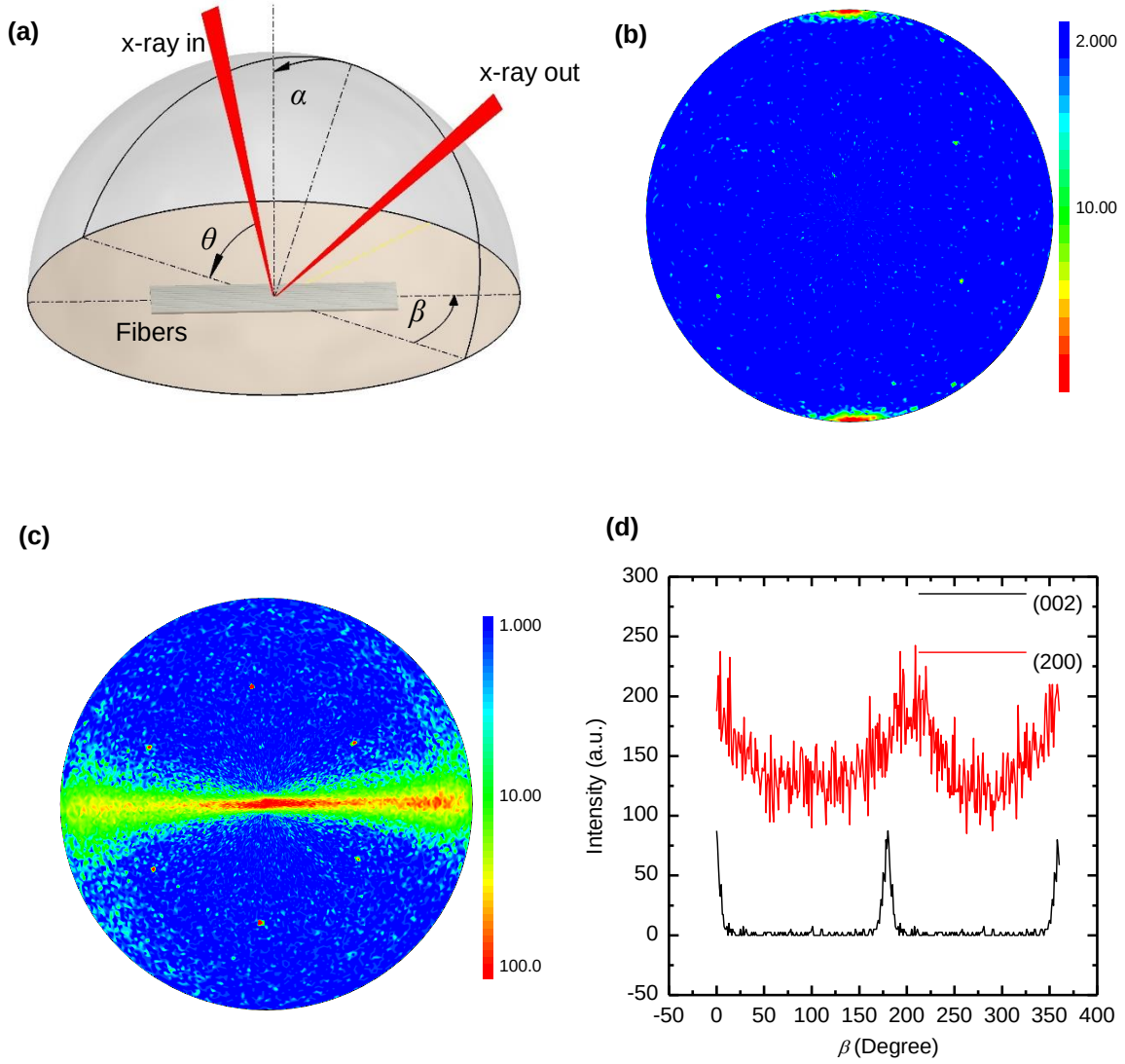

Figure 3.3 (a) Schematic of the XRD experiment. (Curtesy from Bowen Zhu) (b) Pole figure for (002) plane. (c) Pole figure for (200) plane. (d) The intensity variation along a varying β with a fixed α corresponds to a twisting motion. (002) plane: α=0°. (200) plane: α=90°.

Figure 3.2(b) gives the x-ray diffraction (XRD, Rigaku Smartlab Diffractometer) patterns for the UHMWPE fibers. The sample is highly crystalline and the crystallinity is determined to be

91.9%. The crystallite size in the (002) direction is determined to be around 19.7 nm. For the out-of-plane direction, the crystallite size is 12±1.6 nm. The inset in Fig. 3.2(b) shows the schematic experiment setup for determining the crystallite size in the (002) direction. The normal lines of the x-ray beam are perpendicular and parallel to the plane of PE fibers, respectively. Detailed crystallite orientation is analyzed based on the XRD pole figures. Figure 3.3(a) shows the schematic of the XRD experiment. The pole figures for (002) plane and (200) plane are shown in Fig. 3.3(b) and Fig. 3.3(c). Figure 3.3(d) shows the intensity variation along a varying β (β: rotation angle around sample surface normal direction) with a fixed α (α: tilt angle from sample surface normal direction) corresponding to a twisting motion, for (002) plane: α=0°; for (200) plane: α=90°. Combining (b)-(d), we could conclude that the crystallite orientation [the *c*-direction in Fig. 3.1(b)] is highly along the fiber axial direction. For the (002) plane, the orientation distribution shown in Fig. 3.3(d) has a very small angle distribution along the fiber axial direction: 8.28° for full width at half-maximum. Figure 3.3(b) and the intensity distribution in Fig. 3.3(d) show the (200) plane is more spread (all along alpha of 0° to 90°) than the (002) plane. The excellent orientation of the PE crystal in the fiber also explains why they have a high *c*-direction thermal conductivity [~25 W/(m·K) at room temperature], which is larger than that of many unprocessed PE fibers.

3.2 Thermal Conductivity of UHMWPE Fibers

3.2.1 Thermal diffusivity and thermal conductivity variation against temperature

Since there are differences among UHMWPE fibers even though they are produced at the same time, two UHMWPE fibers are used to do the experiment (S1 and S2). The samples' length and diameter are 1.32 mm and 49.08 μm for S1 and 1.17 mm and 45.17 μm for S2. After the PE

fiber is coated with15 nm-thick iridium, the to-be-measured sample is placed in a vacuum chamber of a cryogenic system (CCS-450, JANIS). The thermal diffusivity and conductivity of the two UHMWPE fibers are measured from room temperature down to 10 K by using the TET technique which is introduced in chapter 2 in details.[18, 19] Based on the sample's crystallinity of 91.9% (obtained above using XRD), the volumetric heat capacity of this sample is evaluated using the heat capacity of extrapolated crystalline and amorphous PE as a function of temperature given in Chang's work.[82] The density of crystalline PE and amorphous PE are determined to be 1000 kg/m^3 and 851.5 kg/m^3 according to previous work.[22] The volumetric heat capacity of the sample is derived from the literature according to the following equation: $(\rho c_p)_{sample}=(\rho c_p)_c\chi+(\rho c_p)_a(1-\chi)$, in which χ is crystallinity and it is determined by XRD analysis. The subscripts '*c*' and '*a*' are for crystal and amorphous structure. Figure 3.4(a) shows the determined ρc_p variation against temperature for the sample. This result will be used to subtract the effect of radiation and iridium coating. The emissivity of PE and iridium are ~0.1 and 0.3, respectively. The upper half surface of the PE fiber is coated with iridium while the lower is not, so we use 0.2 as the effective emissivity. The details of subtracting the effect of radiation and iridium on thermal diffusivity is introduced chapter 2. The real thermal diffusivity without the effect of radiation and iridium is denoted as α_{real}.

Figure 3.4(b) shows the temperature dependence of α_{real} for S1 and S2. The uncertainties of the real thermal diffusivity are presented by error bars. The temperature of the sample increases a little bit due to Joule heating, so corrections are made to represent the real temperature of the sample for the measured thermal diffusivity. The *R*-*T* relationship of the sample is first obtained, and then the average of initial and the steady-state resistances in the TET measurement are used

to calculate the characteristic temperature of sample for reporting its thermal properties. This explains why the lowest temperature is a little bit higher than 10 K in Fig. 3.4(b). During the TET test, the temperature rise is commonly less than 10 K when the voltage is increased by 3% or less. From Fig. 3.4(b), it can be seen that α_{real} decreases with increased temperature. This changing trend is almost linear. For S2, α_{real} of S2 at the lowest temperature and 294 K are determined to be 3.011×10^{-5} and 1.550×10^{-5} m^2/s, respectively. The increasing thermal diffusivity with decreased temperature points out that heat transfers faster in the fiber at lower temperatures. It is understood that the thermal diffusivity is a combined effect of both thermal conductivity and specific heat. Its variation against temperature is more related to the change of the phonon mean free path in the material. More discussions are given later for using the inverse of thermal diffusivity of crystalline regions in S1 and S2 (thermal reffusivity) to study the phonon-defect scattering effect.

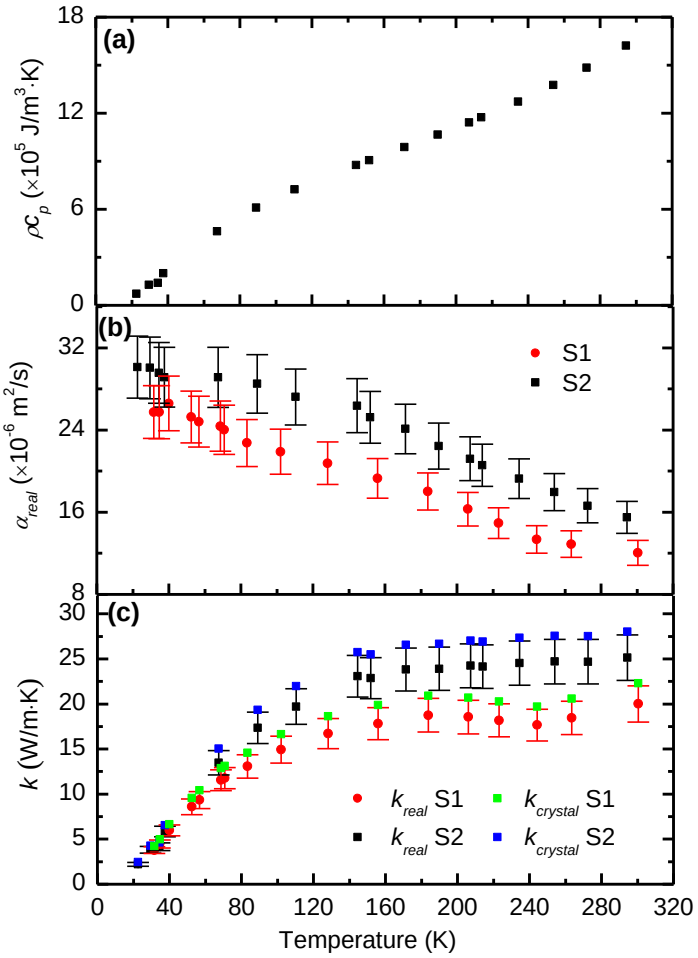

Figure 3.4 (a) The volumetric heat capacity against temperature. (b) Variation of real thermal diffusivity with temperature for S1 and S2. (c) Variation of real thermal conductivity with temperature for S1 and S2. The thermal conductivity for pure crystalline regions in S1 and S2 is also predicted by subtracting the amorphous effect and shown in the figure. The uncertainties of the measurements are presented with error bars for S1 and S2.

The real thermal conductivity (k_{real}) of the sample is obtained according to the equation: $k_{real}=\alpha_{real}(\rho c_p)_{sample}$. Figure 3.4(c) shows the variation of k_{real} against temperature for S1 and S2. k_{real} of S1 and S2 are determined to be 20 and 25.1 W/(m·K) at room temperature, respectively. They are much smaller than that of nanoscale PE fiber measured by Shen *et al*..[4] In their work, k was found to be as high as ~104 W/(m·K). This difference may arise partly from the amorphous effect. Samples in our experiment are microscale PE fibers with amorphous structure effect, while

the nanofiber used in their experiment is stretched to improve the fiber toward to an 'ideal' single crystalline fiber. Here, we give an estimate to rule out the amorphous effect and defect-induced phonon scattering effect. The semi-crystalline UHMWPE fiber used in the experiment can be considered as a two-phase system composed of crystallite and amorphous regions. The amorphous phase can be regarded as being distributed uniformly among the rich crystalline regions. In our work, the crystallinity is very high: 91.9%, so the amorphous region only takes a small volume fraction of 8.1%. Under such conditions, according to Maxwell effective medium theory, the relationship of the effective thermal conductivity of a mixture (k_e) and the thermal conductivity of the crystallite ($k_{crystal}$) is $k_e / k_{crystal} = 1 + 3(\gamma - 1)(1 - \chi) / [(\gamma + 2) - (\gamma - 1)(1 - \chi)]$. Here γ is the ratio of thermal conductivity of amorphous to thermal conductivity of crystallite, and χ is crystallinity.[28] Since the thermal conductivity of amorphous region is negligible compared with that of crystalline UHMWPE, we have $k_e / k_{crystal} = 1 - 3(1 - \chi) / (1 + \chi)$ as very precise evaluation. After taking out the amorphous effect, the thermal conductivity will be 11.5% higher. The predicted $k_{crystal}$ for S1 and S2 are also shown in Fig. 3.4(c). In Choy's work, the orientation effect is also considered when measuring the thermal conductivity of PE samples. The orientation effect is depicted by an orientation function f_c: $f_c = [3 < \cos^2 \theta > -1] / 2$, among which θ is the angle between the *c*-direction [shown in Fig. 3.1(a)] and fiber drawn direction. < > indicates the mean value over all crystallites. The thermal conductivity parallel to drawing direction ($k_{\parallel}$), thermal conductivity perpendicular to chains direction ($k_{c\perp}$) and the thermal conductivity of amorphous region (k_a) has the following relationship: $(k_{\parallel} - k_a) / (k_{\parallel} + 2k_a) = \chi \left[k_{c\perp} / k_a - 1 + 3 < \cos^2 \theta > \right] / (k_{c\perp} / k_a + 2)$.[23, 26] However, the orientation effect is not considered in this work because the chain directions in the measured samples are highly along the fiber axial direction, which is detailed in Fig. 3.3.

The predicted $k_{crystal}$ is still much smaller than the k [104 W/(m·K)] obtained by Shen *et al*..[4] In our work, we found that the sample can be easily split to finer fibers after mechanical twisting. Figure 3.1(c) and 3.1(d) show the SEM images of the sample before and after being split. This concludes that the large fiber indeed is composed of fine fibers aligned along the axial direction. We feel the grain boundary resistance, crystallite size, and alignment could contribute to the difference a lot. Since the PE crystal of our sample is highly aligned, the grain boundary resistance and crystallite size contribute more to this difference. The large thermal conductivity obtained by Shen *et al.* is for ultra-drawn nanofibers,[4] so the crystallite size (grain size) could be a big-role player.

From Fig. 3.4(c), it is found that k_{real} increases with increased temperature with a relatively faster rate at lower temperatures and kind of saturates when temperature is above 150 K. $k_{crystal}$ shows the same trend as k_{real}. Since phonon scattering dominates the thermal transport both in crystalline and amorphous regions,[83] the crystalline region largely determines the k of the fibers measured in this work. The following quantitative discussion about the samples is focused on the phonon scattering in crystalline regions. For any specific phonon with a particular wave vector κ and angular frequency ω, single relaxation time approximation is valid. Under one relaxation time approximation, it is well known that $k=Cvl$ for 1-D molecular structures. C is the volumetric heat capacity, v is the phonon velocity; and l is the mean free path. v varies little with temperature, so the trend of k is more determined by C and l jointly. Defect-induced phonon scattering and phonon-phonon scattering (Umklapp scattering) make up the phonon scattering jointly. So we could have

$$l^{-1} = l_0^{-1} + l_i^{-1} \tag{3.1}$$

according to Matthiessen's rule,[64] where l_0 and l_i are defect-induced mean free path and mean free path due to phonon-phonon scattering, respectively. This single relaxation approximation is used to qualitatively explain the observed thermal conductivity variation against temperature. l_i decreases as temperature increases while C increases with increased temperature.[82, 84] In section 3.2.2.1, detailed discussion is given about the physics on why l_i decreases as temperature increases. Due to the existence of l_0, l decreases with a lower rate compared with that of l_i as temperature increases. This causes $k_{crystal}$ to increase with increased temperature and saturate at higher temperatures. The phenomenon that $k_{crystal}$ reaches a peak value around 100 K for other PE fibers is not observed in our samples.[26] It is because, in our samples, the size of defects is comparable with the mean free path due to phonon-phonon scattering. More discussions are provided in the following sections. It is more convenient to look at the inverse of thermal diffusivity of crystalline regions (thermal reffusivity) for studying the thermal transport process.

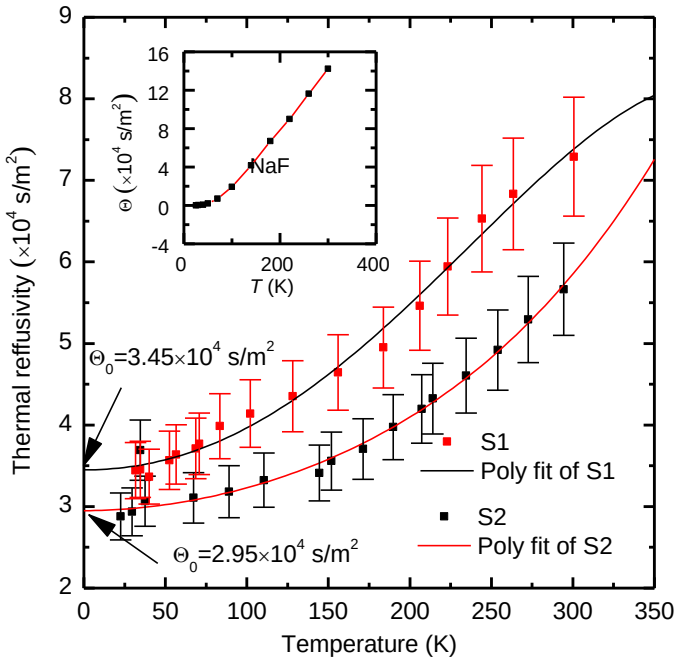

Figure 3.5 Variation of the thermal reffusivity of crystalline regions with temperature for S1 and S2. The uncertainties of the measurements are presented with error bars. The inset shows the

variation of thermal reffusivity with temperature for crystalline sodium fluoride for comparison purpose.

3.2.2 Defect effect on thermal conductivity uncovered by 0 K limit phonon diffusion

3.2.2.1 New defined parameter: thermal reffusivity

The thermal reffusivity (denoted as Θ) was first defined and used by Xu *et al.* to characterize the phonon thermal resistivity.[85] First, we plot the variation of thermal reffusivity of crystalline regions against temperature. The results are shown in Fig. 3.5. Θ plays the same role as electrical resistivity in reflecting the phonon scattering and defect scattering of energy/charge carriers. For electron charge transport, electron-phonon scattering and electron-defect scattering determine the electrical resistivity jointly: $\rho = m/ne^2\tau = \rho_L + \rho_0$ (ρ_L: the resistivity induced by thermal phonons; ρ_0: the resistivity from the static defect-phonon scattering). At the 0 K limit, a finite residual electrical resistivity ρ_0 demonstrates the existing defect in metals. If there are very rare defects, ρ_0 approaches zero at 0 K limit. Although the electrical resistivity is the inverse of electrical conductivity, the reciprocal of thermal conductivity k cannot be used similarly to define a thermal resistivity to describe the phonon scattering since ρc_p is involved in k and it also changes with temperature. Θ is defined to characterize the phonon scattering for the thermal transport behavior after ruling out the effect of ρc_p. Θ is solely determined by the phonon scattering inside the material and is expressed as the following equation in terms of phonon velocity (v) and mean free path (l): $\Theta = 3v^{-1}l^{-1}$. Therefore, Θ directly reflects the phonon scattering behavior. As will be discussed later, Θ also consists of two parts: one is induced by phonon-phonon scattering, and the other part is static phonon scattering by boundary/defects. Just like electrical resistivity, the variation of Θ versus temperature can be used to identify the residual value at the 0 K limit to evaluate the defects in the material.

Thermal reffusivity can be used to characterize different phonon scattering mechanisms. The way Θ changes with temperature ($\partial\Theta/\partial T$), and its residual value at the 0 K limit can be used to provide unprecedented details of phonon scattering. For any specific ω and κ, we already have $l^{-1} = l_0^{-1} + l_i^{-1}$. The occupancy of a phonon mode at a specific temperature T is described by the Bose-Einstein distribution,[86]

$$< n >= \frac{1}{e^{\hbar\omega/k_B T} - 1}, \tag{3.2}$$

where $\hbar$ is Planck's constant and k_B is the Boltzmann constant. $< n >$ becomes very small when temperature goes to the 0 K limit, indicating the phonon-phonon scattering is scarce and $l_i \to \infty$. The phonon-phonon scattering vanishes as temperature goes down to 0 K, and the defect-induced scattering becomes the only phonon scattering effect at the 0 K limit. For any specific ω and κ, $k=Cvl$ for the 1-D molecular structure in PE. Combing with Eq. (3.1), we get $\Theta=l^{-1}v^{-1}=v^{-1}(l_0^{-1} + l_i^{-1})=(\Theta_0+\Theta_i)$. Here, subscripts '0' and 'i' indicate for phonon-boundary/defect scattering and intrinsic scattering, namely phonon-phonon scattering. As temperature goes down to 0 K, Θ_i goes to zero, the thermal reffusivity is left with Θ_0 at 0 K. For all phonons, the accumulated effect of their residual thermal reffusivity gives the one measured in our experiment. Defect-induced phonon scattering plays a major role in limiting k. If there are no defects in the material, Θ should approach zero when temperature is zero. From Fig. 3.5, it can be seen that Θ approaches a nonzero value as temperature goes down to 0 K. The residual thermal reffusivity Θ_0 of the two samples are indicated in Fig. 3.5: 3.45×10^4 s/m^2 for S1, and 2.95×10^4 s/m^2 for S2. The trend of $\Theta\sim T$ curve is very similar to the change of electrical resistivity change with temperature for metals: if the defects in the material have substantial effect on scattering, when temperature goes to 0 K, Θ and ρ do not

approach zero; rather they have finite residual values. Many crystalline materials have been used to examine the thermal reffusivity theory. Θ of silicon, germanium, sodium chloride, and sodium fluoride are found to show different behaviors from the UHMWPE fibers. For a material with negligible defects effect, Θ_0 becomes very small (negligible) at the 0 K limit. The $\Theta \sim T$ relationship for sodium fluoride (NaF) crystal shown in the inset in Fig. 3.5 strongly proves this point: Θ becomes almost zero at the 0 K limit.[87, 88]

3.2.2.2 Defect-induced phonon scattering mean free path and volumetric heat capacity

After knowing Θ_0, we could derive the defect-induced phonon scattering mean free path (l_0) in crystalline regions for the two samples. As $T \rightarrow 0$ K, phonons with different frequencies can be reasonably considered to share the same l_0 since only a few acoustic phonons with low frequencies are excited according to Eq. (3.2).[26] Thus, we get

$$\Theta_0 = \left.\frac{\rho c_p}{k}\right|_{T\to 0} = \left.\frac{\rho c_p}{\rho c_p v l_0}\right|_{T\to 0} = \left.\frac{\sum_{M=1}^{18}\int_0^{\omega_D}\frac{\partial U_M}{\partial T}d\omega}{\sum_{M=1}^{18}\int_0^{\omega_D}\frac{\partial U_M}{\partial T}l_0 v_\omega d\omega}\right|_{T\to 0} \tag{3.3}$$

For the AIREBO model of PE crystal,[89] there are 18 phonon branches: 4 acoustic phonon branches and 14 optical phonon branches. M denotes the number of phonon branches. U_M is the thermal energy for Mth phonon branch, v_ω is the phonon velocity, and it is dependent with the frequency ω. In polymers, acoustic phonons dominate the scattering for thermal transport, so only acoustic phonons are taken into consideration when estimating phonon group velocities. For optical phonons, the phonon velocity is almost zero, so we ignore it here. The phonon velocity is $v = \partial\omega(\kappa)/\partial\kappa$ as defined. The phonon velocity variations for four acoustic phonon branches

against the normalized frequency are shown in Fig. 3.6(b). Number indices identify the two transverse (1 and 2) branches, longitudinal (3) and torsional acoustic polarizations (4). The phonon velocity will be used for evaluating the volumetric heat capacity and the defect-induced phonon mean free path, and will be discussed later. ω_D is the cutoff frequency for each phonon branch. For acoustic phonon branches, the thermal energy U_M is given:

$$U_M = \int g(\omega) n(\omega) \hbar\omega d\omega = \int_0^{\omega_D} g(\omega) \left(\frac{\hbar\omega}{e^{\hbar\omega/k_B T} - 1} \right) d\omega , \tag{3.4}$$

among which $g(\omega)$ is the density of state and $g(\omega)$ is shown in Fig. 3.6(a).[90]

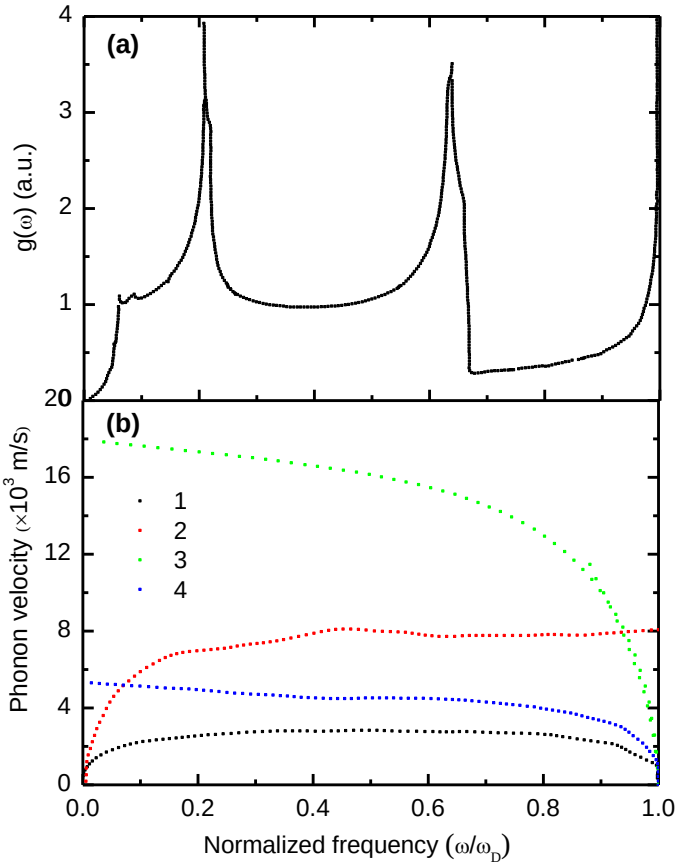

Figure 3.6 (a) Density of state for complete frequency distribution.[90] (b) Phonon velocity for four acoustic phonon branches. The legends identify the two transverse (1 and 2) branches, longitudinal (3) and torsional acoustic polarizations (4).

The volumetric heat capacity C_a for the acoustic phonons becomes

$$C_a = \sum_{M=1}^{4} \int_0^{\omega_D} g(\omega) k_B \left(\frac{\hbar\omega}{k_B T} \right)^2 \frac{e^{\hbar\omega/k_B T}}{(e^{\hbar\omega/k_B T} - 1)^2} d\omega \ . \tag{3.5}$$

For optical phonons, the thermal energy is given by the Einstein model: $U = N < n > \hbar\omega$, among which N is the number of primitive cells. Thus, we have

$$C_o = \sum_{M=1}^{14} N k_B (\frac{\hbar\omega}{k_B T})^2 \frac{e^{\hbar\omega/k_B T}}{(e^{\hbar\omega/k_B T} - 1)^2} \ . \tag{3.6}$$

The total volumetric heat capacity is the combination of two kinds of phonons. Figure 3.7(a) shows the curves of volumetric heat capacity against temperature obtained through reference and the calculation method depicted earlier. The data shown in red squares are the reference value. Data in black squares and green squares indicate the volumetric heat capacity for 14 optical phonon branches and 4 acoustic phonon branches, respectively. Data shown in blue squares are the calculated total volumetric heat capacity. The typical frequencies for the optical phonon branches are between 30 THz and 90 THz.[91] From Figure 3.7(a), it is observed that the optical phonons contributes little to the total specific heat compared with that of acoustic phonons. Since the optical phonons have almost zero velocity and is significantly smaller specific heat, the optical phonons contribute much less to the thermal transport, so the optical phonons' effect can be neglected when calculating the thermal conductivity. The calculated volumetric heat capacity is very close to the reference experimental value, which validating the theory to obtain the total volumetric heat capacity for PE crystals. The little difference is possibly induced by the fact: our frequency of phonons is based on the results of PE single molecular chain, and the chain-chain interaction is not considered. This will omit some energy contribution to the overall specific heat. Combining Eqs. (3.4), (3.5) and (3.6), Θ_0 is obtained as:

$$\Theta_0 = \left. \frac{\sum_{M=1}^{4} \int_0^{\omega_D} g(\omega) k_B (\hbar\omega / k_B T)^2 e^{\hbar\omega/k_B T} / (e^{\hbar\omega/k_B T} - 1)^2 d\omega + \sum_{M=5}^{18} k_B (\hbar\omega / k_B T)^2 e^{\hbar\omega/k_B T} / (e^{\hbar\omega/k_B T} - 1)^2}{l_0 \sum_{M=1}^{4} \int_0^{\omega_D} g(\omega) k_B (\hbar\omega / k_B T)^2 e^{\hbar\omega/k_B T} / (e^{\hbar\omega/k_B T} - 1)^2 v_\omega d\omega} \right|_{T \to 0} \quad (3.7)$$

By knowing Θ_0, $g(\omega)$ and v_ω, l_0 can be determined. Based on Eq. (3.7) and Θ_0, l_0 for S1 and S2 are determined to be 8.06 and 9.42 nm. l_0 of the two samples are both comparable, but smaller than the grain size (l_g=19.7 nm) determined by XRD. It indicates that the phonon-grain boundary/defect scattering is very strong, which makes the phonons almost lose all the original information after passing the grain interface. We can tell that the grain boundary scattering is totally diffuse, the boundary-induced phonon scattering mean free path should be shorter than the XRD-determined grain size based on the mean free path physical meaning: after traveling displacement of l_0, the phonons are left with e^{-1} times of the original energy. Here, Θ_0 is evaluated to tell the difference in grain boundary/defect-induced phonon scattering mean free path of crystalline regions for the two samples. It is better to tell the grain boundary/defect difference between S1 and S2 directly through other methods to verify the results gained in our experiment. However, due to the very small sample size (~50 μm), our current XRD system could not give a sound signal for a single fiber to distinguish the defect difference between individual fibers. Also, our Raman spectrum study could not tell the tiny defect difference between samples. To our best knowledge, there is no direct and quick technology to measure the grain boundary/defect-induced phonon scattering mean free path while the mean free path of phonons could be calculated out from experimental data.[84, 92] We believe that thermal reffusivity could serve as an alternative method to determine grain boundary/defect-induced phonon scattering mean free path that indirectly indicates the grain boundary/defect difference among samples.

3.2.2.3 Grain boundary thermal conductance

With the knowledge of l_0 and l_g, the grain boundary thermal conductance in crystalline regions is analyzed. Just as mentioned previously, the thermal resistance arises from phonon to phonon scattering and phonon scattering by the grain boundary/defect. If we assume that there is negligible defect in our sample, the thermal resistance relationship can be depicted as

$$l_g / k_{crystal} = R + l_g / k_g . \tag{3.8}$$

Here l_g is the grain size determined by XRD, k_g and $k_{crystal}$ are the intrinsic thermal conductivity of the grain and crystalline part, respectively. R is the grain boundary thermal resistance. Multiplying ρc_p on both sides of Eq. (3.8), $\Theta l_g=\Theta_i l_g+R\rho c_p$ can be determined. As temperature goes down to 0 K, Θ_i goes to zero; therefore, we can calculate the grain boundary interface thermal conductance as: $G=R^{-1}= \rho c_p / (\Theta_0 l_g)$. G could also be written as $G=\beta\rho c_p v$,[91] where β is the grain boundary scattering coefficient and $\beta=l_0/l_g$. The grain boundary scattering coefficients are determined to be 0.409 and 0.478 for S1 and S2, respectively. Chen's work gives the grain boundary scattering coefficients for phonons diffuse scattering at the grain boundary for 3-D non-equilibrium thermal transport: $\beta= 3T_{d21} / \{4[1-0.5(T_{d12}+T_{d21})]\}$, where T_{dij} is the energy transmissivity at grain boundary for phonons incident from ith layer towards the jth layer.[91] For the situation of diffuse scattering with $T_{d12}=T_{d21}=0.5$, β is 0.75 according to Chen's work. Compared with this characteristic scenario, our grain boundary scattering is a little weaker, but comparable. Then here if we assume β is weakly frequency dependent, we can give a good estimation of G using this equation $G=\beta\rho c_p v$. Figure 3.7(b) shows the temperature dependence of G in S2. The high crystallinity and good crystallite orientation helps make the grain boundary interface thermal conductance very high. At room temperature, G is 3.73 GW/(m^2·K) for S2 (R: 0.268×10^{-9} m^{2}K/W). The grain boundary

interface thermal conductance decreases with the decreased temperature, and this trend is determined by ρc_p as shown in the equation: $G=\beta\rho c_p v$. At 22 K, G becomes very small. The corresponding grain boundary interface thermal resistance is around 2.27×10^{-9} m^2K/W for S2. The order of grain boundary interface thermal resistance calculated for the UHMWPE crystal is comparable to interface thermal resistance of some other materials. Here, the interface thermal resistance of some other material is presented to show the usual order of interface thermal resistance. Wei's work shows that the interface thermal resistance in multilayer graphene structures has an order of 10^{-9} m^2W/K at room temperature.[93] Even we give a 20% variation range for β, we get the same level of interface thermal conductance. The magnitude of the G remains the same, and the true grain boundary interface thermal conductance should fall in this range well.

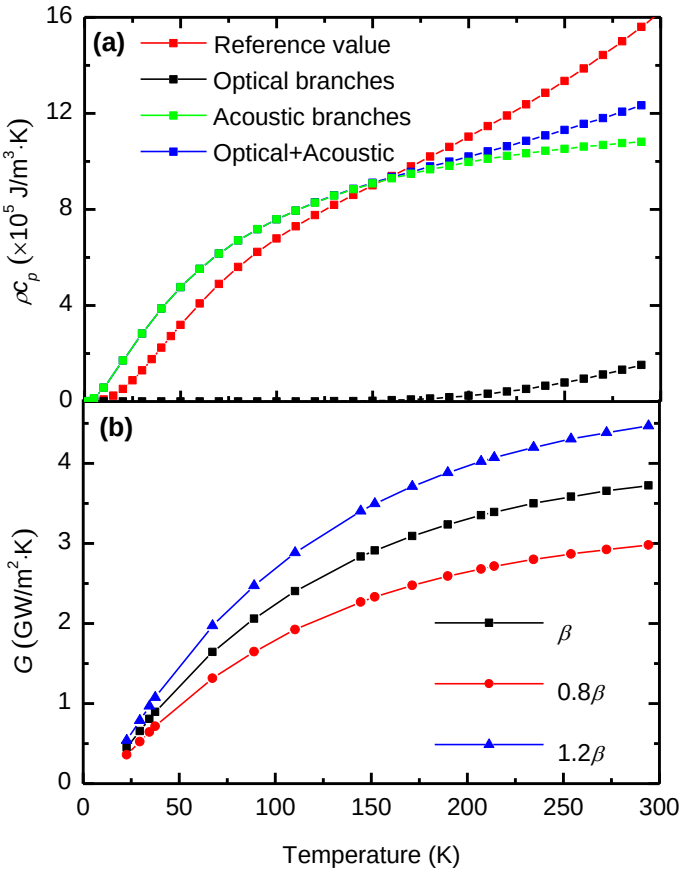

Figure 3.7 (a) Volumetric heat capacity against temperature. (b) Grain boundary interface thermal conductance varying with temperature for S2, the grain boundary interface thermal conductance range is given when β changes ±20%.

CHAPTER 4 ENERGY TRANSPORT IN CVD GRAPHENE SUPPORTED BY PMMA

In this chapter, the thermal conductivity of giant chemical vapor decomposition (CVD) graphene supported by poly(methyl methacrylate) (PMMA) is characterized using our TET technique based on a differential concept. The sample size is ~mm, far above the sample studied in the past. In section 4.1, we will introduce how to prepare the sample and the microstructure characterization. The abnormal temperature coefficient of resistance for PMMA-supported graphene is analyzed in section 4.2. The effect of radiation and effect of cross-plane heat conduction on thermal diffusivity measurement is discussed in section 4.3. Section 4.4 introduces how to obtain the intrinsic thermal conductivity of graphene. In section 4.5, we discuss about the variation of electrical and thermal conductivities among samples, followed by the structure study based on Raman spectroscopy.

4.1 Sample Preparation and Characterization

Graphene supported by PMMA tested in this experiment is obtained from Advanced Chemical Supplier company. Totally four kinds of graphene supported by PMMA are tested. They are single-layered graphene (1S), two-layered graphene (2S), three to five-layered graphene (3S) and six to eight-layered graphene (4S). The layer numbers of graphene are offered in the technical data of the samples. We also do separate measurement of the layer numbers after the samples are received. In this work, the sample index is used as this: '2S8' means the eighth tested sample of 2S. The preparation method for the supported graphene is described as follows. The graphene is grown on a copper (Cu) foil through a controlled chamber pressure CVD (CP-CVD) system. A clean Cu foil was first annealed at 1077 °C with a H_2 flow rate of 500 sccm. Then the H_2 flow rate and chamber pressure were adjusted to 70 sccm and 108 Torr, respectively. The graphene started

to grow by introducing 0.15 sccm CH_4 into the chamber.[94] After the reaction, the copper was etched off after PMMA was coated on the graphene. At last, graphene supported by PMMA was transferred onto a polymer substrate.

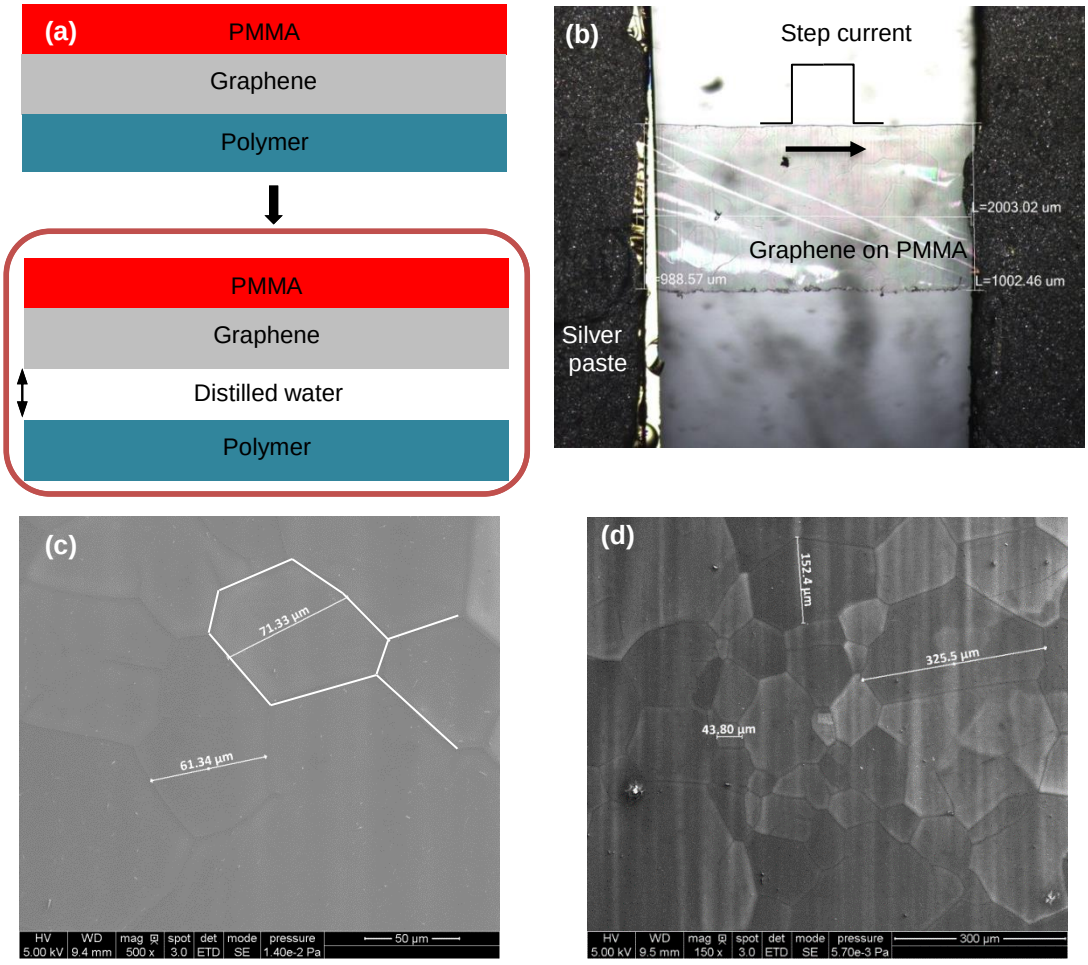

Figure 4.1 (a) Steps to obtain desired size sample from as-purchased graphene (not to scale). (b) Sample 2S3 (under microscope) suspended between two electrodes. (c) and (d) SEM images for sample 2S8. Clear grains can be seen with a characteristic size of tens to hundreds of μm. In Fig. 4.1(c), the white lines depict representative grains of graphene.

Figure 4.1(a) shows the steps to cut the sample from the originally purchased graphene into a desired sample size. First, the supported graphene is released into distilled water and then picked

up by a filter paper. The supported graphene is then cut into desired sizes with scissors. After obtaining desired experimental sample, the supported graphene is transferred to the electrode substrate, which is shown in Fig. 4.1(b). This is used for measurement of thermal diffusivity by TET technique.[18, 95] The morphology of sample 2S8 was also investigated under SEM. The SEM pictures are shown in Figs. 4.1(c, d), with clear grains visible at the level of tens to hundreds of μm. Even though the layer numbers are given in the technical data sheet of these samples, the quality and the layer number of the samples need to be examined and verified. It is necessary to know whether the graphene distributes uniformly on PMMA for the TET measurement, so the layer number of the graphene is characterized by a confocal Raman system (Voyage, B&W Tek, Inc. and Olympus BX51).

Taking sample 2S3 as an example, a 532 nm Raman laser of ~0.77 mW is focused on the graphene with a 50× objective. The integration time varies from 8 to 10 s for different spots on the graphene. Spectra of the 2S3 are shown in Fig. 4.2. It can be found that the *D* band (~1340 cm^{-1}) for 2S3 is absent from the spectrum, meaning that 2S3 has rare *D* band related defects. Peaks at around 1586 cm^{-1} (*G* band) and 2690 cm^{-1} (2*D* band) are observed. The number of the layer is obtained by evaluating I_G/I_{2D}.[96] Totally 15 random spots on 2S3 are tested. Figure 4.2 also indicates the layer number determined using the Raman spectrum for each spot. The area percentage of single-layered, two-layered and three-layered graphene are 53.3%, 40.0% and 6.7% respectively. The overall average number of layer is calculated to be 1.53 for 2S sample. Using the same method, the average layer number is determined to be 1.33 and 2.74 for 1S and 3S sample, respectively.

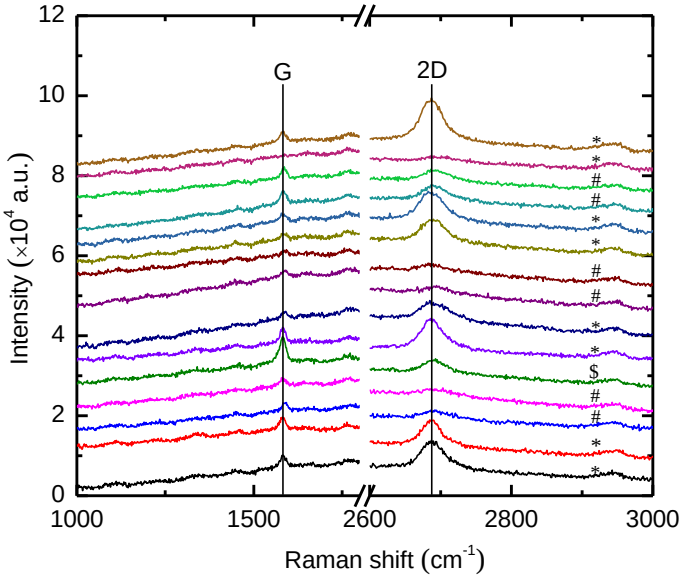

Figure 4.2 Raman spectra for sample 2S3. Clear *G* band and 2*D* band are observed. '*', '#' and '$' above each Raman spectrum indicate single-layered, two-layered and three-layered graphene, respectively.

The representative Raman spectra for 4S are shown in Fig. 4.8 and will be discussed in detail later. Three pronounced peaks at about 1346, 1589 and 2681 cm^{-1} are observed, corresponding to the *D* band, *G* band and 2*D* band, respectively. The *D* band originates from the defects and disorder structure in the sp^2 domains of graphene.[97] While no *D* band is observed in 1S, 2S and 3S, meaning they are defect-free graphene sample. Besides, some *G* bands of 4S (e.g., spectrum *a*, *b*, *c* and *d* in Fig. 4.8) show the characteristic of peaks that contains two peaks. This may arise from the stratification among multiple-layered graphene. Under this situation, it is not reasonable to determine the graphene layer number using the Raman method. Here, we determine the graphene layer number of sample 4S by measuring its optical transmittance. A laser beam (532 nm) with known incident energy is irradiating the sample surface, while an energy power meter is used to measure the transmitted energy at the same time. The transmittance is determined to be 81.48%. The refractive indexes of air, PMMA and graphene are 1, 1.49 and 2.4, respectively. The extinction coefficient of graphene is ~1.3.[98] These values are used in graphene layer number

determination. The average graphene layer number is calculated out according to the transmittance coefficient by using the transfer matrix method (TMM).[99] The layer number of sample 4S is determined to be 5.2. This value will be used when calculating the thermal conductivity of graphene. The thickness of PMMA is also needed to calculate the *k* of graphene by subtracting the effect of PMMA. The mass of PMMA (*m*) is measured by thermogravimetric analysis (TGA). With the knowledge of surface area (*A*) and density (ρ) of the PMMA, the thickness of PMMA (δ_p) is determined to be $\delta_p=m/(A\cdot\rho)$. The density of PMMA is 1180 kg/m^3 in this equation.[100] The thicknesses of PMMA and graphene layer numbers for the four samples are summarized in Table 4.1.

Table 4.1 PMMA thickness, average layer number, intercept, slope of linear fit and emissivity for 1S, 2S, 3S and 4S

Sample	1S	2S	3S	4S
PMMA thickness (nm)	790.06	632.63	825.65	630.95
Average layer number	1.33	1.53	2.74	5.20
Intercept	2.46×10^{-7}	2.46×10^{-7}	2.94×10^{-7}	2.23×10^{-7}
Slope	0.112	0.103	0.0992	0.197
Emissivity	0.128	0.0943	0.119	0.181

4.2 Abnormal Temperature Coefficient of Resistance for PMMA-supported Graphene

The TET technique is used to do thermal properties characterization. During the measurement, a step current is fed through the sample to cause Joule heating. The Joule heating leads to temperature rise in the sample, which is recorded by measuring the voltage over the sample. Generally, the resistance of graphene decreases with increased temperature.[60] However, we find

that upon heating and temperature rise, the resistance of the graphene supported by PMMA goes up instead of decreasing like many reported graphene samples (detailed in section 4.3) at RT. This section is designed to study the temperature coefficient of the resistance (TCR) of our samples before we elaborate on the thermal properties characterization.

For TCR measurement, due to the fragile nature of the sample under low temperatures, the supported graphene is placed on a glass side and silver paste is used to connect the sample with two electrodes. Then the sample is placed in a vacuum chamber of a cryogenic system (CCS-450, JANIS). A liquid nitrogen cold-trapped mechanical vacuum pump is used to make the vacuum level under 0.5 mTorr. This is intended to reduce the water content impact in the chamber at low temperatures. The resistance of the sample is detected by using a $6\frac{1}{2}$ digital multi-meter (Agilent 34401A). Since the resistance of different samples varies a lot, a normalized resistance (ratio of the resistance over that at RT) for samples with different layer numbers are presented in Fig. 4.3(a). The inset shows a close view of the normalized resistance between 100 and 220 K. When temperature is around RT, the resistance decreases a little bit when temperature decreases, giving a positive TCR. After reaching a minimum value, resistances of 1S and 2S_1 begin to rise as temperature decreases. However, the resistances of 3S and 4S increase a little bit and then drop again with decreased temperature. The maximum resistance decrease is 0.071% among the five *R~T* tests. The electrical resistance of graphene supported on flexible substrates under tensile strain has been studied by Hinnefeld *et al.*. They found that the tensile strain in the supported graphene could cause rips in the graphene, and these rips are reversible. These rips could cause the supported graphene resistance to increase significantly.[101]

Combined effects including positive thermal expansion of the PMMA (β_p), negative thermal expansion coefficient of graphene (β_g) and intrinsic resistance change of relaxed graphene against temperature (β) determine the observed R~T jointly. As shown in Fig. 4.3(b), PMMA and graphene have different thermal expansion coefficients (TEC).[102, 103] When temperature changes, PMMA and graphene will intend to have different thermal expansion. Since they are tightly held together by the Van der Waals force between them, strain and stress will be built up in graphene. This strain/stress will change the resistance of graphene accordingly. Therefore, the overall TCR of graphene could be described as the following equation: $dR/dT = -\beta + (\beta_p - \beta_g)\gamma$, among which γ is a positive constant coefficient. β_p increases with increasing temperature and remains positive when temperature is above 0 K.[102] β_g is strongly dependent on temperature but remains negative when temperature is under RT according to experiments and theoretical calculations.[103-105] When the temperature is high, the TEC of PMMA is very large, making the overall TCR positive. When the temperature is low, the TEC of PMMA and graphene becomes small compared with β, making the TCR negative as shown in Fig. 4.3(a). However, the sudden increase of TCR for 1S when temperature is reduced to around 150 K indicates that part or most of the graphene separates from PMMA. Under such scenario, the TCR is determined largely by β since the stress in graphene due to thermal expansion mismatch is released by the separation. In our experiment, since the TET measurement is conducted at RT and the temperature increase is small after Joule heating, the resistance of the sample will increase upon Joule heating and it will be shown and discussed in the next section.

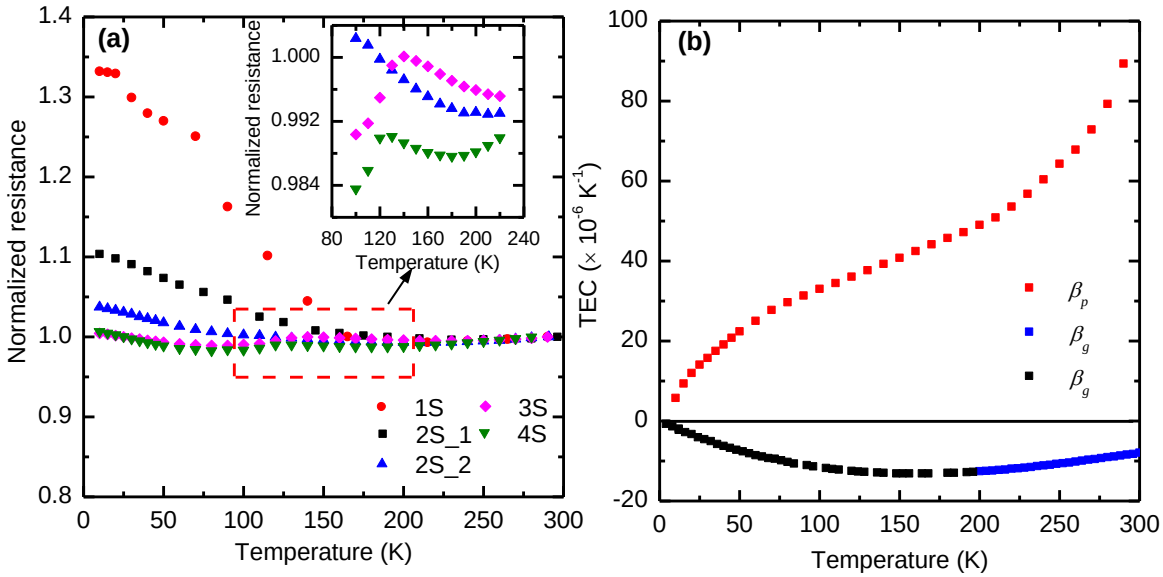

Figure 4.3 (a) Normalized resistances for 1S, 2S, 3S and 4S, respectively. The RT resistances for 1S, 2S_1, 2S_2, 3S and 4S are 0.614, 2.494, 2.587, 1.782 and 3.422 kΩ, respectively. The inset shows a close up of the normalized resistances between 100 and 220 K. (b) Thermal expansion coefficient of PMMA (from experiment) and suspended SLG.[102, 103] Data shown in blue square is obtained by the experiment fitting. The data shown in black square is the estimated value.

4.3 Thermal Characterization of Giant Graphene

4.3.1 Details of TET measurement of the thermal diffusivity

Supported graphene samples with different layers and lengths are used to do the TET test. As shown in Fig. 4.4(a), the supported graphene on PMMA is suspended between two gold-coated silicon electrodes. Silver paste is used to secure the contact between graphene and the electrodes. And then the sample is placed in an iridium coating machine (EMS 150T S) which helps keep high vacuum (below 0.6 mTorr) to do the TET test at RT. This is for eliminating heat convection effect in the measurements. During the thermal characterization, a step current provided by a current source (Keithley 6221) is fed to the sample to induce a temperature rise in the sample. The change in the temperature leads to change in resistance and thus the voltage. An oscilloscope (Tektronix DPO3052) is used to monitor and capture the voltage evolution of the graphene. Normalized

temperature change curve derived from voltage evolution is used for fitting and determining the effective thermal diffusivity (α_{eff}). As temperature rise is small, the TEC of the sample is regarded to be constant. Thus, the experimental normalized temperature change can be calculated as $\Delta T^{*}=(V-V_0)/(V_1-V_0)$, where V_0 and V_1 are the initial and final voltages over the sample. The TET technique has been proven rigorously to be a quick and effective method to m easure the thermal diffusivity of various conductive and non-conductive micro-/nanoscale samples. More details could be found in the references.[18, 73]

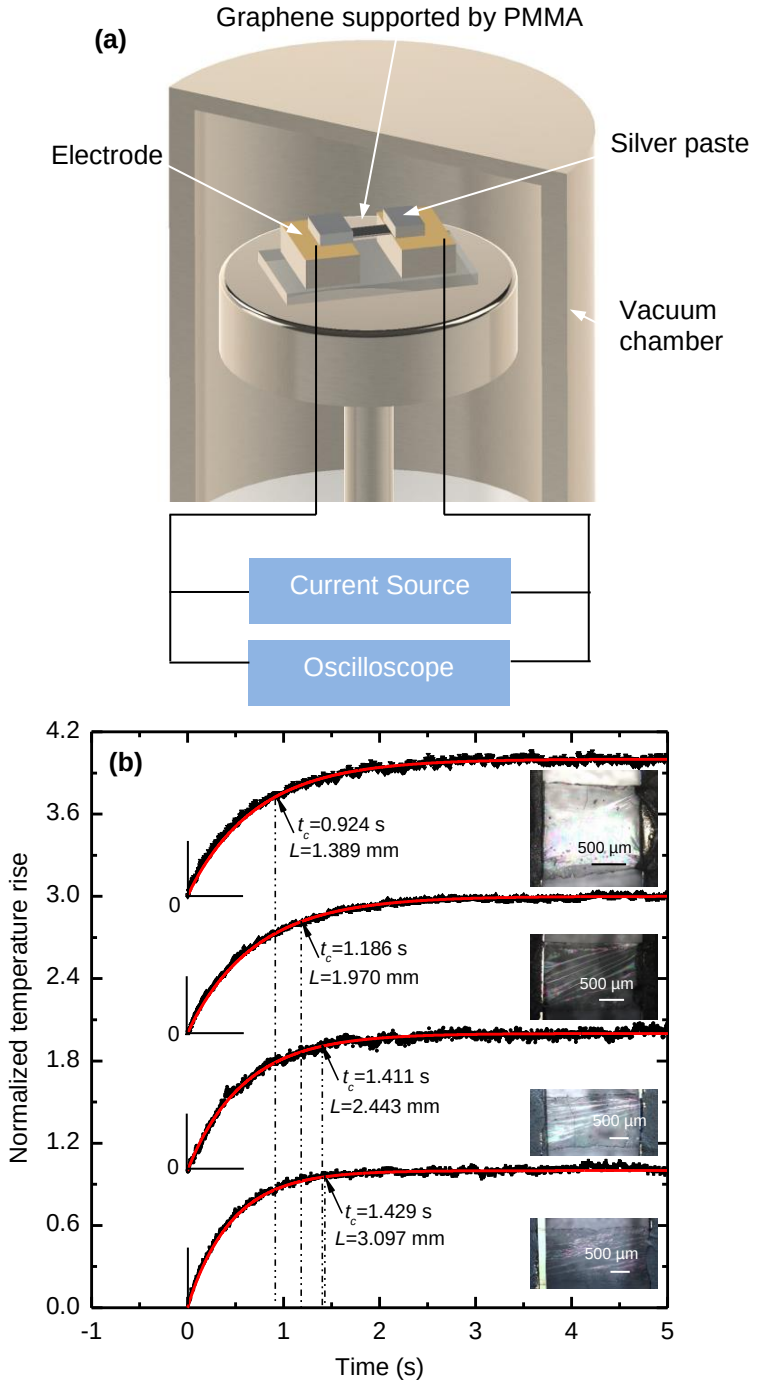

Figure 4.4 (a) Schematic setup for the TET measurement (not to scale). (b) Normalized temperature rise evolution and TET fitting results for sample 1S with different lengths. The results of different experiments are shifted in the vertical direction to enhance the view. The insets are the samples under microscope. The characteristic time (t_c) increases with increasing sample length. The black dots are the original data, and the fitting curves are shown in red.

As seen from Fig. 4.4(a), the heat conduction along the sample can be treated as one-dimensional problem. Since the gold-coated silicon is much larger than the sample dimension, the temperature of the electrodes can be assumed unchanged even though a small current goes through it. The boundary condition for this heat transport can be described as $\Delta T(x=0) = 0$, where $\Delta T = T - T_0$ (T_0: room temperature). The governing equation is

$$\frac{\partial\left(\rho c_p T\right)}{\partial t} = k\frac{\partial^2 T}{\partial^2 x} + \dot{q}\,, \tag{4.1}$$

where ρ, c_p and k are the density, specific heat and thermal conductivity of the sample, respectively. $\dot{q}$ is the electrical heating power per unit volume with the form I^2R_s/AL. A and L are the cross-sectional area and length of the sample, respectively. I and R_s are the fed-in current and the resistance of the sample, respectively. The normalized temperature rise, which is defined as $T^*(t)=[T(t)-T_0]/[T(t\rightarrow\infty)-T_0]$, is solved as

$$T^* = \frac{48}{\pi^4}\sum_{m=1}^{\infty}\frac{1-\exp[-(2m-1)^2\pi^2\alpha_{eff}t/L^2]}{(2m-1)^4}\,. \tag{4.2}$$

From Eq. (4.2), it is noted that the normalized temperature rise is only dependent on $\alpha_{eff}t/L^2$. The thermal diffusivity could be directly determined by the characteristic point of the $T^*\sim t$ curve. Details could be found in the reference.[18] The characteristic point is obtained when T^* is 0.8665 according to Eq. (4.2). The relationship between the thermal diffusivity and characteristic time (t_c) is $\alpha_{eff} = 0.2026L^2/t_c$ for quick analysis in addition to global data fitting. For global data fitting, different trial values of α_{eff} are applied in Eq. (4.2) in a MATLAB program and the T^* value is compared with the experimental results. The trial α which gives the best fitting of the experiment data is taken as the sample's α_{eff}.

4.3.2 Effect of radiation

In the TET measurement, the radiation could have strong effect on the measurement. The real thermal diffusivity (α_{real}) of the sample is obtained after taking out the radiation effect as:[18, 76]

$$\alpha_{real} = \alpha_{eff} - 8\varepsilon k_s T^3 L^2 / (\pi^2 \delta \rho c_p) . \quad (4.3)$$

In the above equation, δ, ε and k_s are the thickness of PMMA, emissivity and Stefan-Boltzmann constant, respectively. Different samples with different lengths are used to do the TET experiments, which aims at eliminating the effect of radiation.

Figure 4.4(b) shows the normalized temperature rise evolution (T^*~t) and fitting results when the experiments are conducted at RT for sample 1S. Magnificent fitting is obtained. The insets are the samples under microscope. t_c increases with increasing sample length, which is consistent with our fitting results. According to Eq. (4.3), we can see that α_{eff} and length square (L^2) have a linear relationship. The intercept at the y-axis of α_{eff}~L^2 relationship is the real thermal diffusivity of the sample. The α_{eff}~L^2 linear fitting for four kinds of graphene samples are shown in Fig. 4.5. The linear fitting intercepts and slopes for four kinds of graphene samples are summarized in Table 4.1. Also, with the knowledge of fitting slope, PMMA thickness and temperature, the emissivity of the four kinds of graphene samples can also be determined when slope is divided by $8k_sT^3/(\pi^2\delta\rho c_p)$. The determined emissivity of four kinds of graphene samples is summarized in Table 4.1. The emissivity of the first three kinds of graphene samples is consistent with each other and close to 0.1. Documents show that SLG absorbs ~2.3% fraction of incident photon energy over a wide wavelength range.[106, 107] Besides, the opacity of the graphene is found to increase linearly with increasing graphene layers. The light absorbance could be ~11.8% for the five-layered graphene according to published research.[107] It is reasonable that the emissivity of the

sample 4S is a little bit higher than other three graphene samples'. Furthermore, Dawlaty. *et al.* measured the absorbance of six-layered graphene. They found that the absorbance varies from ~0.25 to ~0.035 when the wavelength varies from 100 μm to 10 μm.[108] The discrepancy between our results and the documented values could be ascribed to different light absorbance at different wavelength. Additionally, our measured emissivity is for all directions while in other reference, the absorbance is for normal direction. The direction difference could also cause the discrepancy between our results and the documented values. Past work has shown that the emissivity of PMMA is ~2.6% at ~7 μm for a 250 μm-thick sample.[109] For our PMMA film with hundreds of nm thickness, the emissivity could be smaller since the absorption of PMMA is a volumetric effect. Therefore, the PMMA has a very small contribution to the measured emissivity.

4.3.3 Effect of cross-plane heat conduction

In our thermal characterization, the graphene layer is heated first by the electrical current, and then the thermal transfers to the PMMA. Since the graphene layer is ~nm thick, and the PMMA substrate is several hundred times thicker, a natural question is: Will the graphene and PMMA have thermal equilibrium in the cross-sectional direction? How does the heat conduction in the cross-section affect the measurement results? First, taking one supported graphene sample as an example, analysis is conducted for the effect of thermal contact resistance between graphene and PMMA. The picked sample 1S is 2 mm in length and 1.2 mm in width. When k of PMMA is 0.19 W/(m·K)[110] and the thickness of PMMA is 790 nm, the thermal resistance for PMMA conduction in the film longitudinal direction is ~1.1×10^{7} K/W. To date, no data about the thermal contact conductance between graphene and PMMA is reported. The thermal contact resistance for graphene/SiO_2 interface was measured to be 1.2×10^{-8} m^2K/W.[111] Assuming the thermal contact

resistance between graphene and PMMA is at the same level with that of graphene/SiO_2 interface, the interface thermal resistance for our samples is estimated to be 0.05 K/W. This value is much smaller than the PMMA thermal resistance in the longitudinal direction. Therefore, it is physically reasonable to conclude that the interface thermal resistance between graphene and PMMA in our sample has negligible effect on the thermal transport in the longitudinal direction.

In our experiment, the graphene is extremely thin (~nm) compared with the PMMA (632 - 830 nm). A natural question is: When graphene is heated up by the electrical current, whether it has sufficient time to conduct the heat to PMMA to reach thermal equilibrium in the cross-plane direction. For graphene, its thermal relaxation time (τ_g) can be estimated as $\tau_g \approx \delta_g R_{tc}^{''} \rho c_p$, where $R_{tc}^{''}$, ρ and c_p are thermal contact resistance, graphene density and heat capacity, respectively. For a SLG, when the graphene thickness, thermal contact resistance and volumetric heat capacity is taken as 0.335 nm, 1×10^{-8} m^2K/W and 1.5×10^6 J/(m·K), respectively, τ_g is estimated as 5 ns. For the heat conduction across the thickness direction of PMMA, its characteristic time can be estimated using this equation: $\tau_p = \delta_p^2 / \alpha_p$, where α_p is the thermal diffusivity of PMMA. When the thickness of PMMA is 790 nm, and the thermal diffusivity of PMMA is 1.25×10^{-7} m^2/s, the estimated cross-plane characteristic time for PMMA during TET measurement is 5 μs. Both characteristic times are much smaller than the characteristic time taken to reach the thermal steady state in the TET measurement, which is in the order of seconds as shown in Fig. 4.4(b). This means the temperature of graphene and PMMA at the same point have the same temperature during the transient thermal transport process.

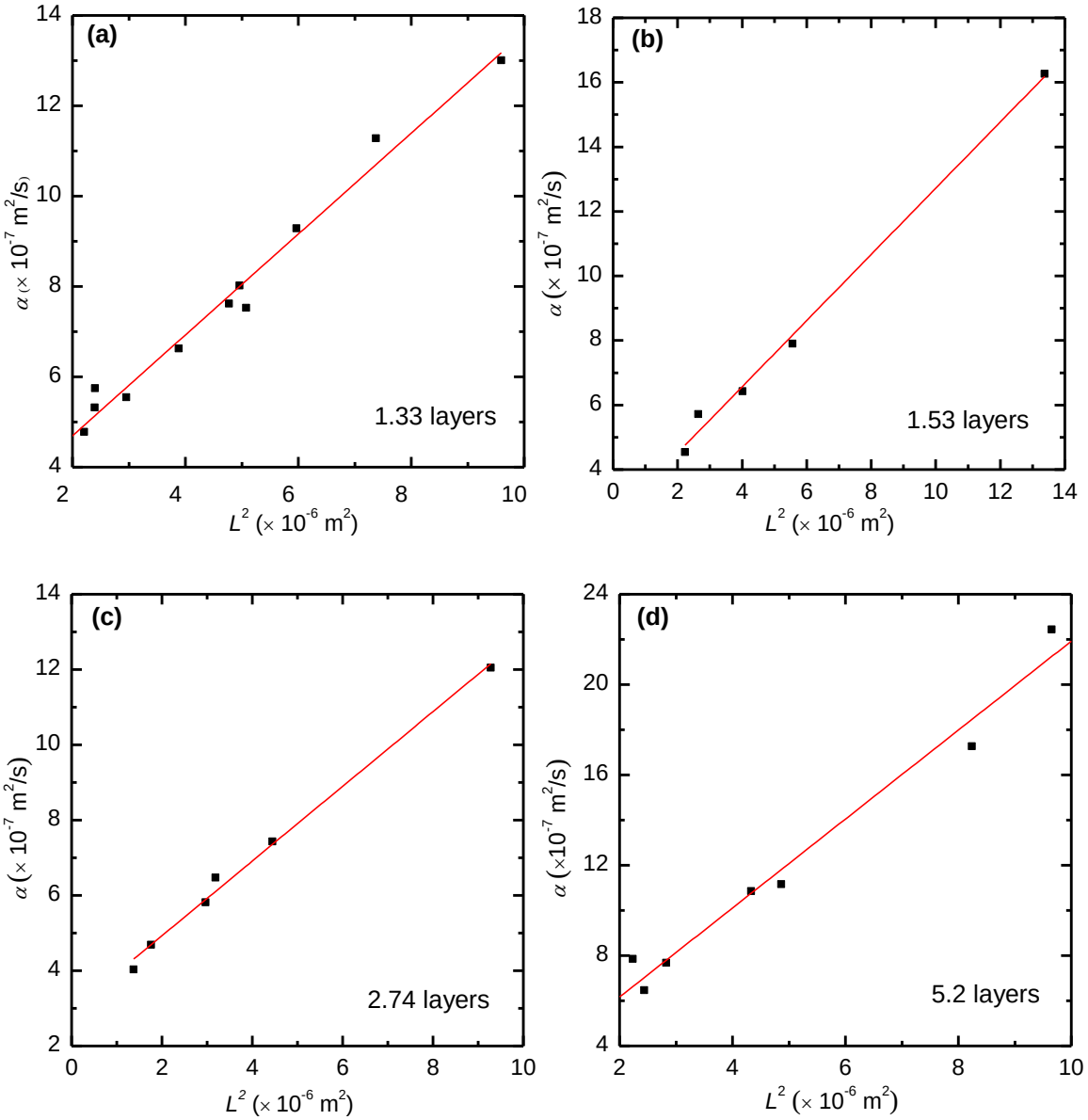

Figure 4.5 Linear fit of $\alpha_{eff} \sim L^2$ for (a) 1.33-layered graphene; (b) 1.53-layered graphene; (c) 2.74-layered graphene; and (d) 5.2-layered graphene. The black dots are the original data, and the linear fitting lines are shown in red.

Furthermore, numerical study of this transient electro-thermal transport in the supported graphene is also conducted by using ANSYS to double check the situation. The dimensions of graphene are 1.54 mm in length and 0.335 nm in thickness, and the dimensions of PMMA are 1.54 mm in length and 790 nm in thickness. The k, c_p and ρ of graphene used in the simulation are 316

W/(m·K), 709 J/(kg·K), and 2210 kg/m^3, respectively. The k, c_p and ρ of PMMA used in the simulation are 0.21 W/(m·K), 1466 J/(kg·K), and 1180 kg/m^3, respectively. The initial temperature of the sample is 298.15 K. Boundary conditions for the sample are: the emissivity for upper surface and lower surface is 0.13, temperature of two ends is considered to remain at 298.15 K during Joule heating. The heat generation in the sample is 0.0296 mW. The total simulation time is 5 s with a 0.01 s time-step interval. Figure 4.6 shows the graphene temperature evolution with time and difference between the temperature of PMMA and graphene at the middle along the axial direction. It is seen the graphene has an overall temperature rise of ~5 °C. Meanwhile the temperature difference between graphene and PMMA is in the order of 10^{-5} °C. Therefore, the temperature of graphene and PMMA could be regarded the same during Joule heating.

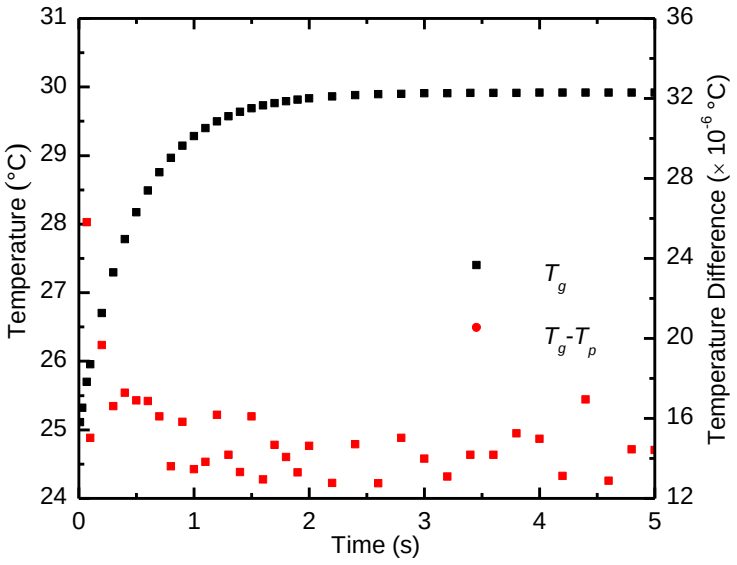

Figure 4.6 Graphene temperature evolution with time and difference between the temperature of PMMA and graphene in the middle along the longitudinal direction. The graphene has an overall temperature rise of ~5 °C. Meanwhile the temperature difference between PMMA and graphene is in the order of 10^{-5} °C.

4.4 Intrinsic Thermal Conductivity of Graphene

After knowing α, the effective thermal conductivity (k_{eff}) with the effects from PMMA and graphene can be determined as: $k_{eff} = \alpha(\rho c_p)_p$. Since the mass proportion of graphene in the composite is very small, the volumetric heat capacity of PMMA can be used for the whole sample with high accuracy. Just as discussed in the graphene layer number determination part, the graphene distribution on the PMMA is not uniform. For example, there are single-layered, two-layered and three-layered graphene on PMMA for sample 2S. In this situation, the supported graphene could be taken as a composite filled with multiple fillers. The fillers are PMMA and the corresponding on-top graphene of different layers. The thermal conductivity of the multi-filler composite could be described by the modified Nielsen model:[112]

$$\frac{k}{k_m} = \left[1 + \sum_{i=1}^{n} A_i \cdot B_i \cdot \Phi_i\right] \Big/ \left[1 - \sum_{i=1}^{n} B_i \cdot \Psi_i \cdot \Phi_i\right], \tag{4.4}$$

$$B_i = \frac{k_i / k_p - 1}{k_i / k_p + A}, \tag{4.5}$$

$$\Psi_i \cong 1 + \frac{1 - \Phi_{mi}}{\Phi_{mi}^2} \cdot \Phi_i . \tag{4.6}$$

k and k_m are the thermal conductivity of composite and base matrix. k_i represents the thermal conductivity of each filler. The subscript 'i' represents different filler. Φ_i is the volume fraction of each filler. A_i and Φ_{mi} are the shape factor and maximum packing fraction. In this sample, the graphene fillers could be regarded as uniaxial oriented fibers, and the thermal conductivity measured in this experiment is that transverse to fiber axial direction. Based on this condition, A_i and Φ_{mi} are chosen to be 0.5 and 0.82.[112] Ψ_i is a constant that taking the orientation and the packing of the filler in the matrix into account.

k_i (each filler) is written as $k_i = (n\delta k_g + \delta_p k_p)/(n\delta + \delta_p)$. δ is the thickness of single-layered graphene, and it is taken as 0.335 nm, which is the interlayer space in graphite. n is the graphene layer number of each filler. k_g is the thermal conductivity of graphene layer. Taking the sample 2S as an example, its k_{eff} is calculated to be 0.422 W/(m·K). The filler 1 (single-layered graphene on PMMA) is chosen to be the base matrix, since it has the biggest volume fraction (0.533). The volume fraction of filler 2 (two-layered graphene on PMMA) and filler 3 (three-layered graphene on PMMA) is 0.4 and 0.067, respectively. By trying different values of k_g, k of the composite is determined according to Eqs. (4.4), (4.5) and (4.6). When the k of composite is equal to the measured k_{eff} of the 2S sample, the corresponding value of k_g is taken to be the thermal conductivity of graphene. The k_g of 2S is determined to be 359 W/(m·K). Correspondingly, k_m, k_2 and k_3 are 0.40, 0.59 and 0.78 W/(m·K) for 2S, respectively. Using the same method, k_g of 1S and 3S are determined to be 365 and 273 W/(m·K). Since the graphene layer distribution of sample 4S cannot be determined by the Raman method, k_g of 4S is calculated based on the following equation: $k_{eff} = (n_a\delta k_g + \delta_p k_p)/(n_a\delta + \delta_p)$. n_a is the average graphene layer number of 4S. k_{eff} of 4S is obtained as 0.38 W/(m·K), and k_g is determined to be 33.5 W/(m·K) for sample 4S.

4.5 Results and Discussion

4.5.1 Variation of electrical and thermal conductivities among samples

Before we discuss the measured k_g, we would like to discuss the graphene quality of the four kinds of samples based on their electrical conductivity (σ) first, and then discuss how the σ and k_g vary among samples. Figure 4.7(a) shows the σ and k_g variations with the graphene thickness δ_g. Due to the possible damage during the sample preparation process, the smallest σ of four kinds of graphene is used, these can best reflect the qualities of the graphene. The σ for 1S, 2S, 3S and

4S are determined to be 3.16×10^6, 3.13×10^6, 2.05×10^6 and 5.18×10^5 $\Omega^{-1}\cdot m^{-1}$, respectively. The σ of 4S is about one fifth of that for the other three. All these measured electrical conductivities are more than one order of magnitude lower than that of suspended graphene of high quality: 7×10^7 $\Omega^{-1}\cdot m^{-1}$.[113] Also, it can be observed that k_g decreases with the increasing δ_g. The k_g of 4S is about one ninth of that for other three. The significantly reduced σ and k_g of 4S reflect the poor structure in 4S. Figure 4.7(b) shows the correlated relationship between σ and k_g. The relationship of σ~k_g is quite linear, and the σ and k_g jointly reflect that the structure of the four samples becomes poorer with the increasing graphene thickness. To further investigate the poor structure of 4S sample, the Raman spectra of 4S is shown in Fig. 4.8 and will be discussed in detail later.

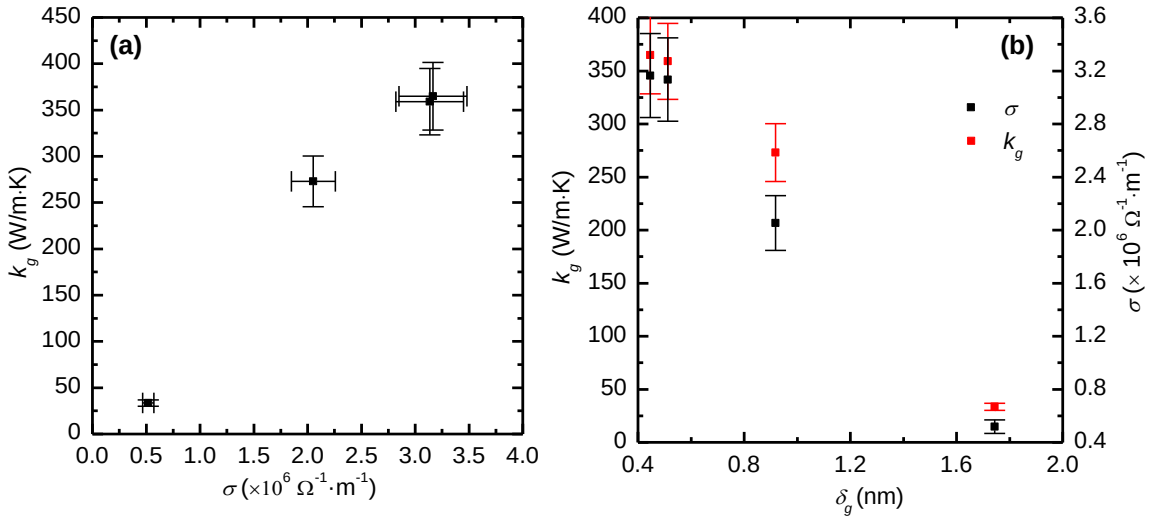

Figure 4.7 (a) Variation of the thermal and electrical conductivities of graphene with its thickness. (b) Thermal conductivity of graphene variation against its electrical conductivity.

For 1S, 2S and 3S, the k_g at RT is a factor of ~8 lower than the reported value [3000 W/(m·K)] of suspended graphene.[38] This is understandable since their electrical conductivities are more than one order of magnitude lower than that of suspended graphene. The contribution to k from ZA mode phonon scattering is significantly suppressed in supported graphene due to the

phonon leakage across the interface between graphene and PMMA.[32, 38, 46] Our k_g of supported graphene is much smaller (~40% lower) than the *k* of supported graphene obtained by Seol *et al.*[46] [~600 W/(m·K)] and the value obtained by MD simulation [609±19 W/(m·K)].[32] Two possible mechanisms lead to the *k* reduction of supported graphene by PMMA compared with that of supported by SiO_2. First, as graphene flake becomes large and contains many polycrystalline grains, the *k* of graphene will be hindered by the phonon-grain boundary scattering.[51] From Fig. 4.1(c), clear grains with a size of tens to hundreds of μm could be observed. Our sample is at the size of ~mm level and contains many graphene grains. On the other hand, the *k* of supported graphene measured based on micro-Raman spectroscopy or by the micro-fabricated device is only the *k* of very small graphene flake, at the level of 10 μm.[39, 45, 46] Second, in the thermal conductivity measurement and the simulation of above two references, the graphene is supported by SiO_2. In our experiment, the graphene is supported by PMMA. Ong *et al.* used nonequilibrium MD method to simulate the thermal transport in graphene sandwiched by SiO_2. When compared with supported graphene having weaker interface coupling strength, the supported graphene with stronger interface coupling strength has a larger thermal conductivity. It was suggested that the coupling of the graphene ZA modes to the substrate Rayleigh waves leads to enhancement in phonon velocity in supported graphene.[33] On the other hand, Chen *et al.* found that the increase of graphene-substrate coupling strength leads to shorter phonon lifetime and finally make the thermal conductivity reduce.[32] The graphene-substrate coupling strength effect on thermal conductivity of supported graphene needs more experimental data to prove. We believe that besides the graphene-PMMA coupling strength, the atomic mass and the type of atom of the substrate also play an important role in affecting the thermal transport in graphene. There are abundant carbon atoms in PMMA. Under this situation, the ZA modes of graphene will be more easily coupled with PMMA

(C atoms) than that between graphene and other substrate of heavier or lighter atoms. This ready momentum and energy coupling between C atoms in graphene and the C atoms in PMMA will result in stronger scattering of phonons in graphene, leading to more thermal conductivity reduction. In Chen's work, they predicted the thermal conductivity of SiO_2-supported FLG with 52 Å width and 300 Å length by MD simulation. It is found that the thermal conductivity of FLG increases rapidly with the layer number and finally saturates at the level of graphite.[32] In our work, the k_g of FLG linearly decreases with the increasing average layer number of the four kinds of samples. This observation is rather related with the structure of the sample, not simply the layer number. From the difference between the Raman spectra of 1S, 2S and that of 4S (in Fig. 4.8), and the electrical conductivity difference among the four kinds of samples, it is concluded that there are different defect levels in the four graphene samples.

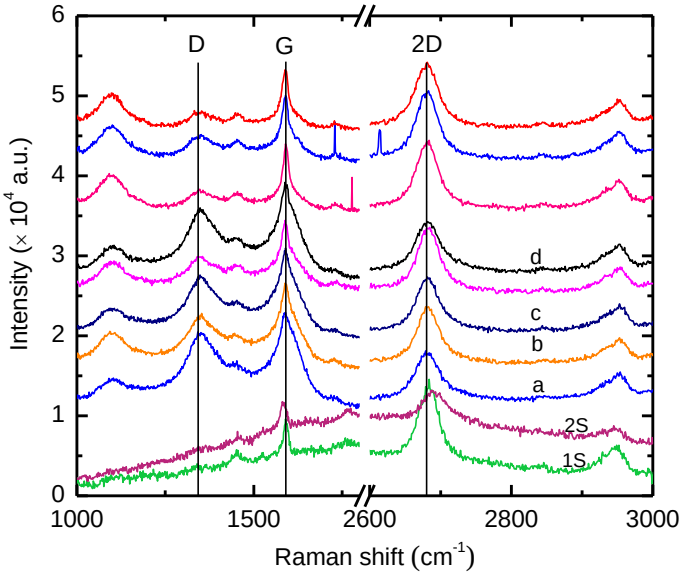

Figure 4.8 Raman spectra for sample 4S. For comparison, spectra of 1S and 2S are also plotted in the figure.

4.5.2 Structure study based on Raman spectroscopy

The k_g of 4S is significantly lower than that of other three graphene samples. Representative Raman spectra of 4S are shown in Fig. 4.8 in anticipation to explain the physics behind this significantly lower k_g. For comparison, the Raman spectra of 1S and 2S are also presented in the figure. Pronounced *D* band is observed in 4S while no *D* band is observed in both 1S and 2S. The *D* band is related with the breathing modes in the sp^2 carbon rings which are adjacent to the graphene edge.[97, 114] Also, some *G* peaks of the Raman spectra (e.g., spectrum *a*, *b*, *c* and *d*) show stratification among multiple-layered graphene of 4S. Taking spectrum *a* as an example, the *G* peak of spectrum *a* is asymmetrical, and single peak Gaussian function could not fit it well. Two peaks Gaussian function fits it well, indicating that there is stratification in the sample 4S. Besides, from the Raman spectrum *a*, *b*, *c* and *d* shown in Fig. 4.8, it is observed that *D* band and *G* band are wide and overlap. This is a typical Raman spectrum of graphene oxide (GO).[115] Based on these observations, we speculate the existence of GO in sample 4S. It is reasonable that sample 4S is a composite of graphene and GO. The in-plane thermal conductivity of free-standing reduced GO film is reported to ~61 W/(m·K).[116] To conclude, we ascribe the lower k_g of 4S to the disorder defects in sp^2 domain, the stratification among the multi-layered graphene and the existence of GO sheets.

The Raman spectrum linewidth (Γ: cm^{-1}) provides a good way to estimate the phonon lifetime. Phonon scattering dominates the thermal transport in graphene. The optical phonon lifetime (τ) has the following relationship with Γ: $\tau^{-1} = 2\pi c\Gamma$, where *c* (3×10^{10} cm/s) is the light speed.[117] Based on the Raman fitting of the four kinds of graphene samples, the linewidth of 4S (*G* peak) is ~50.2 cm^{-1}, which is much larger than the linewidth of 1S (~19.1 cm^{-1}), 2S (~18.9 cm^{-}

[1]) and 3S (~16 cm^{-1}). According to the above equation, phonon scattering in the graphene of 4S sample has a much shorter phonon lifetime. The optical phonon lifetime of 4S is estimated as 0.106 ps. This value is about one tenth of the documented value of the optical phonon lifetime in SLG (1.2 ps).[118] Although this lifetime is only for the optical phonon probed in the Raman spectrum, it is expected the acoustic phonons in 4S graphene should have the similar order of lifetime shorter than that of phonons in the other graphene samples. Thus, the k_g of 4S is correspondingly much smaller than that of other three kinds of supported graphene samples.

In graphene, phonons and electrons are the major energy carriers and phonons' contribution dominate.[119] So far, most of the experimental work measured the thermal conductivity of graphene using Raman spectroscopy. Recent numerical studies have posted a question about the non-equilibrium thermal state between phonons and electrons when the graphene is under laser irradiation during thermal conductivity measurement.[120] In the measurement based on optical heating, electrons are first heated in suspended graphene by electromagnetic excitation. Then the energy flows through electron-phonon (*e-ph*) scattering and phonon-phonon (*ph-ph*) scattering. Vallabhaneni *et al.* reported the temperature profiles of electrons, acoustic phonons and optical phonons in graphene based on Boltzmann transport equation (BTE) calculation. The laser power used in the simulation is 0.2 mW and the spot size is 0.25 μm. The average *T* of electrons is found the highest and the average *T* of optical phonons ranks second. The average *T* of acoustic phonons is the lowest. This means that during Raman spectroscopy measurement, the electrons and different mode phonons are not in thermal equilibrium. To be more specific, the ZA phonons have the largest non-equilibrium to other phonon modes. It is reported this would underestimate the thermal conductivity of graphene due to the fact that ZA phonons dominate the thermal transport.[120, 121] In

our differential technology to measure the thermal conductivity of supported graphene, this problem will not happen. Since the characteristic time of temperature rise is in the order of seconds and the sample is ~mm long, it provides enough time and space for electrons and different phonons to reach thermal equilibrium during the measurement. The TET technique offers a quick and reliable method to measure the thermal diffusivity of graphene while avoiding the thermal non-equilibrium problem among electrons, optical phonons and acoustic phonons.

CHAPTER 5 ENERGY TRANSPORT AND ANNEALING EFFECT ON STRUCTURE OF LIGNIN-BASED MICRO CARBON FIBERS

In this chapter, the systematic investigation of the structure and thermal conductivity of lignin-based carbon fibers at the microscale is reported. The structure domain size of the carbon fiber is investigated by x-ray scattering, Raman scattering in section 5.1.2. We study the temperature dependence of thermal conductivity and thermal diffusivity from room temperature down to 10 K, and the temperature dependence of thermal properties is introduced in section 5.2.1. Section 5.2.2 describes how to utilize 0 K-limit phonon scattering to obtain the structure domain size. The annealing effect on thermal transport and microscale structure is studied by the microscale Raman scanning from slightly annealed to highly annealed regions, and they are introduced in section 5.3. Finally, we report the relationship between thermal conductivity and annealed temperature.

5.1 Structural Properties of the Fiber Specimens

5.1.1 Carbon fiber manufacturing

The carbon fiber used in this study was manufactured from red oak-derived pyrolytic lignin using melt-spinning method.[122] The production method of pyrolytic lignin and manufacturing process of the lignin-based CFs are shown in Fig. 5.1(a). The detailed information could be found in reported work.[122] Briefly, red oak was pyrolyzed in a fluidized bed reactor with a staged-fractionation condenser system. Pyrolytic lignin was isolated from heavy fraction of bio-oil.[123] Because pyrolytic lignin is partly decomposed lignin which has low viscosity upon heating, it was thermally repolymerized to increase its viscosity, making it a suitable precursor for melt-spinning.[122] The as-spun fiber was then subjected to oxidative stabilization at a rate of 0.3 °C/min

up to 280 °C, and further carbonized at 3 °C/min up to 1000 °C under argon environment. The produced CF has a diameter varies from 29 to 50 µm, with majority has a diameter between 35 to 40 µm. Further characterizations of the CFs are provided in Table 5.1 and Fig. 5.1.

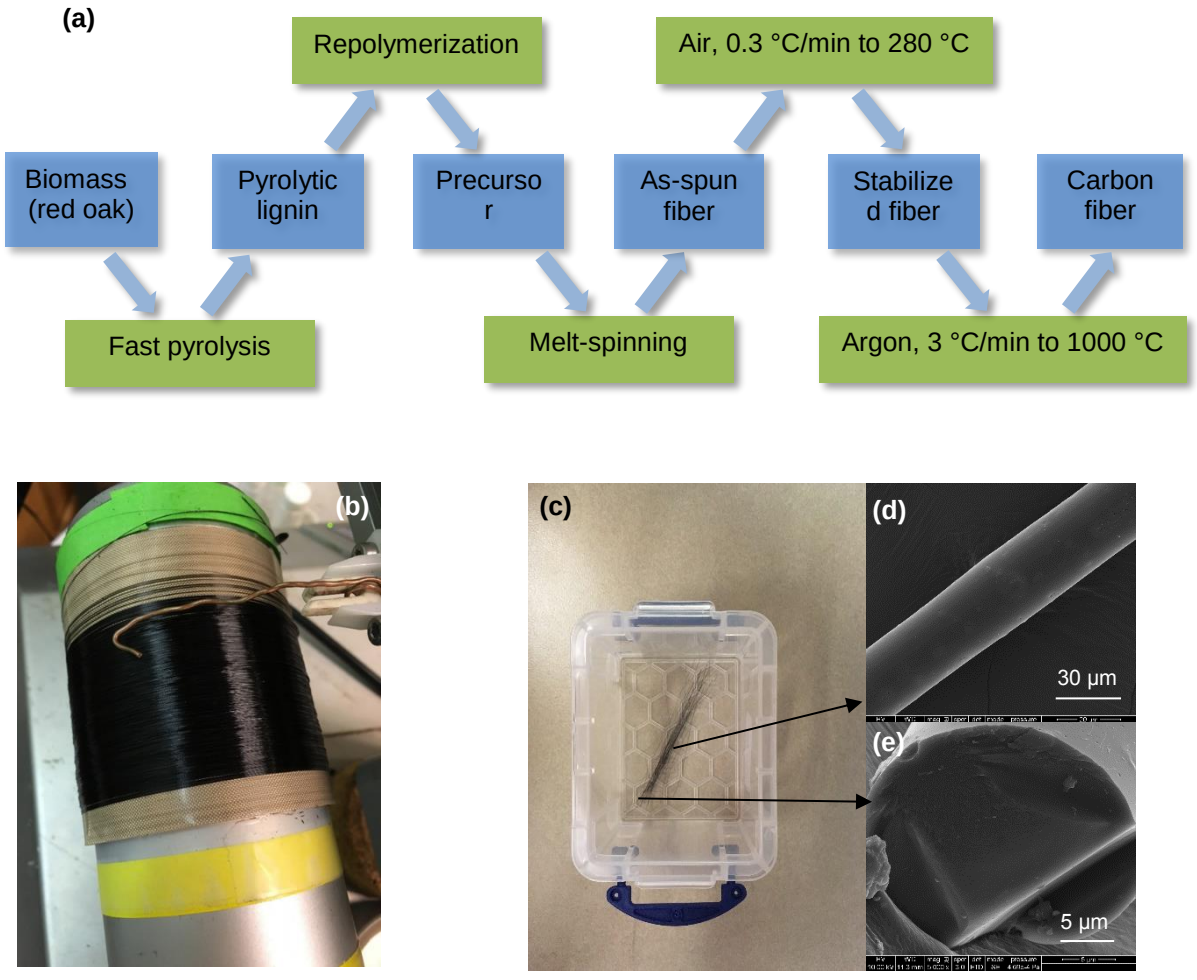

Figure 5.1 (a) Production of pyrolytic lignin and manufacturing process for the CFs. (b) As-spun fiber. (c) Carbonized CFs. (d) Scanning electron micrograph (SEM) of the surface for single CF. (e) Cross-sectional view of the CF.

Table 5.1 Properties of lignin-based carbon fiber[122]

	Lignin-based CFs
Diameter (μm)	29-50
Tensile strength (MPa)	855 ± 159
Modulus (GPa)	85 ± 37
Strain (%)	1.01 ± 0.3
Carbon content (%)	93.4
Hydrogen content (%)	0.74
Oxygen content (%)	4.55

5.1.2 Structural characterization of the lignin-based carbon fibers

Before characterizing the thermal properties, the micro-structure and elemental composition of the CFs are studied by Raman, XRD and x-ray photoelectron spectroscopy (XPS). The Raman spectrum [Fig. 5.2(a), E_{Laser}= 2.33 eV (532 nm)] of the CFs exhibits two wide and overlapping peaks at 1350 and 1580 cm^{-1}, corresponding to *D* peak and *G* peak in the CFs. A flat 2*D* region is also observed. This is a typical Raman spectrum of graphite oxide.[124] The *D* and *G* peak's full width at high maximum (FWHM) are broadened due to structure disorder.[114] It is known that *D* peak is assigned to breathing mode of A_{1g} as disorder exists. Its intensity (I_D) could be used to show the degree of disorder in the structures. *G* peak results from the motion of sp^2-hybrized carbon stretching mode and its intensity reflects the degree of carbonization.[125] The Lorenz function is employed to fit the *D* and *G* peaks, respectively, which is shown in red and blue lines in the inset of Fig. 5.2(a). Using the ratio of peak intensities I_D/I_G, the degree of disorder in the CFs is characterized. It has been proposed that I_D/I_G could be interpreted with an empirical formula: $I_D/I_G = C(\lambda)/L_a$, called the TK equation to name after Tuinstra and Koenig.[125, 126] Here, $C(\lambda) = (2.4\times10^{-10}\ nm^{-3}) \times \lambda^4$, λ is the wavelength (unit: nm) of the excitation laser, which is 532 nm in this research. L_a is cluster size. In this work, Raman spectrum of multiple points is obtained, I_D/I_G ranges from 2.18 to 2.42. The average L_a for the CFs is 23 Å.

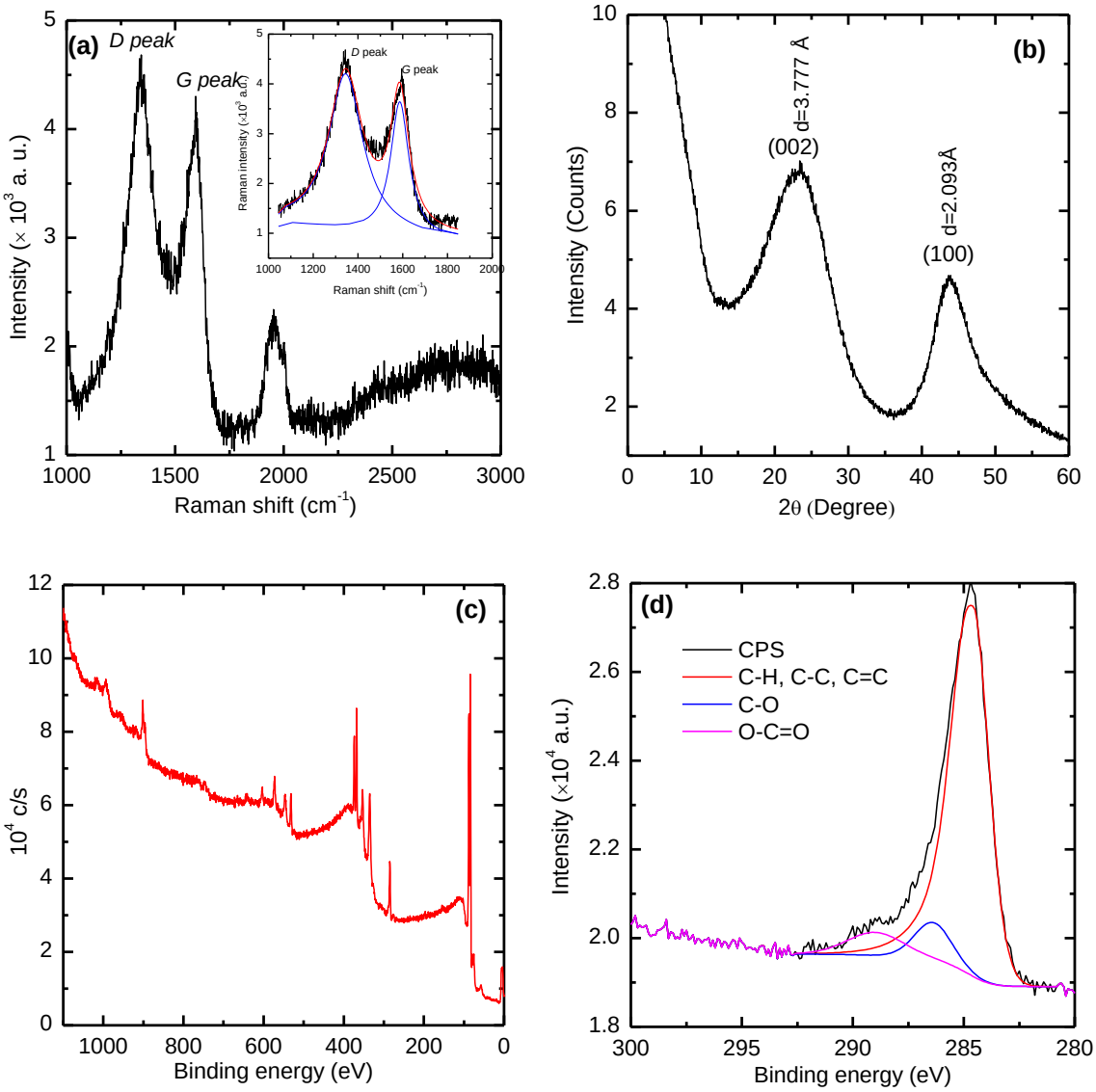

Figure 5.2 (a) Raman spectrum. Broad *D* peak at 1350 cm^{-1} and *G* peak at 1580 cm^{-1} are observed. Lorentz function is employed to fit the *D* and *G* peak, as shown in red and blue lines in the inset. (b) XRD diffractogram. (c) x-ray photoelectron spectra of CFs. (d) The XPS C1s spectrum, indicating different bonds for carbon atoms in the sample surface.

Figure 5.2(b) shows the XRD results (XRD, Siemens D500 x-ray diffractometer using a Cu x-ray tube) of the CFs. Two broad peaks are observed at 23.53° and 43.18°, corresponding to (002) peak and (100) peak. The corresponding lattice spacing is determined to be 3.777 and 2.093

Å for (002) and (100) peak, respectively. For graphite oxide, the lattice spacing between carbon layers (d_{002}) is 6.5-7.5 Å, depending on the functional group content in graphite oxide.[127] For PAN-based CFs, d_{002} varies from 3.395 to 3.53 Å.[53] We speculate that the existence of graphite oxide in our sample leads to the lattice spacing between carbon layers in our sample larger than that of PAN-based CF. The XRD also indicates the low crystallinity of the CFs. The crystallite size L_c along the normal direction of the basal plane is obtained from the (002) peak, and it is determined to be 9 Å. L_c along the basal plane is 13 Å obtained by the (100) peak. Discrepancy between the L_a determined by Raman and L_c determined by XRD is found here. This is due to different mechanisms in determining the cluster size: L_a determined by Raman reflects the phonon scattering mean free path of optical phonons, while L_c determined by XRD reflects the real crystallite size.

Chemical analysis of the CFs is conducted by XPS on a PHI55000 XPS with an Al Kα x-rays (1486.6 eV). The binding energy ranges from -5 to 1100 eV with a step size 0.5 eV, and the pass energy is 153.6 eV. Figure 5.2(c) shows the x-ray photoelectron spectra of the CFs. The elemental composition is determined as: C (93.4%), H (0.74%) and O (4.55%). The C1s XPS spectrum is shown in Fig. 5.2(d). It has three obvious peaks by deconvolution, corresponding to C-H, C-C, C=C (these three totally 84.83%) and C-O (7.87%) and O-C=O (7.29%), respectively. The existence of these functional groups also leads to a larger lattice spacing between carbon layers when compared with that of PAN-based CF.

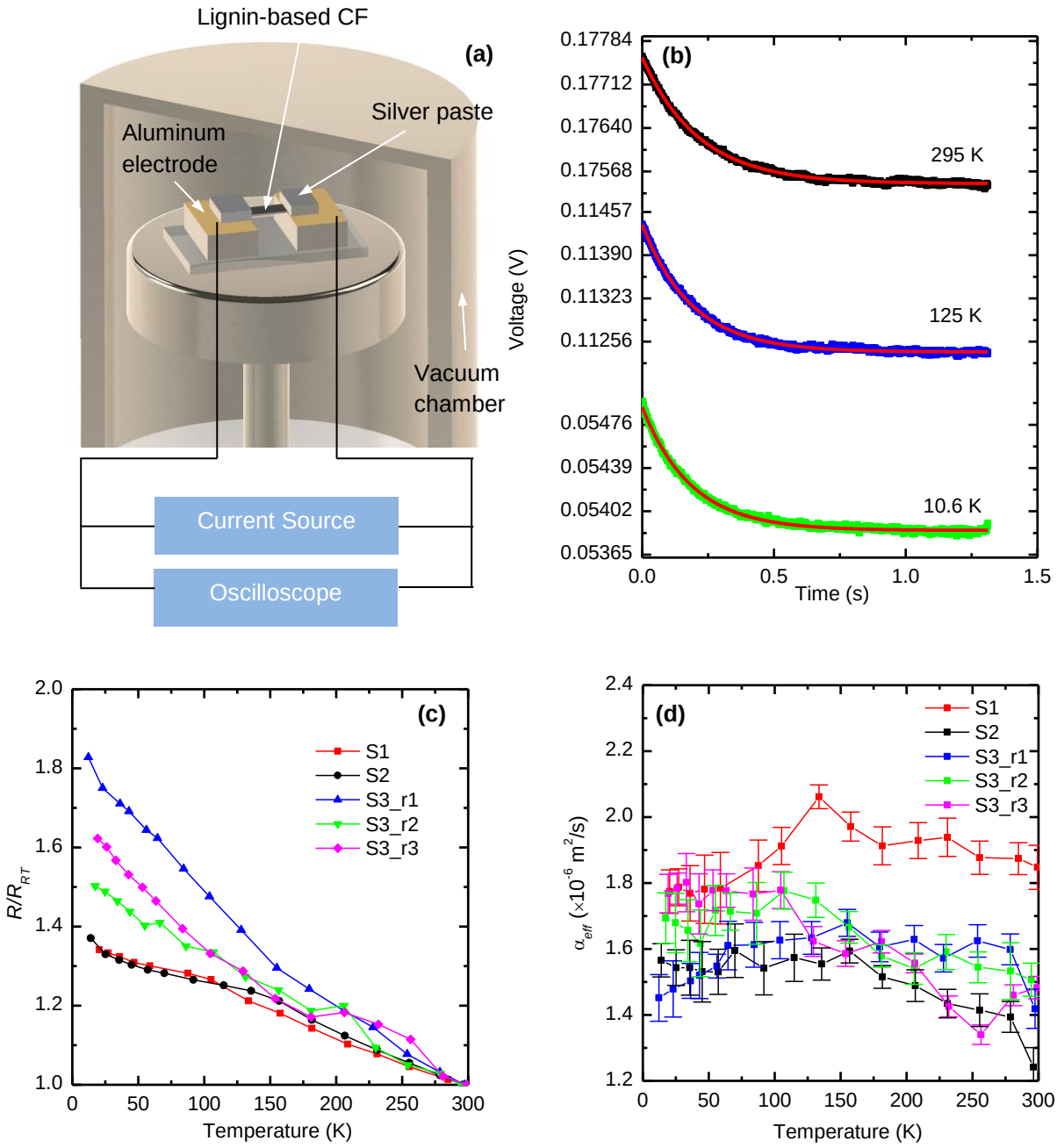

Figure 5.3 (a) Experiment setup for cryogenic TET technique. (b) The voltage profiles for S3_r1 at different temperatures: 295, 125 and 11.6 K. The symbols are the experiment data and the lines are the fitting curves. (c) Temperature dependence of the normalized electrical resistance for three samples from RT to 10 K. (d) Effective thermal diffusivity of three samples. Standard deviation of the thermal diffusvitiy is shown in the figure, too.

5.2 Results and Discussion

5.2.1 Thermal transport and properties: correlation with temperature

The thermal diffusivity of the CFs from room temperature (RT) down to 10 K is measured by the cryogenic TET technique. Figure 5.3(a) shows the systematic experiment setup. Since the TET has been introduced before, we will not introduce here in details.

In the experiment, three samples are used to do the cryogenic TET test, and they are indexed as S1, S2 and S3. S4 and S5 are annealed at high temperatures. The diameter, length and index for five lignin-based CF samples are summarized in Table 5.2. In this work, the density of the sample is obtained by measuring the weight and volume of CFs. Using an analytical balance (Radwag xA 82/220/2x), the weight of the to-be-measured CFs is 0.13 mg. The average diameter and the length of the to-be-measured sample is 40 μm and 47.27 mm, respectively. Thus, the density of the CF is determined to be 2.189 g/cm^3. The specific heat capacity of the sample at RT is set as 709 J/g·K, which is corresponding to the specific heat value of graphite.[128]

During the cryogenic TET test, TET characterizations were conducted from RT to 10 K with a step of 10-25 K. As temperature becomes lower, the temperature step is set as 10 K to have a denser data collection. For S3, the cryogenic TET characterizations were repeated for three times to study the structure stability and any thermal-cycling induced structure change. They are indexed as S3_r1, S3_r2 and S3_r3. Figure 5.3(c) shows the temperature dependence of the normalized electrical resistance for three CFs. The normalized resistance is obtained by using the electrical resistance at RT as the base. Note that all samples exhibit similar nonmetallic-like behavior throughout the entire temperature range. When temperature is changed from RT to 10 K, the

normalized electrical resistances are increased by 34%, 37% and 83% for S1, S2 and S3_r1, respectively. For S3, the resistance measured at three rounds show less repeatability. The resistance change as temperature decreases are attributed to two factors. One is the intrinsic resistance change caused by temperature change, and the other one is the strain built in the sample as temperature decreases. The CF has a negative intrinsic resistance temperature coefficient (RTC), which means that the resistance of the CFs will increases as temperature decreases. Besides, graphite and graphite oxide have different thermal expansion coefficient (TEC) as temperature is lower than 300 K. Since seldom work has been published about the TEC of graphite oxide. The TEC of graphene remains negative when temperature is lower than 300 K. As temperature decreases from 300 to 150 K, the TEC of graphene decreases from -2.5×10^{-6} to -12.5×10^{-6} K^{-1}. For graphene oxide paper, the TEC decreases from 9.1×10^{-5} to 0 K^{-1} as temperature decreases from 300 to 245 K, and then the TEC (around -4.8×10^{-5} K^{-1}) changes little as temperature decreases from 220 to 120 K.[103, 129] It is concluded that graphene oxide paper shrinks at first and then expands while graphene keeps expanding when temperature decreases from 300 to 0 K. Both graphene and graphene oxide expand as temperature decreases from 220 to 120 K. However, they expand at different level. Analogously, we speculate that there is thermal expansion difference between graphite and graphite oxide as temperature decreases from 300 to 10 K. Because of this, compressive strain is built up in the CF. This results in the resistance increase when temperature is decreased. This phenomenon has been observed and discussed in our past work.[47, 130] It has been observed that the structure change due to compressive strain could lead to permanent structure change in the material. This will result in different resistances change for S3 during the three rounds measurement, even though the whole $R\sim T$ trends are similar.

Table 5.2 Details of lignin-based CFs measured in this research

Sample type	Index	Diameter (μm)	Length (mm)
As-prepared	S1	37.97	2.07
As-prepared	S2	43.87	1.24
As-prepared	S3	40.0	1.77
As-prepared	S4	35.72	1.16
As-prepared	S5	36.10	0.905

During the TET characterization, a small DC current (I) is fed through the CF sample to induce Joule heating. With the initial resistance (R_0), steady state resistance (R_∞), and R-T relationship, we can calculate the temperature rise as $(R_\infty-R_0)/(dR/dT)$. During each TET test, the initial temperature T_0 is known, thus we got the temperature at steady state T_∞ as: $T_\infty = T_0+(R_\infty-R_0)/(dR/dT)$. The characteristic temperature of the sample is set as the average temperature of initial and steady state temperature for the reported thermal properties. This explains why the sample temperature is a little bit higher than the environmental temperature. Figure 5.3(b) shows typical TET V~t profiles of S3_r1 when experimental temperatures are 295, 125 and 10.6 K, respectively. As temperature decreases from RT down to 10.6 K, the characteristic time changes a little. This is consistent with the results that the measured effective thermal diffusivity varies little as temperature decreases. The effective thermal diffusivities for three samples are shown in Fig. 5.3(d). It is observed that effective thermal diffusivities vary a little throughout the entire temperature range. For S3_r1, the maximum and minimum effective thermal diffusivity are 1.68×10^{-6} and 1.42×10^{-6} m^2/s, respectively. The ratio of maximum to minimum value is 1.18.[59] Besides, the effective thermal diffusivities non-monotonically change with decreased temperature. For typical polymers and graphene-based materials, the thermal diffusivity increase significantly

and monotonically when temperature is decreased from RT to 10 K. For polyethylene, the ratio of maximum to minimum thermal diffusivity could be 1.8 when temperature is in the range of 10 K to RT.[59, 60] This is due to the mechanism that the phonon scattering is dominant by phonon to phonon scattering in the measured sample. However, for the CFs used in this work, the thermal diffusivity changes little, indicating that the phonon scattering in CFs is dominated by the phonon-grain boundary/defect scattering. The phonon scattering mechanism will be introduced in detail in section 5.2.2. When considering the relative error of α_{eff}, the parameter fitting error of nonlinear fitting is calculated out and it is between 0.1% and 0.3%, which is negligible. During the TET characterization, thermal diffusivity measurement of the sample under each temperature are repeated 30 to 40 rounds. The standard deviation due to measurement is calculated out by the repeated experimental results. Based on uncertainty propagation, the relative errors of effective thermal diffusivity are shown in Fig. 5.3(d).

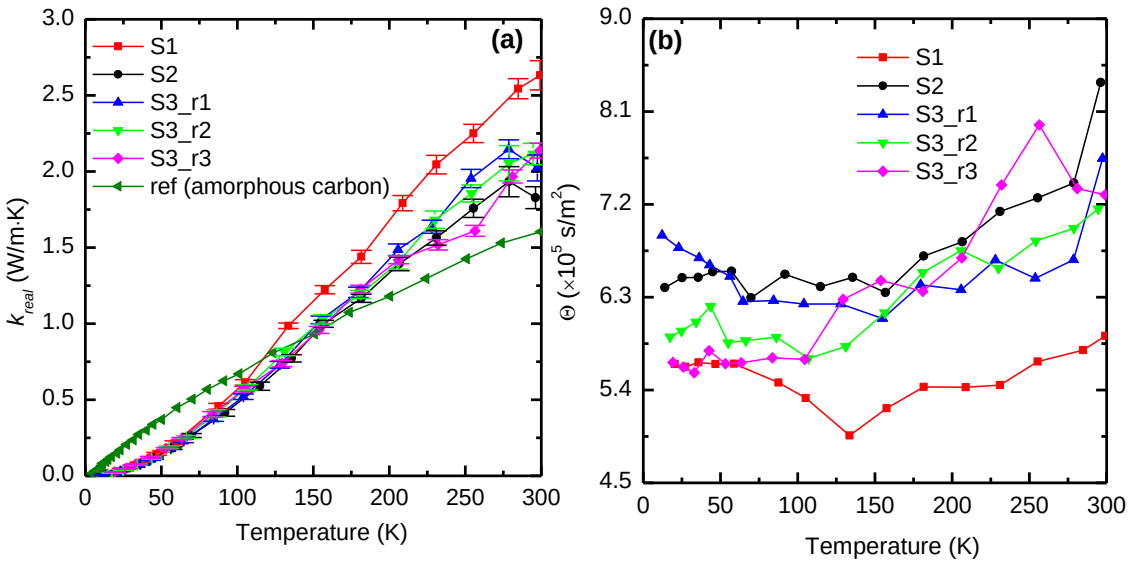

Figure 5.4 (a) Temperature dependence of thermal conductivities for three samples. Error bars are shown in the figure. (b) Temperature dependence of thermal reffusivities for three samples.

We get the specific heat capacity from RT down to 10 K from the reference[131] to subtract the thermal diffusivity due to radiation effect. Based on Eq. (2.9), the thermal diffusivity due to radiation is calculated out. Its magnitude is two orders of magnitude smaller than the effective thermal diffusivity. After knowing real thermal diffusivity, the real thermal conductivity (k_{real}) is obtained as $k_{real}=\alpha_{real}\cdot\rho c_p$. Figure 5.4(a) shows the thermal conductivity of the samples from RT down to 10 K. Error bars are given in Fig. 5.4(a), too. k is determined to be 1.83 to 2.63 W/(m·K) at RT for all the samples. Considering the differences among samples, the thermal conductivities of the as-prepared samples show good consistency with each other. For comparison, the thermal conductivity of bulk amorphous carbon is also shown in Fig. 5.4(a).[132] Our results are close to the reference values.

5.2.2 The underlying mechanism and structure-dependent phonon scattering

XRD pattern of the as-prepared CFs shows that the samples have low crystallinity. Thermal transport inside the CFs is dominated by the phonon scattering. As sample length (L) is much larger than the phonon mean free path (Λ), the thermal transport is called diffusive transport. Under this situation, various scattering mechanism jointly determine the lattice thermal conductivity. The phonons are scattered not only by other phonons but also by grain boundary and defects. Based on the single relaxation time approximation, the phonon relaxation time (τ) could be written as: $\tau^{-1} = \tau_U^{-1} + \tau_b^{-1} + \tau_d^{-1}$. Here τ_U, τ_b and τ_d are the phonon relaxation time due to phonon-phonon scattering, phonon-grain boundary scattering and phonon-defect scattering, respectively. The lattice thermal conductivity is expressed as $k = 1/3C_pv\Lambda$, among which C_p is the specific heat capacity, v is the phonon group velocity. Λ is related with the relaxation time and can be expressed

as $\Lambda = v\tau$. The thermal conductivity variation against temperature contains the information about phonon scattering and specific heat capacity. Since specific heat is temperature dependent, it is difficult to use the thermal conductivity to obtain the phonon scattering information, and then the structure of the CFs is difficult to derive.

It is known that thermal diffusivity and thermal conductivity could be expressed as: $k = \rho c_p \alpha$. To get rid of the effect of heat capacity, a good method is to study the thermal diffusivity only. In this section, the thermal reffusivity (Θ) is defined as the inverse of thermal diffusivity: $\Theta = \alpha^{-1}$. Based on the definition, Θ could be expressed as $\Theta = 3/(v\Lambda) = 3/(v^2\tau)$. Furthermore, Θ could be written as a function of phonon relaxation time due to different phonon scattering process:

$$\Theta = 3/v^2 \cdot (\tau_U^{-1} + \tau_b^{-1} + \tau_d^{-1}) = 3/v \cdot (\Lambda_U^{-1} + \Lambda_b^{-1} + \Lambda_d^{-1}) = \Theta_U + \Theta_b + \Theta_d . \quad (5.1)$$

v changes little with temperature, but it is strongly dependent with phonon mode and phonon frequency. τ_U is strongly dependent on temperature, while τ_b and τ_d are only related with the internal micro-structure. As temperature goes down to 0 K, τ_U is approaching zero due to the quick freezing-out of phonons, while τ_b and τ_d remain less changed. Thus, when temperature is 0 K, Θ_U goes to zero and the thermal reffusivity is left with Θ_b and Θ_d. It is a nonzero value at 0 K, which is caused by the grain boundaries and defects. When the phonon-boundary and phonon-grain boundary/defects scattering are dominant, Θ scales with the mean free path determined by grain boundary and defects, and it shows little temperature dependence. As the phonon-phonon scattering is dominant, Θ is strongly temperature dependent.

The thermal reffusivity variations against temperature for the three samples are shown in Fig. 5.4(b). It is observed that the thermal reffusivity shows very weak temperature dependence.

The ratio of maximum to minimum thermal reffusivity is 1.43, indicating that the phonons in the CFs are mainly scattered by grain boundaries and defects. As temperature goes down to 0 K, the estimated residual thermal reffusivity (Θ_0) are 5.67×10^5, 6.39×10^5 and 5.92×10^5 s/m^2 for S1, S2 and S3 respectively. With the knowledge of phonon velocity and residual thermal reffusivity, Λ_{eff} could be calculated as $\Lambda_{eff} = 3/(\Theta_0 v)$. The phonon velocity can be determined from the dispersion relation: $v = \partial\omega/\partial\kappa$. ω and κ are the angular frequency and wavenumber. In this work, phonon velocity is estimated as 4300 m/s, which is taken from the phonon velocity in pyrolytic graphite.[62, 133] Thus, Λ_{eff} are determined to be 12.3, 11 and 11.8 Å for the three samples, respectively.

Table 5.3 Crystallite size measured by XRD, cluster size obtained by Raman method and mean free path due to phonon-grain boundary/defect scattering

	L_c by XRD [(100) direction] (Å)	L_c by XRD [(002) direction] (Å)	L_a by Raman (Å)	Λ_{eff} (Å)
S1	13	9	23	12.3
S2				11
S3				11.8
S4				N/A.

Table 5.3 summarizes the crystallite size measured by XRD and cluster size obtained by Raman method, as well as the mean free path uncovered by phonon-boundary/defect scattering. Since a bundle of CF samples were tested in the crystallite size measurement by XRD, the obtained crystallite size is reasonable to be the crystallite size of each CF. S4 broke when the annealing temperature reached a certain value, so we could not get Λ_{eff} of S4. It is found that L_a measured by Raman, L_c obtained by XRD and Λ_{eff} show the same order of magnitude. However, the

measurement mechanisms of the three kinds of size are different. L_a obtained by Raman is measured by the optical phonon scattering, and it indicates the mean free path of optical phonons. Since the thermal transport is dominated by the scattering of acoustic phonons, Λ_{eff} is determined by acoustic phonon scattering. We can conclude that the phonon scattering mechanisms of optical phonon and acoustic phonon can be quite different. As we mentioned before, the crystallite size along the edge and basal plane are 9 and 13 Å, respectively. The crystallite sizes measured by XRD are different in different crystallite orientations. Λ_{eff} indicates the effective phonon mean free path due to grain boundaries and defects. Surprisingly, it is found that the crystallites size determined by XRD are almost equal to the phonon mean free paths caused by grain boundary/defect scattering even though there is small discrepancy between them. Former research reported that the phonon scattering mean free path due to grain boundary/defect is related with crystallite size even though no quantitative relation was established between them.[52] For those material whose crystallite size is difficult to obtain by XRD, the thermal reffusivity mechanism offers an alternative method to estimate the order of crystallite size and study the corresponding acoustic phonon mean free path due to grain boundaries and defects.

5.3 Annealing Effect on Structure and Thermal Transport

5.3.1 Micro-structure: Effect of annealing

Annealing is a high temperature treatment that alters the microstructure of materials which also helps improve the thermal properties. During the annealing process, the sample is placed in a vacuum chamber which is kept high vacuum (below 0.5 mTorr). In this work, a DC current offered by a current source (Keithley 6221) is fed through the sample to induce Joule heating, which finally leads to high temperature in the sample. Note that this is a 1-D heat conduction problem. The

temperature distribution along the fiber axial direction is not uniform. The samples denoted as S4 and S5 were used to do the annealing treatment. The original resistances of S4 and S5 are 138 and 67.9 Ω, respectively. For S4, the annealing current increases from 16 to 107 mA with a multiplication factor in the range 1.05 to 1.1. For S5, the annealing current increases from 3 to 206 mA with a multiplication factor in the range 1.05 to 1.1. The annealing time lasts from 30 to 70 s. The voltage evolution of the sample during annealing process is monitored by an oscilloscope (DPO 3052), through which the resistance during annealing process can be derived.

Figure 5.5(a) and (b) show the voltage evolutions with different annealing currents for S4 and S5. The voltage evolution consists of two states. In state 1, the voltage of the sample drops very quickly upon the annealing current feeding into it. In this state, there is no annealing process, only Joule heating process exists. It is like the TET heating and resistance change process. Since the carbon fiber shows a negative temperature-resistance coefficient, the high temperature caused by the Joule heating leads the resistance decrease very quickly. This finally results in the quick voltage drop. It is observed that state 1 becomes shorter as annealing current increases. This is consistent with the fact that the structure of the CF improves after annealing. Better structure leads to higher thermal diffusivity, so that the characteristic time becomes shorter with increased annealing current. State 2 is the annealing process. During this process, high temperature annealing helps to reduce the internal stresses and elimination of lattice vacancy in the samples, thus the resistance decreases with a very slow rate. When the annealing current is 16 mA for S4 and 6.4 mA for S5, the voltages of the samples show negligible change in state 2. This indicates that when annealing current is small, the temperature in the sample is not high enough to induce annealing process. Only as temperature increases to a certain value, the annealing process starts in the sample.

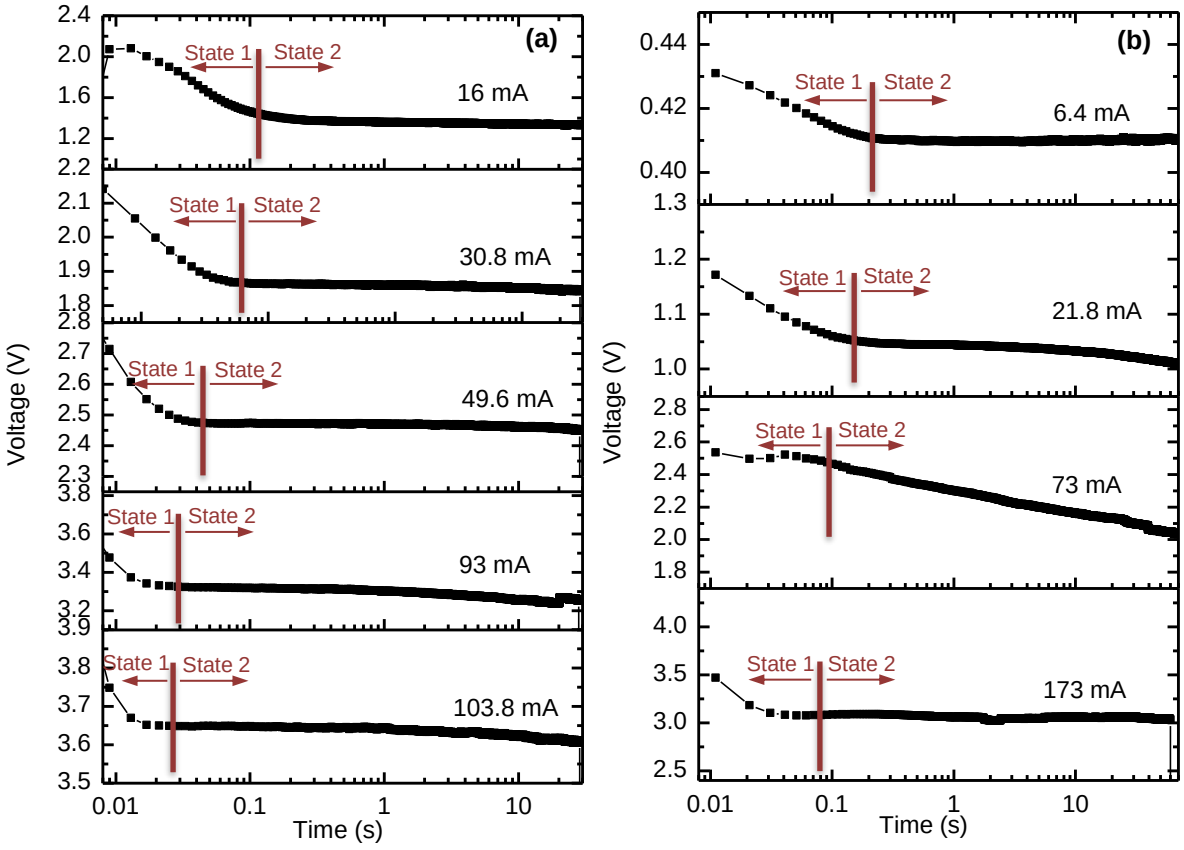

Figure 5.5 (a) and (b) Voltage evolution with different annealing current for S4 and S5, respectively.

After each annealing process, the in-situ resistance of the sample is measured by a digital multimeter. Then the in-situ thermal diffusivity of the sample is measured by the TET technique. Average resistance (R_a) during the annealing period is obtained through dividing voltage by annealing current. With current I_a fed into the sample, the annealing power is estimated as $I_a^2 R_a$. The resistance variations with increased annealing power are shown in Fig. 5.6(a). The annealing temperature has a positive correlation with the annealing power. Therefore, the annealing power could be used to indicate the annealing temperature of the sample. At first, the resistance decreases at a higher rate. As annealing power becomes larger, the resistance saturates and then it increases a little bit. Finally, the sample broke at the middle point. Since the midpoint has been suffered the

highest temperature, the breakage could be ascribed to the structural shrinkage of CF under elevated temperature. The annealing current when the sample broke is defined as maximum current (I_m). The electrical resistances of the two samples decreased by around 40% after being completely annealed. Figure 5.6(b) shows the broken sample (S4) under SEM. During the annealing process, the graphitic microstructure improves and constituents of graphite increases. This will be studied by Raman spectroscopy later. Besides, the functional groups in the CFs reduces. These two factors explain the electrical conductivity increase after annealing. This speculation in structure change is further detailed and supported in the following Raman study.

We conduct Raman spectrum study of broken S4 at different locations from the broken point. Since the temperature during annealing is not uniform, we used the measured thermal diffusivity and the derived thermal conductivity to estimate the temperature at different locations that corresponding to the measured Raman spectrum. l_d is defined as the distance of measured point to the broken point and its definition schematic is shown in Fig. 5.6(b). Figure 5.6(d) shows the temperature distribution along the fiber axial direction with the maximum current (I_m) annealing in the sample. Original point of the *x*-axis means the broken point of the sample. As l_d increases, the temperature of the sample decreases. Our Raman study gave us the information on how the structure of the annealed CF changes along the fiber axial direction under different annealing temperature.

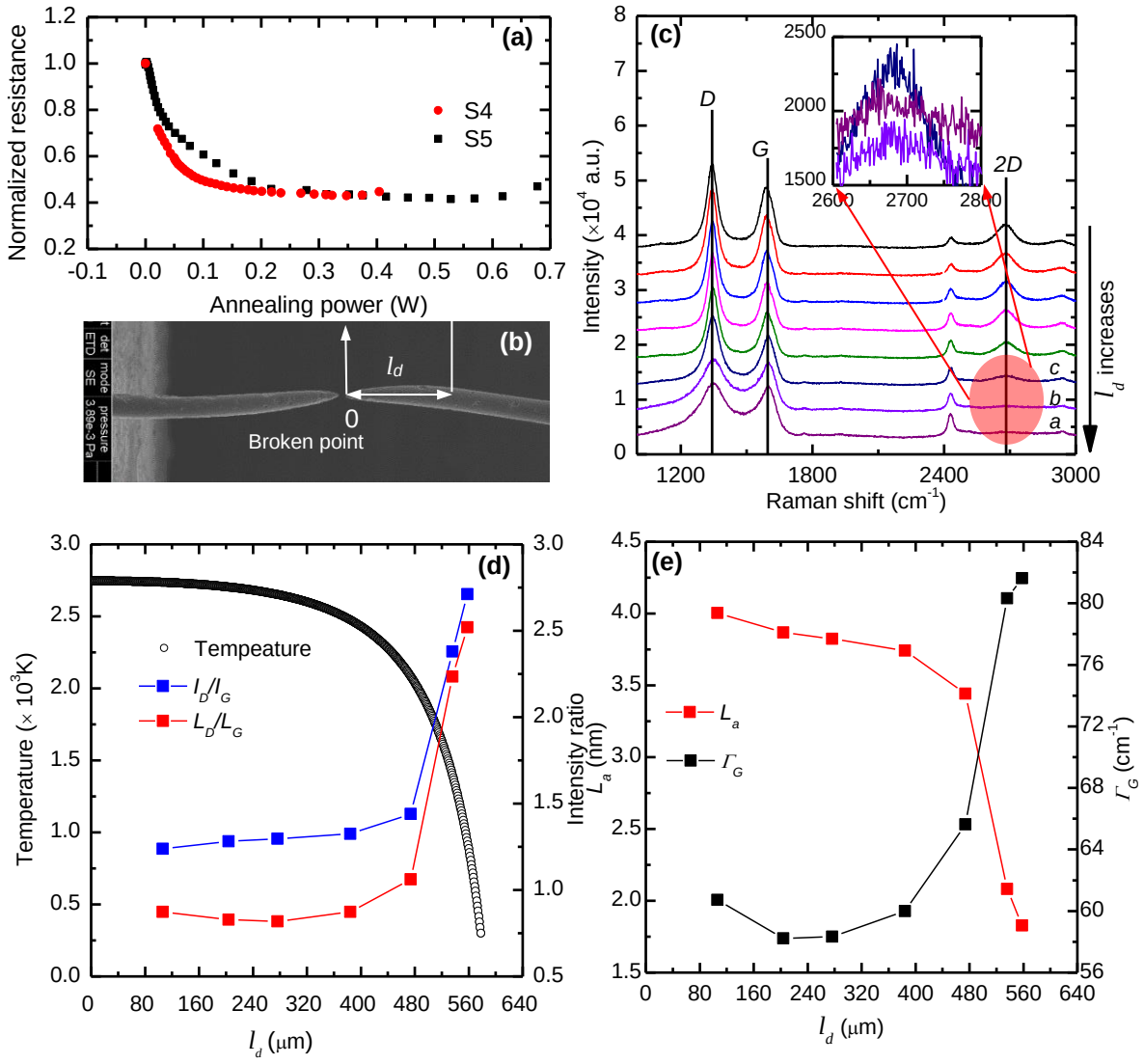

Figure 5.6 (a) Annealing power dependence of electrical resistances for S4 and S5. (b) S4 under SEM after breaking. The definition of l_d is also shown in the figure. (c) Raman spectrum at different points of S4, it is observed that the *D* and *G* peak become sharper when the tested point is closer to broken point. The inset shows a clear view of the 2*D* peak of point *a*, *b* and *c*. Point *a*, *b* and *c* is very close to the electrode end. (d) S4: Ratios of intensity and linewidth of *D* and *G* peak changes with l_d. The data shown in open circle gives the simulation result of temperature distribution before the sample broke. (e) Cluster size obtained by Raman (L_a) and linewidth of *G* peak (Γ_G) as a function of l_d.

Raman spectrum of S4 measured at 532 nm excitation is given in Fig. 5.6(c). The lens and integration time is 20× and 5 s, respectively. The inset of Fig. 5.6(c) gives a clear view of spectrum for point *a*, *b* and *c*. Point *a*, *b* and *c* are very close to the electrode end. From Fig. 5.6(c), very

wide and small 2*D* peak is found as the tested point is close to the electrode end. Also, *D* peak and *G* peak are wide and overlap for the tested point close to the electrode end. It shows a representative Raman spectrum of disordered graphite oxide.[114] As the tested points are closer to the broken point (l_d becomes smaller), a single 2*D* peak at 2677 cm^{-1} starts to show apparently. Gaussian function is used to fit the 2*D* peak. Its full width at half maximum (FWHM) is ~92 cm^{-1}, which is four-fold larger than that of 2*D* peak for graphene.[114] At the same time, both *D* peak and *G* peak become sharper as the tested point becomes closer to the broken point. Based on these, it is reasonable to state that our sample undergoes the transition from turbostratic to graphitic carbon after being highly annealed.

To further estimate the cluster size change by annealing, two-peak Lorentz function is used to fit the *D* and *G* peak to obtain the intensity and linewidth (Γ_D and Γ_G). Figure 5.6(d) shows the value of I_D/I_G and Γ_D/Γ_G changing with l_d. As l_d decreases from 558 to 106 μm (from strongly annealed region to slightly annealed region), I_D/I_G decreases from 2.71 to 1.11, indicating that annealing the CFs with higher temperatures improves the structure order. As we mentioned before, the cluster size (L_a) has the following relationship with I_D/I_G: $I_D/I_G = C(\lambda)/L_a$. Thus, we obtain the cluster size and its variations with l_d, as shown in Fig. 5.6(e). It is observed that L_a decreases from 4 to 1.83 nm as l_d increases from 60.7 to 557.9 μm. Figure 5.6(e) also shows the Raman spectrum linewidth of *G* peak (Γ_G) changing with l_d. The optical phonon lifetime (τ) has the following relationship with Γ_G: $\tau^{-1} = 2c\pi\Gamma_G$. c (=3×10^{10} cm/s) is the speed of light.[134] Γ_G increases with increased l_d, indicating that optical phonon lifetime decreases with increased l_d. This strongly supports the conclusion that annealing significantly improves the structure order, which can be reflected by a longer optical phonon lifetime. The annealing effect on the structure of the sample

is strongly dependent on the annealing temperature. The middle part of the sample has higher annealing temperature, leading to better structure of the middle part. The temperature of the sample close to the electrode is much smaller, resulting in no annealing process.

5.3.2 Thermal properties: Effect of annealing temperature

In our annealing process, after each annealing, the thermal diffusivity of the sample is measured using the TET technique. But this scenario is different from the measurement of as-synthesized sample. For the as-synthesized sample, the thermal conductivity and diffusivity are uniform along the sample. But for the annealed sample, due to the nonuniform temperature distribution along the fiber axial direction during annealing, the whole sample is not annealed at the same level. Therefore, the thermal conductivity along the fiber axial direction will vary. In our TET data processing, this non-uniform *k* direction is considered based on numerical modeling. In the 1-D numerical thermal transport simulation, the thermal conductivity along the fiber axial direction is assumed to be linearly distributed. Since the temperatures at the two electrodes change very little during the annealing process, the *k* at two ends is set as the thermal conductivity of as-prepared samples. The middle point of the sample has the largest annealing temperature, leading to a maximum *k* at the middle point. We used 1-D numerical thermal transport simulation based in the finite difference method to simulate the temperature evolution for TET data processing. During the simulation process, the emissivity is set as 0.85, which is the same value used in calculating out the effect of radiation on thermal diffusivity before. *k* of as-prepared samples is taken to be 1.75 W/(m·K). By varying the *k* at middle point, we get multiple normalized temperature evolutions changing with time. The one best fitting the experimental result is taken as the property of the sample. This middle point thermal conductivity is termed as k_m.

To evaluate the temperature of the middle point (T_m) and average temperature (T_a) during annealing, the above obtained k_m is used to model the steady-state heating conduction in S4 during annealing. In the steady-state heating model, the emissivity of CF is set as 0.85 at RT. As annealing power increases, the temperature of the sample increases as well. The emissivity of CF deviates from 0.85 when temperature is high. We found that when emissivity changes with ±10%, the obtained T_m shows a 2% variation. Thus, we set the emissivity of CF as 0.85 in the temperature range 300 to 2800 K. The inset of Fig. 5.7(a) shows the measured real thermal diffusivity (α_{real}) variation with average temperature during the annealing process. α_{real} increases by 80% when average temperature increases from 700 to 2300 K. Figure 5.7(a) shows how T_m changes with annealing current square in the sample. As annealing current increases, the temperature at the middle point reaches to a certain value, under which the sample broke. This temperature is termed as T_c. T_c is determined to be ~2770 K. It is reported that the melting point of graphite is 4489 °C under 10.3 MPa.[135] T_c of CFs is much smaller than the melting point of graphite, indicating the intrinsic defective graphitic structure in our CFs. The inset of Fig. 5.7(b) shows the k_m changing with annealing temperature at the middle point. Overall, k_m increases monotonically with the annealing temperature. As temperature in the range of 800 to 2000 K, k_m increases at a slower rate. It increases from 7.2 to 11.2 W/(m·K), by 55.6%. As annealing temperature is above 2000 K, k_m increases faster. It is increased by 110%, from 11.2 to 23.5 W/(m·K). It is concluded that when annealing temperature becomes higher, the fiber is more annealed, leading to a much more improved microstructure in the CFs. This has been confirmed by Raman study before. Figure 5.7(b) shows the inverse of k_m as a function of annealing temperature. A linear fitting between the inverse of k_m and temperature is obtained and shown in the figure. The correlation between $1/k_m$ and T is

obtained as $1/k_m = 0.1997\text{-}5.669\times10^{-5}T$. This correlation offers us a quick method to predict the annealed thermal conductivity with known annealing temperatures.

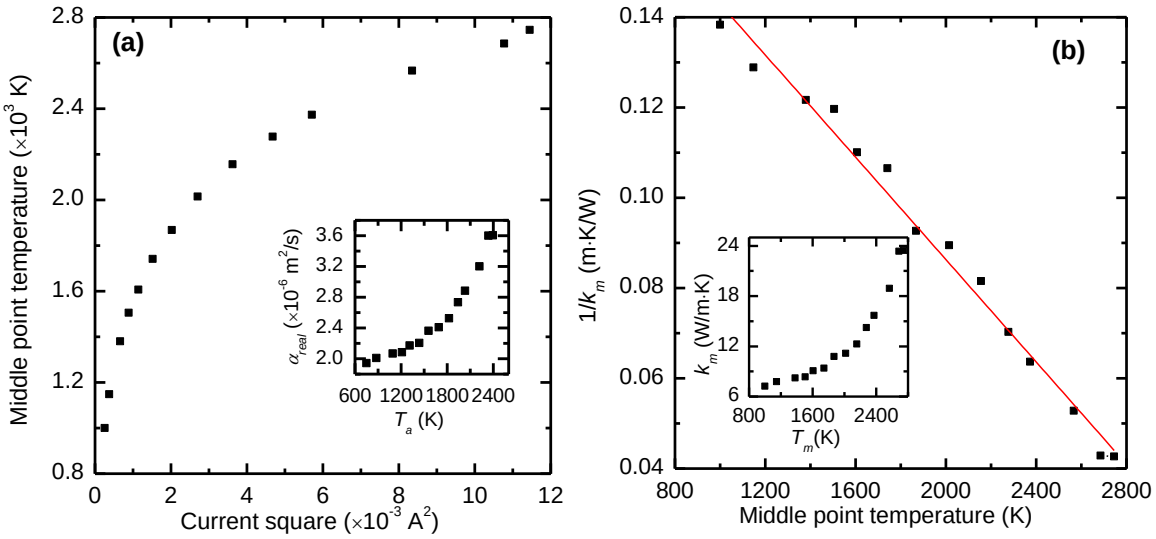

Figure 5.7 (a) Temperature variations of middle point against annealing current squares during annealing process. The inset shows the thermal diffusivity of the sample changing with average temperature during the annealing process. (b) Inverse of thermal conductivity of middle point ($1/k_m$) changes with temperature of middle point. The temperature dependence of thermal conductivity at middle point is shown in the inset, too.

CHAPTER 6 CONCLUSION AND FUTURE WORK

6.1 Conclusion

6.1.1 Conclusion on microscale thermal characterization using Johnson noise

A novel technique was developed to directly characterize the thermal conductivity of one-dimensional microscale materials based on Johnson noise. The thermal conductivity of glass fiber was determined to be 1.20 W/(m·K), which agreed well with the result using a standard technique in our laboratory. The JET technique does not require calibration and impedance matching in terms of Johnson noise measurement since low-frequency Johnson noise was used in our technique. In many other techniques for thermal conductivity measurement, a *R-T* relation must be used for temperature measurement. Calibration is usually needed to establish the *R-T* relation. Since some materials' electrical resistance can be changed permanently during the test, if the resistance and the temperature are obtained at different times, the accuracy of the experiment is sacrificed. Besides, some micro-/nanoscale materials are fragile and easily broken with high temperature change, which leads to the failure of *R-T* calibration. In the JET technique, the resistance and Johnson noise of the sample are obtained simultaneously; therefore, the accuracy of the experiment can be significantly improved. Besides, since the TET technique could measure the thermal diffusivity successfully and the JET technique could measure the thermal conductivity directly, these two techniques can be combined to determine the volumetric specific heat of a material with high accuracy.

6.1.2 Conclusion on energy transport in microscale polyethylene crystalline fibers and phonon scattering study

In this work, we characterized the thermal diffusivity and thermal conductivity of

microscale UHMWPE fibers from room temperature down to 22 K. At room temperature, the thermal diffusivity and thermal conductivity of the samples were measured at around 1.376×10^{-5} m^2/s and 25 W/(m·K). The high crystallinity and excellent crystallite orientation (studied with XRD) make contributions to the high thermal conductivity. A newly defined parameter "thermal reffusivity" was introduced to explain the effect of defects in polymers. Through thermal reffusivity, the mean free path due to grain boundary/defect-induced phonon scattering is determined. The phonon mean free paths determined by boundary/defect in crystalline regions of S1 and S2 were calculated as 8.06 and 9.42 nm, respectively. These values were relatively smaller than the XRD-determined crystallite size of (002) plane in our samples: 19.7 nm. The grain boundary thermal conductance can be evaluated with a sound accuracy using this equation: $G\approx\beta\rho c_p v$. At room temperature, the grain boundary thermal conductance was 3.73 GW/(m^2·K) for pure crystalline S2. The order of the interface thermal conductance increased from ~0.2 to ~4 GW/(m^2·K) when temperature increased from 22 K to room temperature. We also investigated the volumetric heat capacity of PE fibers, which was very close to the experimental value from reference.

6.1.3 Conclusion on energy transport in CVD graphene supported on PMMA

In this work, we first reported the *R*-*T* relationship for different-layered supported graphene. Our samples' d*R*/d*T* reduced from a positive value at RT to a negative value at low temperatures (~10 K), while free-standing graphene has a negative value across the whole temperature range. This is due to the different thermal expansion coefficients of graphene and PMMA and the strain/stress built in graphene under temperature variation. Using our TET technique based on a differential treatment, the thermal conductivity of 1.33-layered, l.53-layered, 2.74-layered and 5.2-

layered supported graphene was measured to be 365, 359, 273 and 33.5 W/(m·K), respectively. These values were a factor of ~8 lower than the reported thermal conductivity of suspended graphene [~3000 W/(m·K)]. This thermal conductivity reduction is attributed to suppressed ZA phonon contribution by the substrate, and the abundant C atoms in PMMA which are more easily coupled with graphene atoms than other substrates of heavier or lighter atoms. Our Raman spectroscopy study showed the existence of graphene oxide sheets, disorder in sp^2 domain and stratification in the 5.2-layered supported graphene. All these factors combined and led to more thermal conductivity reduction in the 5.2-layered supported graphene. The electrical conductivity of sample 4S was determined one-fifth of those of other three kinds graphene. This, from another aspect, proved the poorer graphene quality of sample 4S. Our graphene size reached a level of ~mm, much larger than the sizes of samples studied in the past. This giant graphene measurement significantly suppressed the thermal contact resistance problems and edge phonon scattering encountered in graphene thermal conductivity measurement at the μm scale. Since the characteristic time of temperature rise in our measurement is in the order of seconds and the sample is ~mm long, electrons and different mode phonons could have sufficient time and space to reach thermal equilibrium during the measurement. The TET technique could measure the thermal conductivity of graphene while avoiding the thermal non-equilibrium problem among electrons, optical phonons and acoustic phonons.

6.1.4 Conclusion on thermal transport and microstructure of lignin-based carbon fiber

In this work, the micro-structure and thermophysical properties of lignin-based microscale carbon fibers were studied from various aspects. Our thermal measurement indicated that the thermal conductivity of the lignin-based CFs could be as small as 1.83 W/(m·K). The thermal

reffusivity study from RT down to 10 K shows very weak temperature dependence. This phenomenon suggested dominant defect/boundary phonon scattering-sustained heat conduction in our carbon fibers. By utilizing a new defined parameter, the mean free path of phonon scattering due to grain boundary and defects in the lignin-based CFs was determined. This value (~12 Å) agreed well with the structure domain size determined by XRD (9 and 13 Å) and Raman spectroscopy (23 Å). The annealing effect on the micro-structure and thermal conductivity has been studied by micro-Raman spectroscopy and simulation. The as-prepared CFs only showed a typical structure of turbostratic carbon. After being highly annealed, our results showed that the concentration of graphitic structure in the annealed CFs increased and the microstructure of graphite improved. The thermal conductivity of the annealed lignin-based CFs could be increased by ten folds, as high as ~24 W/(m·K). The structure improvement was also studied by micro-Raman scanning from the highly-annealed region to slightly annealed region, showing a one-fold increase in the cluster size by annealing. The inverse of thermal conductivity was found to have a linear relationship with annealing temperature.

6.2 Future Work

6.2.1 Johnson noise technique combined with TET technique

In both TET technique and 3ω method, it is necessary to know the resistance temperature coefficient (dR/dT) of the sample to determine the thermal conductivity. When doing R-T calibration experiment, a thermocouple is usually employed to measure the temperature of the electrode ends. The measured temperature is taken as the experiment environmental temperature as well as the sample temperature. However, temperature difference between the sample and the environment may exist. Thus, the measured temperature has discrepancy with the sample's real

temperature. In the future, it is possible to use Johnson noise to obtain the real temperature of the sample without introducing any external noise and calibration. Combined with TET technique, the thermal conductivity of a microscale sample could be determined. In previous work, the temperature rise of the sample was induced by Joule heating which was offered by current. With the current in the measuring circuit, significant external noise was introduced when measuring Johnson noise. Under this situation, laborious setup is needed to eliminate the effect of external noise, which made the measurement extremely difficult. In the future, our goal is to use laser as the heating source. Under this situation, no external noise will be introduced into the circuit. Figure 6.1 shows the setup of obtaining *R*-*T* curve by using Johnson noise. During the test, a laser is used to induce temperature rise in the sample, at the same time the resistance (R_s) of the sample is measured by a 6½ digital multi-meter (Agilent 34401A). The Johnson noise of the sample after heating is first amplified by a preamplifier and then measured by a dynamic spectral analyzer. With known resistance and Johnson noise, the in-situ temperature of the sample is derived as $T = (S_V/g^2 - S_0)/(4k_B R_s)$. Here, S_V and S_0 are the measured power spectral density of Johnson noise and intrinsic instrument noise, respectively. g is the gain of the preamplifier. By varying the laser power, the *R*-*T* relationship could be obtained.

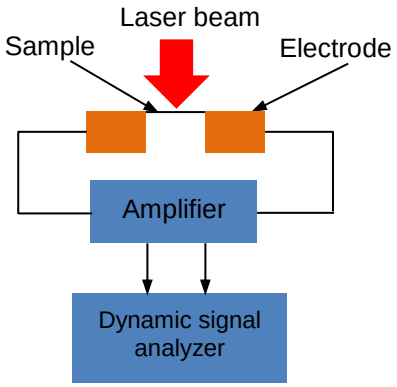

Figure 6.1 Schematic for *R*-*T* curve using laser-assisted Johnson noise.

6.2.2 Domain size study of low density polyethylene fibers

In Chapter 4, we presented the investigation of microstructure and temperature dependence of thermal properties for UHMWPE fiber. The phonon scattering by the grain boundaries at the 0 K limit was also introduced to obtain the domain size in UHMWPE fiber. The crystallite size of UHMWPE is relatively high and the crystallinity of our sample is 91.9%. In the future, we want to check whether thermal reffusivity theory is applicable to polymers with low crystallinity and relatively small crystallite size. So, this work would be extended to low density polyethylene (LDPE) fiber. LDPE is defined by a density range of 0.91-0.94 g/cm^3. Most of the LDPE is characterized by very branched molecules, which makes LDPE a very flexible material. The crystallite size of LDPE is dependent on the crystallite orientation. The orthorhombic crystallite size of LDPE is reported to be ~ 4 nm.[136] To date, there is very few work on the domain size and defects in LDPE. In the future, we will focus on the domain size in LDPE by utilizing the thermal reffusivity theory. The question that how the crystallinity and crystallite size is related with domain size is also a valuable aspect to study.

6.2.3 Thermal conductivity study of giant 2D material using differential technique

To date, the thermal conductivity of black phosphorus (BP) is majorly measured by conventional TDTR and four-probe transport measurements.[137, 138] The spot size (r = 5 μm) or even smaller value is used when utilizing TDTR method. The size of the BP flake is 2.46 μm in width and ~15 μm in length by utilizing four-probe transport method.[138] The thermal conductivity of suspended and supported molybdenum disulfide (MoS_2) measured by Raman spectroscopy and TDTR method has been reported before. Size of measured MoS_2 is only several μm in diameter.[139-141] However, there are very few reports about the thermal conductivity of giant 2D atomic-level

layers like graphene, BP and MoS_2. In previous work, we reported the thermal conductivity of giant (~ mm scale) single-layered to few-layered graphene supported by PMMA. The thermal conductivity measurement of giant supported graphene takes the phonon-boundary scattering into consideration. In the future, we aim at measuring the thermal diffusivity of giant MoS_2 supported by ultra-thin PMMA (~ 500 nm) by using the differential method. The size of the supported MoS_2 could be at mm scale. We may answer this question: will the thermal conductivity of giant 2D material with extensive grain boundaries be lower than that of microscale 2D materials? Also, we could study the size dependence of thermal conductivity of 2D materials.

The principle of differential technology is this: the ultra-thin (~nm) 2D material is supported by an ultra-thin polymer, like PMMA. The effective thermal conductivity of the whole sample is a function of thickness (δ) and thermal conductivity of both 2D material and PMMA. We could write the effective thermal conductivity (k_{eff}) as following equation: $k_{eff} = f(\delta_p, \delta_g, k_p, k_g)$. Since the thermal conductivity of MoS_2 is ~50 W/(m·K)[139-141] which is much smaller than that of graphene, to utilize the differential method to measure the thermal conductivity of giant flake of MoS_2, the layer number of MoS_2 should be at least 10. If the thickness of PMMA could be reduced to 200 nm, MoS_2 could be thinner than several nm. While measuring the thermal conductivity of a sample, the input heat and resistance temperature coefficient are needed. However, by utilizing the differential method, the thermal diffusivity is determined. Note that thermal diffusivity is only related with sample's length and thermal relaxation time. Thus, the measured thermal diffusivity will have higher measurement accuracy than that of thermal conductivity. The thermal conductivity of 2D material can be determined by multiplying the thermal diffusivity with heat capacity of the sample.

REFERENCES:

1. D. G. Cahill, W. K. Ford, K. E. Goodson, G. D. Mahan, A. Majumdar, H. J. Maris, R. Merlin and P. Sr, *J. Appl. Phys.*, 2003, **93**, 793-818.
2. J. Darabi, *Heat Transfer Eng.*, 2002, **23**, 1-2.
3. Z. Cheng, L. J. Liu, S. Xu, M. Lu and X. W. Wang, *Sci. Rep.*, 2015, **5**, 10718.
4. S. Shen, A. Henry, J. Tong, R. T. Zheng and G. Chen, *Nat. Nanotechnol.*, 2010, **5**, 251-255.
5. A. L. Moore and L. Shi, *Mater. Today*, 2014, **17**, 163-174.
6. T. M. Tritt, *Annu. Rev. Mater. Res.*, 2011, **41**, 433-448.
7. W. Yi, L. Lu, D. L. Zhang, Z. W. Pan and S. S. Xie, *Phys. Rev. B*, 1999, **59**, R9015-R9018.
8. D. G. Cahill, *Rev. Sci. Instrum.*, 1990, **61**, 802-808.
9. T. Choi, D. Poulikakos, J. Tharian and U. Sennhauser, *Nano Lett.*, 2006, **6**, 1589-1593.
10. L. Shi, D. Li, C. Yu, W. Jang, D. Kim, Z. Yao, P. Kim and A. Majumdar, *J. heat transfer*, 2003, **125**, 881-888.
11. P. M. Norris, A. P. Caffrey, R. J. Stevens, J. M. Klopf, J. T. McLeskey and A. N. Smith, *Rev. Sci. Instrum.*, 2003, **74**, 400-406.
12. D. G. Cahill, *Rev. Sci. Instrum.*, 2004, **75**, 5119-5122.
13. T. F. Luo and G. Chen, *Phys. Chem. Chem. Phys.*, 2013, **15**, 3389-3412.
14. G. Chen, *J. Nanopart. Res.*, 2000, **2**, 199-204.
15. P. Kim, L. Shi, A. Majumdar and P. L. McEuen, *Phys. Rev. Lett.*, 2001, **87**, 215502.
16. P. Kim, L. Shi, A. Majumdar and P. L. McEuen, *Physica B*, 2002, **323**, 67-70.
17. W. S. Capinski and H. J. Maris, *Rev. Sci. Instrum.*, 1996, **67**, 2720-2726.
18. J. Guo, X. Wang and T. Wang, *J. Appl. Phys.*, 2007, **101**, 063537.
19. X. Feng, X. Wang, X. Chen and Y. Yue, *Acta Mater.*, 2011, **59**, 1934-1944.
20. C. A. Paddock and G. L. Eesley, *J. Appl. Phys.*, 1986, **60**, 285-290.
21. A. Schmidt, M. Chiesa, X. Y. Chen and G. Chen, *Rev. Sci. Instrum.*, 2008, **79**, 064902.
22. C. L. Choy, Y. W. Wong, G. W. Yang and T. Kanamoto, *J. Polym. Sci. Polym. Phys. Ed.*, 1999, **37**, 3359-3367.
23. C. L. Choy, W. H. Luk and F. C. Chen, *Polymer*, 1978, **19**, 155-162.
24. T. A. Scott, J. Debruin, M. M. Giles and C. Terry, *J. Appl. Phys.*, 1973, **44**, 1212-1216.
25. J. Hennig, *J. Polym. Sci., Part C: Polym. Symp.*, 1967, **16**, 2751-2761.
26. C. L. Choy, *Polymer*, 1977, **18**, 984-1004.
27. C. L. Choy, E. L. Ong and F. C. Chen, *J. Appl. Polym. Sci.*, 1981, **26**, 2325-2336.
28. J. C. Maxwell, *Electricity and Magnetism, Part II*, Clarendon, Oxford, 3rd edn, 1904, ch. 9, p. 440.
29. D. Hansen and G. A. Bernier, *Polym. Eng. Sci.*, 1972, **12**, 204-208.
30. A. Henry and G. Chen, *Phys. Rev. Lett.*, 2008, **101**, 235502.
31. J. Liu and R. G. Yang, *Phys. Rev. B*, 2012, **86**, 104307.
32. J. Chen, G. Zhang and B. W. Li, *Nanoscale*, 2013, **5**, 532-536.
33. Z. Y. Ong and E. Pop, *Phys. Rev. B*, 2011, **84**, 075471.
34. B. Qiu, Y. Wang, Q. Zhao and X. L. Ruan, *Appl. Phys. Lett.*, 2012, **100**, 233105.
35. L. Lindsay, D. A. Broido and N. Mingo, *Phys. Rev. B*, 2011, **83**, 235428.
36. H. K. Liu, Y. Lin and S. N. Luo, *J. Phys. Chem. C*, 2014, **118**, 24797-24802.
37. A. Y. Serov, Z. Y. Ong and E. Pop, *Appl. Phys. Lett.*, 2013, **102**, 033104.

38. A. A. Balandin, S. Ghosh, W. Z. Bao, I. Calizo, D. Teweldebrhan, F. Miao and C. N. Lau, *Nano Lett.*, 2008, **8**, 902-907.
39. W. W. Cai, A. L. Moore, Y. W. Zhu, X. S. Li, S. S. Chen, L. Shi and R. S. Ruoff, *Nano Lett.*, 2010, **10**, 1645-1651.
40. F. Banhart, J. Kotakoski and A. V. Krasheninnikov, *ACS Nano*, 2011, **5**, 26-41.
41. A. Bagri, S. P. Kim, R. S. Ruoff and V. B. Shenoy, *Nano Lett.*, 2011, **11**, 3917-3921.
42. B. Mortazavi, M. Potschke and G. Cuniberti, *Nanoscale*, 2014, **6**, 3344-3352.
43. J. Lahiri, Y. Lin, P. Bozkurt, I. I. Oleynik and M. Batzill, *Nat. Nanotechnol.*, 2010, **5**, 326-329.
44. H. C. Dong, B. Wen and R. Melnik, *Sci. Rep.*, 2014, **4,** 703701-703705.
45. Z. Q. Wang, R. G. Xie, C. T. Bui, D. Liu, X. X. Ni, B. W. Li and J. T. L. Thong, *Nano Lett.*, 2011, **11**, 113-118.
46. J. H. Seol, I. Jo, A. L. Moore, L. Lindsay, Z. H. Aitken, M. T. Pettes, X. S. Li, Z. Yao, R. Huang, D. Broido, N. Mingo, R. S. Ruoff and L. Shi, *Science*, 2010, **328**, 213-216.
47. J. Liu, T. Y. Wang, S. Xu, P. Y. Yuan, X. Xu and X. W. Wang, *Nanoscale*, 2016, **8**, 10298-10309.
48. X. F. Xu, L. F. C. Pereira, Y. Wang, J. Wu, K. W. Zhang, X. M. Zhao, S. Bae, C. T. Bui, R. G. Xie, J. T. L. Thong, B. H. Hong, K. P. Loh, D. Donadio, B. W. Li and B. Ozyilmaz, *Nat. Commun.*, 2014, **5**, 3689.
49. L. Yang, P. Grassberger and B. Hu, *Phys. Rev. E*, 2006, **74**, 062101.
50. D. L. Nika, E. P. Pokatilov, A. S. Askerov and A. A. Balandin, *Phys. Rev. B*, 2009, **79**, 155413.
51. D. L. Nika, S. Ghosh, E. P. Pokatilov and A. A. Balandin, *Appl. Phys. Lett.*, 2009, **94**, 203103.
52. B. Nysten, J. P. Issi, R. Barton, D. R. Boyington and J. G. Lavin, *Phys. Rev. B*, 1991, **44**, 2142-2148.
53. J. Heremans, I. Rahim and M. S. Dresselhaus, *Phys. Rev. B*, 1985, **32**, 6742-6747.
54. L. Qiu, X. H. Zheng, J. Zhu, G. P. Su and D. W. Tang, *Carbon*, 2013, **51**, 265-273.
55. X. S. Huang, *Materials*, 2009, **2**, 2369-2403.
56. M. L. Bauer, C. B. Saltonstall, Z. C. Leseman, T. E. Beechem, P. E. Hopkins and P. M. Norris, *J. Heat Transfer*, 2016, **138**, 061302.
57. E. Frank, L. M. Steudle, D. Ingildeev, J. M. Sporl and M. R. Buchmeiser, *Angew. Chem., Int. Ed.*, 2014, **53**, 5262-5298.
58. E. Mayhew and V. Prakash, *Carbon*, 2013, **62**, 493-500.
59. J. Liu, Z. L. Xu, Z. Cheng, S. Xu and X. W. Wang, *ACS Appl. Mater. Interfaces*, 2015, **7**, 27279-27288.
60. Y. S. Xie, Z. L. Xu, S. Xu, Z. Cheng, N. Hashemi, C. CSDeng and X. W. Wang, *Nanoscale*, 2015, **7**, 10101-10110.
61. Z. Xu, X. Wang and H. Xie, *Polymer*, 2014, **55**, 6373-6380.
62. Y. S. Chenghao Deng, Lujun Pan, Tianyu Wang, Yangsu Xie, Jing Liu, Bowen Zhu, and Xinwei Wang, *ACS Nano*, 2016, **10**, 9710-9719.
63. C. Kittel, *Introduction to Solid State Physics*, John Wiley & Sons, 5th edn, 1976, ch. 4, p. 116.
64. C. Kittel, *Introduction to Solid State Physics*, John Wiley & Sons, 5th edn, 1976, ch. 5, p. 143.

65. C. Kittel, *Introduction to Solid State Physics*, John Wiley & Sons, 5th edn, 1976, ch. 5, p. 147-149.
66. P. Kim, L. Shi, A. Majumdar and P. L. McEuen, *Phys. Rev. Lett.*, 2001, **87**, 215502.
67. J. B. Johnson, *Phys. Rev.*, 1928, **32**, 97-109.
68. H. Nyquist, *Phys. Rev.*, 1928, **32**, 110-113.
69. R. Kisner, C. L. Britton, U. Jagadish, J. B. Wilgen, M. Roberts, T. V. Blalock, D. Holcomb, M. Bobrek and M. N. Ericson, IEEE *Aerospace Conference Proceedings*, 2004, 2586-2596.
70. C. J. Borkowski and T. V. Blalock, *Rev. Sci. Instrum.*, 1974, **45**, 151-162.
71. V. A. Khlus, *Sov. Phys. JETP*, 1987, **66**, 2179-2190.
72. M. Reznikov, M. Heiblum, H. Shtrikman and D. Mahalu, *Phys. Rev. Lett.*, 1995, **75**, 3340-3343.
73. H. Lin, S. Xu, X. W. Wang and N. Mei, *Small*, 2013, **9**, 2585-2594.
74. D. F. Santavicca, J. D. Chudow, D. E. Prober, M. S. Purewal and P. Kim, *Nano Lett.*, 2010, **10**, 4538-4543.
75. F. Volklein, H. Reith, T. W. Cornelius, M. Rauber and R. Neumann, *Nanotechnology*, 2009, **20**, 325706.
76. G. Q. Liu, S. Xu, T. T. Cao, H. Lin, X. D. Tang, Y. Q. Zhang and X. W. Wang, *Biopolymers*, 2014, **101**, 1029-1037.
77. F. P. Incropera, D. P. DeWitt, *Fundamentals of Heat and Mass Transfer*, John Wiley & Sons, 6th edn, 2006, Appendix A, p. 936.
78. Y. K. Kwon, A. Boller, M. Pyda and B. Wunderlich, *Polymer*, 2000, **41**, 6237-6249.
79. C. W. Bunn, *Chemical Crystallography*, Oxford University Press, 1945, ch. 7, p. 233.
80. H. Sato, M. Shimoyama, T. Kamiya, T. Amari, S. Sasic, T. Ninomiya, H. W. Siesler and Y. Ozaki, *J. Appl. Polym. Sci.*, 2002, **86**, 443-448.
81. A. Riveiro, R. Soto, J. del Val, R. Comesaña, M. Boutinguiza, F. Quintero, F. Lusquiños and J. Pou, *Appl. Surf. Sci.*, 2014, **302**, 236-242.
82. S. S. Chang, *J. Res. Natl. Bur. Stand., Sect. A*, 1974, **78**, 387−400.
83. T. Mugishima, Y. Kogure, Y. Hiki, K. Kawasaki and H. Nakamura, *J. Phys. Soc. Jpn.*, 1988, **57**, 2069-2079.
84. I. Perepechko, *Low-Temperature Properties of Polymers*, Pergamon Press Inc., 1980, ch. 2, p. 67-69.
85. Z. L. Xu, X. W. Wang and H. Q. Xie, *Polymer*, 2014, **55**, 6373-6380.
86. C. Kittel, *Introduction to Solid State Physics*, John Wiley & Sons, 5th edn, 1976, ch. 5, p. 128.
87. A. F. Cohen, *J. Appl. Phys.*, 1958, **29**, 870-870.
88. A. J. Kirkham, B. Yates, *J. Phys. C: Solid State Phys.*, 1968, **1**, 1162−1170.
89. S. J. Stuart, A. B. Tutein and J. A. Harrison, *J. Chem. Phys.*, 2000, **112**, 6472-6486.
90. S. M. Genensky and G. F. Newell, *J. Chem. Phys.*, 1957, **26**, 486-497.
91. G. Chen, *Phys. Rev. B*, 1998, **57**, 14958-14973.
92. R. J. Kolouch and R. G. Brown, *J. Appl. Phys.*, 1968, **39**, 3999.
93. Z. Y. Wei, Z. H. Ni, K. D. Bi, M. H. Chen and Y. F. Chen, *Phys. Lett. A*, 2011, **375**, 1195-1199.
94. Z. Yan, J. Lin, Z. W. Peng, Z. Z. Sun, Y. Zhu, L. Li, C. S. Xiang, E. L. Samuel, C. Kittrell and J. M. Tour, *ACS Nano*, 2012, **6**, 9110-9117.
95. H. Lin, S. Xu, Y. Q. Zhang and X. W. Wang, *ACS Appl. Mater. Interfaces*, 2014, **6**, 11341-11347.

96. D. Graf, F. Molitor, K. Ensslin, C. Stampfer, A. Jungen, C. Hierold and L. Wirtz, *Nano Lett.*, 2007, **7**, 238-242.
97. S. Some, Y. Kim, Y. Yoon, H. Yoo, S. Lee, Y. Park and H. Lee, *Sci. Rep.*, 2013, **3**, 01929.
98. E. Ochoa-Martinez, M. Gabas, L. Barrutia, A. Pesquera, A. Centeno, S. Palanco, A. Zurutuza and C. Algora, *Nanoscale*, 2015, **7**, 1491-1500.
99. E. X. Perez, Ph. D. thesis, Universitat Rovira i Virgili, 2007.
100. R. J. Crawford, *Plastics Engineering*, Elsevier Butterworth Heinemann, Oxford, 3rd edn, 1998, ch. 2, p. 59.
101. J. H. Hinnefeld, S. T. Gill, S. Zhu, W. J. Swanson, T. Li and N. Mason, *Phys. Rev. Appl.*, 2015, **3**, 014010.
102. M. Esposito, S. Buontempo, A. Petriccione, M. Zarrelli, G. Breglio, A. Saccomanno, Z. Szillasi, A. Makovec, A. Cusano, A. Chiuchiolo, M. Bajko and M. Giordano, *Sens. Actuators, A*, 2013, **189**, 195-203.
103. D. Yoon, Y. W. Son and H. Cheong, *Nano Lett.*, 2011, **11**, 3227-3231.
104. N. Mounet and N. Marzari, *Phys. Rev. B*, 2005, **71**, 205214.
105. W. Z. Bao, F. Miao, Z. Chen, H. Zhang, W. Y. Jang, C. Dames and C. N. Lau, *Nat. Nanotechnol.*, 2009, **4**, 562-566.
106. K. F. Mak, M. Y. Sfeir, Y. Wu, C. H. Lui, J. A. Misewich and T. F. Heinz, *Phys. Rev. Lett.*, 2008, **101**, 196405.
107. R. R. Nair, P. Blake, A. N. Grigorenko, K. S. Novoselov, T. J. Booth, T. Stauber, N. M. R. Peres and A. K. Geim, *Science*, 2008, **320**, 1308-1308.
108. J. M. Dawlaty, S. Shivaraman, J. Strait, P. George, M. Chandrashekhar, F. Rana, M. G. Spencer, D. Veksler and Y. Q. Chen, *Appl. Phys. Lett.*, 2008, **93**, 131905.
109. A. Soldera and J. P. Dognon, *Macromol. Symp.*, 1997, **119**, 157-164.
110. S. Rudtsch and U. Hammerschmidt, *Int. J. Thermophys.*, 2004, **25**, 1475-1482.
111. Z. Chen, W. Jang, W. Bao, C. N. Lau and C. Dames, *Appl. Phys. Lett.*, 2009, **95,** 161910.
112. E. H. Weber, B.S. thesis, Michigan Technological University, 2001.
113. X. Y. Fang, X. X. Yu, H. M. Zheng, H. B. Jin, L. Wang and M. S. Cao, *Phys. Lett. A*, 2015, **379**, 2245-2251.
114. A. C. Ferrari, *Solid State Commun.*, 2007, **143**, 47-57.
115. K. N. Kudin, B. Ozbas, H. C. Schniepp, R. K. Prud'homme, I. A. Aksay and R. Car, *Nano Lett.*, 2008, **8**, 36-41.
116. J. D. Renteria, S. Ramirez, H. Malekpour, B. Alonso, A. Centeno, A. Zurutuza, A. I. Cocemasov, D. L. Nika and A. A. Balandin, *Adv. Funct. Mater.*, 2015, **25**, 4664-4672.
117. R. Cusco, E. Alarcon-Llado, J. Ibanez, L. Artus, J. Jimenez, B. G. Wang and M. J. Callahan, *Phys. Rev. B*, 2007, **75**, 165202.
118. K. Kang, D. Abdula, D. G. Cahill and M. Shim, *Phys. Rev. B*, 2010, **81**, 165405.
119. D. L. Nika and A. A. Balandin, *J. Phys.*: *Condens. Matter*, 2012, **24**, 233203.
120. A. K. Vallabhaneni, J. Loy, D. Singh, X. L. Ruan and J. Murthy, *Proceedings of the ASME 2013 International Mechanical Engineering Congress and Exposition*, San Diego, 2013.
121. P. Virtanen, *Phys. Rev. B*, 2014, **89**, 245410.
122. W. D. Qu, Y. Xue, Y. W. Gao, M. Rover and X. L. Bai, *Biomass Bioenergy*, 2016, **95**, 19-26.
123. A. S. Pollard, M. R. Rover and R. C. Brown, *J. Anal. Appl. Pyrol.*, 2012, **93**, 129-138.
124. A. Kaniyoor and S. Ramaprabhu, *AIP Adv.*, 2012, **2**, 032183.
125. A. C. Ferrari and J. Robertson, *Phys. Rev. B*, 2000, **61**, 14095-14107.

126. F. Tuinstra and J. L. Koenig, *J. Chem. Phys.*, 1970, **53**, 1126-1130.
127. H. C. Schniepp, J. L. Li, M. J. McAllister, H. Sai, M. Herrera-Alonso, D. H. Adamson, R. K. Prud'homme, R. Car, D. A. Saville and I. A. Aksay, *J. Phys. Chem. B*, 2006, **110**, 8535-8539.
128. W. M. Haynes, *CRC Handbook of Chemistry and Physics*, Taylor & Francis, 97th edn, (Internet version) 2017, ch. 4, p. 119.
129. Y. J. Su, H. Wei, R. G. Gao, Z. Yang, J. Zhang, Z. H. Zhong and Y. F. Zhang, *Carbon*, 2012, **50**, 2804-2809.
130. Y. S. Xie, P. Y. Yuan, T. Y. Wang, N. Hashemi and X. W. Wang, *Nanoscale*, 2016, **8**, 17581-17597.
131. J. Krumhansl and H. Brooks, *J. Chem. Phys.*, 1953, **21**, 1663-1669.
132. A. A. Balandin, *Nat. Mater.*, 2011, **10**, 569-581.
133. G. A. Slack, *Phys. Rev.*, 1962, **127**, 694-701.
134. K. J. Thomas, M. Sheeba, V. P. N. Nampoori, C. P. G. Vallabhan and P. Radhakrishnan, *J. Opt. A: Pure Appl. Opt.*, 2008, **10**, 055303.
135. W. M. Haynes, *CRC Handbook of Chemistry and Physics*, Taylor & Francis, 97th edn, (Internet version) 2017, ch. 4, p. 116.
136. A. M. Hindeleh and B. R. Bulos, *Acta Polym.*, 1996, **47**, 105-111.
137. H. J. Jang, J. D. Wood, C. R. Ryder, M. C. Hersam and D. G. Cahill, *Adv. Mater.*, 2015, **27**, 8017-8022.
138. B. V. Brandon Smith, Jesús Carrete, Eric Ou, Jaehyun Kim, Natalio Mingo, and a. L. S. Deji Akinwande, *Adv. Mater.*, 2017, **29**, 1603756.
139. R. S. Yan, J. R. Simpson, S. Bertolazzi, J. Brivio, M. Watson, X. F. Wu, A. Kis, T. F. Luo, A. R. H. Walker and H. G. Xing, *ACS Nano*, 2014, **8**, 986-993.
140. J. Liu, G. M. Choi and D. G. Cahill, *J. Appl. Phys.*, 2014, **116**, 233107.
141. I. Jo, M. T. Pettes, E. Ou, W. Wu and L. Shi, *Appl. Phys. Lett.*, 2014, **104**, 201902.